Electrochemical Energy Reviews (2024) 7:1
https://doi.org/10.1007/s41918-023-00197-3

REVIEW ARTICLE

PGM-Free Biomass-Derived Electrocatalysts for Oxygen Reduction in Energy Conversion Devices: Promising Materials

Stefano Zago[1] · Laura C. Scarpetta-Pizo[2] · José H. Zagal[2] · Stefania Specchia[1]

Received: 22 October 2022 / Revised: 15 May 2023 / Accepted: 21 July 2023

Abstract

Biomass is a low-cost, abundant and renewable resource that can be used to manufacture porous carbon-based materials for a variety of applications. Different mesoporous carbon supports can be obtained from the various synthetic approaches that are aimed at increasing the specific surface area and functionalization. Currently, most of the biomass is used for energy recovery. The circular economy approach could lead to the development of cheap and sustainable materials, and turning of wastes into a precious resource. In this review, we provide the recent advances in the field of electrochemistry for porous carbon materials derived from biomass, which offers wider applications in proton exchange membrane fuel cells (PEMFCs), anion exchange membrane fuel cells (AEMFCs) and Zn-air batteries (ZABs). The focus is on understanding the required properties of the materials and the role of synthetic pathways in platinum group metal (PGM) free electrocatalysts. The most promising materials are evaluated towards the oxygen reduction reaction (ORR) in PEMFC, AEMFC, and ZAB. The results achieved showed that the expected performances on these energy conversion devices still lack for deployment in practice, especially if compared with commercially available PGM-free electrocatalysts. This review article provides insights on how to improve the actual electrocatalytic activity of biomass-derived materials.

Graphical Abstract

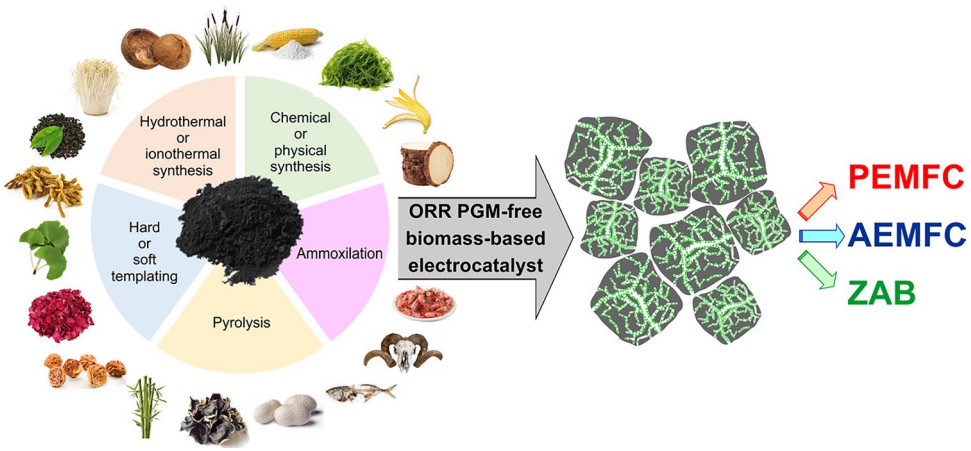

Keywords Mesoporous carbons · Fe–N–C electrocatalysts · Oxygen reduction reaction · Proton exchange membrane fuel cells · Anion exchange membrane fuel cells · Zinc-air batteries · Circular economy

Extended author information available on the last page of the article

Published online: 15 January 2024

1 Introduction

This century is facing a big challenge in terms of emissions reduction, and clean energy source development and deployment. Kyoto Protocol first (1997) [1], Paris Agreement later (2015) [2], and the Glasgow Climate Conference (COP26) in 2021 [3, 4] have established benchmarks for the present decade to drastically reduce emissions and the global temperature increase, that has emanated from heavy reliance on fossil fuels [5, 6]. In parallel, problems with increasing amounts of waste generated, along with recycling the vast amount of biological wastes from industry [7–13], could lead to a new circular economy that would turn waste into wealth [14–16]. Over 140 billion metric tons of biomass waste are produced every year. These are mostly carbon-containing materials that could be used in different fields upon their synthesis that offers good with industrial value and also support sustainability. Porous carbon materials can be obtained from animal and food wastes, as well as bacteria and other human activities [17, 18]. Biomass has been used for centuries but only in the last decades it has been explored for use in the field of electrochemistry. In fact, biomass-derived materials have been developed and tested for use in batteries, capacitors and supercapacitors, and also as electrocatalysts or support material for fuel cells applications [19–24].

The focus of this review paper is on the applications which offer most benefits, including their use in proton exchange membrane fuel cells (PEMFCs) that can convert chemical energy into electrical energy [25]. The main problem here is the slow reaction at the cathode, namely the oxygen reduction reaction (ORR) [26]. Currently, the best materials for the ORR electrocatalysis are Pt-based in acidic environment. Carbon materials without Pt could be used in anion exchange membrane fuel cell (AEMFC) cathode materials in alkaline environment with different mechanisms and also in direct alcohol fuel cells (DAFCs) [27–29]. Biomass-derived carbon materials offer a promising role here. However, the technology hinders from the high requirements, expensive electrocatalysts, and competition with other energy conversion devices. Therefore, the possibility to recycle waste to prepare new electrocatalysts could offer high value for this field of research, especially when many research groups report performances similar to Pt-based electrocatalysts, mostly in AEMFC applications.

However, for industrial applications, durable low-cost and stable electrocatalysts are requirements that are hardly met by Pt-based electrocatalysts, which suffer corrosion and particle aggregation [30–32]. Carbon-based materials are more durable, and amongst the biomass-derived materials, many of them have surpassed the performance of Pt-based electrocatalysts, especially in alkaline medium [33–35]. Biomass-derived carbon materials are useful as carbon-based supports because of their well-developed porous graphitic structure [36–38]. Indeed, the presence of heteroatoms provides adequate activity for ORR applications [20, 24, 39–41].

This review, after introducing the challenge of efficient ORR performance, reports on the best results obtained with biomass-derived materials from different research groups. The review compares not only the electrochemical parameters but also the approaches used, since a large variety of synthesis methods are possible. Figure 1A illustrates the main landscapes where biomass can be collected, re-used and recycled for its transformation into a carbon-based material. Figure 1B shows the increasing interest on biomass-derived carbon materials for electrochemical applications

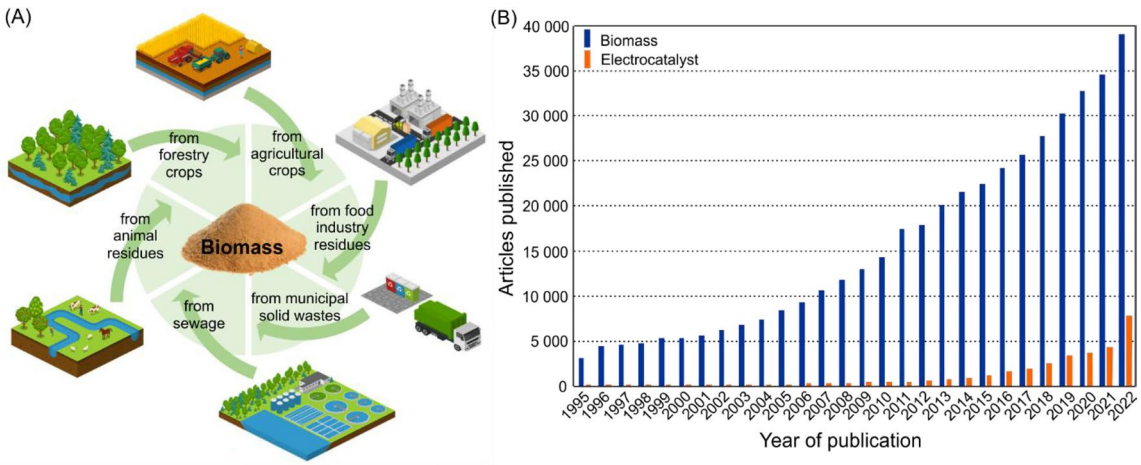

Fig. 1 **A** The sources of biomass. **B** Number of articles published during 1995–2022 with the keywords "biomass" or "electrocatalyst" as per Scopus database

over the past 25 years. Other possible technologies or a different point of view is given elsewhere [42–44].

2 Oxygen Reduction Reaction (ORR)—Issue

The ORR is the cathodic reaction in a hydrogen–oxygen fuel cell, wherein the oxygen must get converted to water in a complex 4-electron transfer process to release most of the possible energy. The multi-step nature of the reaction involving more than one electron makes the ORR a sluggish reaction [45], which occurs at a potential lower than the reversible one [46, 47]. Usually, the first electron transfer forming $O_{2,ads}$ is the rate determining step, since it is the slowest reaction in any operational condition. This is a surface-sensitive reaction and can occur without or with rapid proton transfer [48–50]. The $4e^-$ reduction involving the splitting of O–O bond releases maximum energy in the ORR process [27, 51]. The ORR efficiency is rather low because of the high overpotential, which translates to considerable loss of cell voltage [52]. The mechanism is complicated and still under debate [27, 53–55].

Although there are different models developed, the reaction mechanism depends on the nature of electrode surface, type of active sites, and the reactive environment (acidic, neutral, or alkaline). In aqueous media, the reaction occurs via an inner sphere electron transfer, involving the interaction of O_2 molecule bridging directly with the active sites on the electrode (Fig. 2A) [56]. The kinetics of the inner sphere electron transfer reactions depends on the nature of the electrode surface. This behavior is typical of reactions in acid electrolytes. For alkaline solutions instead, the reaction occurs via an outer sphere electron transfer mechanism, where the solvated molecular O_2 could interact with O atoms in the solvent water molecule in the outer Helmholtz plane and with the surface hydroxyl species (OH_{ads}) to give superoxide O_2^- (Fig. 2B) [27]. The kinetics of outer sphere reactions does not depend on the nature of the electrode surface [56]. Other adsorbed intermediates are also formed, such as HO_2^-, HO^-, O_2^- [48]. The model by Wroblowa in aqueous media simplifies the steps into two main pathways [57]. They include 4-electron process or 2-electron 2-step process with peroxide intermediate as the final product [57–61]. Only under strong alkaline medium an outer sphere 1-electron reduction process has been observed to generate solution phase superoxide, O_2^-(aq), from the reduction of O_2(aq) [62].

The main reaction pathways for ORR under acidic and alkaline environment are presented in Table 1 [27, 45, 47, 57, 59–61, 63, 64]. Oxygen can be directly converted into water in the first process (direct 4-electron reduction, $4e^-$) or it can be reduced in two steps of 2-electron reduction into hydrogen peroxide which can then undergo further reaction via different pathways (e.g., chemical decomposition to O_2, which can remain adsorbed on the electrode surface, or desorb into the solution). Typically, the step from HOO_{ads} to $2HO_{ads}$ is hard to realize on single atom catalytic sites. For ORR occurring on *fcc* metal {111} facets (typically platinum metal {111}), Viswanathan et al. [64] proposed an associative mechanism involving a sequential addition of a proton and electron in each elementary step. Note that direct reduction of O_2 to water via 4 electrons does not imply that the 4 electrons are transferred simultaneously as it is rather unlikely on energetic grounds. Electrons transfer occurs one

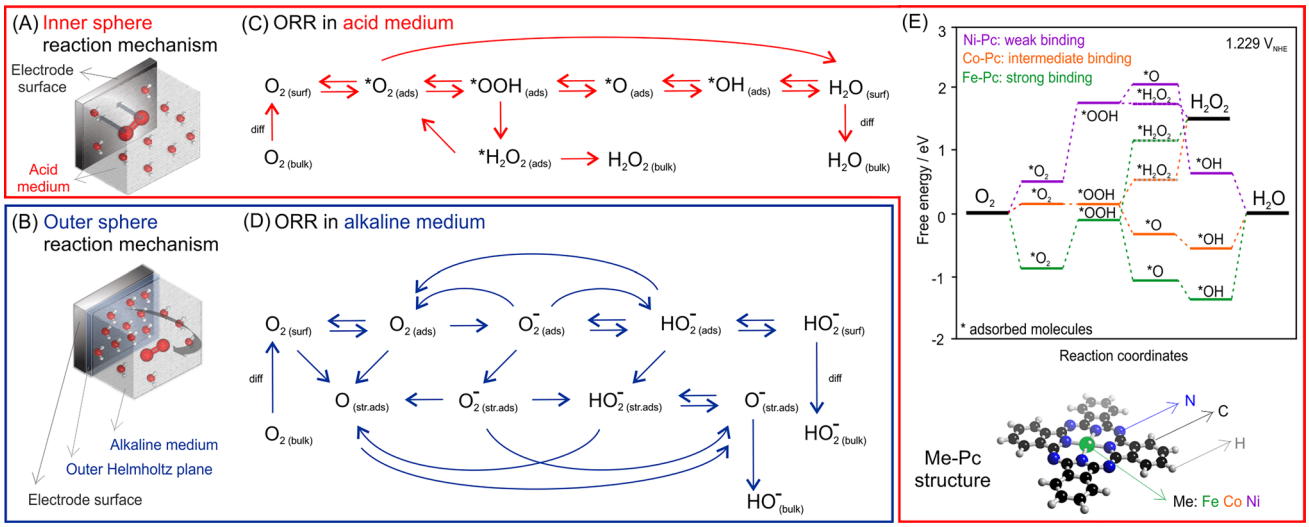

Fig. 2 **A** Inner and **B** outer transfer electron mechanisms. Possible ORR schemes in **C** acid medium and **D** alkaline medium. **E** An example of theoretical DFT calculation for the free-energy diagram of ORR in acid medium on several metal-phthalocyanine (Me-Pc) electrocatalysts at 1.229 V_{NHE}. Data readapted from [56, 69, 70]

Table 1 Main reaction pathways for the oxygen reduction reaction (ORR) [27, 45, 47, 56, 57, 59–61, 63, 64]

	Acid environment	Alkaline environment
Direct $4e^-$ pathway	$O_2 + 4H^+ + 4e^- \rightarrow 2H_2O$ $E^0 = +1.229\ V_{NHE}$	$O_2 + 2H_2O + 4e^- \rightarrow 4OH^-$ $E^0 = +0.401\ V_{NHE}$
Proposed $4e^-$ pathway reaction mechanism	$O_2(aq) \rightarrow O_{2,ads}$ $O_{2,ads} + e^- + H^+ \rightarrow HOO_{ads}$ $HOO_{ads} + e^- + H^+ \rightarrow 2HO_{ads}$ $2HO_{ads} + 2e^- + 2H^+ \rightarrow 2H_2O(l)$ or $O_2(g) + 4H^+ + 4e^- + * \rightarrow HOO^* + 3H^+ + 3e^-$ $HOO^* + 3H^+ + 3e^- \rightarrow O^* + H_2O(l) + 2H^+ + 2e^-$ $O^* + H_2O(l) + 2H^+ + 2e^- \rightarrow OH^* + H_2O(l) + H^+ + e^-$ $OH^* + H_2O(l) + H^+ + e^- \rightarrow * + 2H_2O(l)$	$O_2(aq) \rightarrow O_{2,ads}$ $O_{2,ads} + e^- + H_2O(l) \rightarrow HOO_{ads} + OH^-$ $HOO_{ads} + e^- \rightarrow O_{ads} + OH^-$ $O_{ads} + e^- + H_2O(l) \rightarrow HO_{ads} + OH^-$ $HO_{ads} + e^- \rightarrow OH^-$
Two-step $2e^-$ pathway via hydrogen peroxide	$O_2 + 2H^+ + 2e^- \rightarrow H_2O_2$ $E^0 = +0.695\ V_{NHE}$ $H_2O_2 + 2H^+ + 2e^- \rightarrow 2H_2O$ $E^0 = +1.776\ V_{NHE}$ or $2H_2O_2 \rightarrow 2H_2O + O_2$ (decomposition reaction)	$O_2 + H_2O + 2e^- \rightarrow HO_2^- + OH^-$ $E^0 = -0.065\ V_{NHE}$ $HO_2^- + H_2O + 2e^- \rightarrow 3OH^-$ $E^0 = +0.870\ V_{NHE}$ or $HO_2^- \rightarrow 2OH^- + O_2$ (decomposition reaction)

at the time, with each step involving an energy barrier. The same is true for the $2e^-$ reduction process. Figure 2C, D shows the ORR reaction schemes in acid and alkaline media. According to various kinetic studies, the most accepted pathway in acid medium is the one with peroxide intermediate [65–67]. This reaction is not desired in fuel cells because hydrogen peroxide adversely affects the stability of both the electrode and membrane. Furthermore, this reaction releases much less energy, almost half of the energy released by the direct $4e^-$ pathway [57–61]. Therefore, the electrocatalysts that promote the $4e^-$ mechanism are more suitable for fuel cells [63, 68].

In contrast to Pt-based electrocatalysts, platinum group metal free (PGM-free) electrocatalysts are recognized to be much more intrinsically active in alkaline medium compared to acid medium. The more favorable kinetics of ORR in alkaline environment is due to its surface independency of outer-sphere electron transfer reaction, wherein a peroxide intermediate is produced [27, 56]. Hydrogen peroxide reduction in alkaline medium is kinetically favored, so that the peroxide formed during ORR under alkaline conditions is immediately reduced to the $4e^-$ product. In contrast, the reduction of hydrogen peroxide in acid medium is kinetically disadvantageous because of its weak binding energy on the active site. As a consequence, hydrogen peroxide is directly desorbed into the bulk electrolyte (Fig. 2C) [27].

Several theoretical studies based on spin-polarized density functional theory (DFT) calculations elucidated various reaction pathways with their possible intermediate products, depending on the nature of the metal and heteroatoms used to dope the carbon. An example is visualized in the energy diagram depicted in Fig. 2E, which shows the free energy barriers of each ORR intermediate in acid medium at 1.229 V_{NHE} for phthalocyanines doped with different metals (Me-Pc, Me = Fe, Co, Ni) molecularly dispersed on carbon nanotubes [69, 70]. Depending on the nature of the metal, the selectivity of the ORR is different. In the case of Ni-Pc, the variation of the free-energy for the various reaction intermediates shows a remarkable preference for the $2e^-$ reaction pathway, leading to the release of hydrogen peroxide as final product. In fact, the *OOH intermediate on Ni-Pc exhibits a slight downward free-energy change to form $*H_2O_2$, while the formation of *O in the $4e^-$ pathway is energetically upward (unfavorable). Thus, Ni-Pc is more selective towards the $2e^-$ ORR reduction to H_2O_2. Conversely, Fe-Pc (and Co-Pc in a lesser extent) behaves in an opposite way, leading to the formation of water, thanks to more favorable values of the free-energy. Specifically, the *OOH intermediate on Fe-Pc exhibits a consistent favorable downhill free-energy change to form *O, and then *OH to generate water. While the step to generate $*H_2O_2$ requires a large (and unfavorable) free-energy increase. Thus, ORR on Fe-Pc follows the more favorable $4e^-$ pathway. The Co-Pc behaves like Fe-Pc generating water as final product, but with lower free-energy values for the various steps compared to Fe-Pc. That is, Fe-Pc is more selective to $4e^-$ pathway ORR compared to Co-Pc [69, 70]. As a conclusion, the strength of the binding between the metal and oxygenated intermediates is the key indicator for the selectivity of an ORR electrocatalyst. Strong O_2 binding molecular electrocatalysts promote ORR via 4-electrons, whereas weak-binding electrocatalysts promote ORR to hydrogen peroxide [51, 71]. This is also true for metal electrodes [72]. Modifying on purpose the molecular nature of an electrocatalyst means varying the free-energy of the potential determining steps of the reactions [73, 74]. The

key-point to enhance the ORR is to lower the overpotential, or the free-energy of the intermediate reaction steps [75–77].

To favor the ORR reaction, ORR electrocatalysts must possess these requirements: high electrocatalytic activity, high selectivity, high electrical conductivity, high chemical and electrochemical stability, high durability. Pt-based electrocatalysts are the most used. State-of-the-art Pt-based electrocatalysts, in fact, promote the 4-electron transfer process, with only small amounts of hydrogen peroxide formed. As a general rule, the closer the electron transfer number is to 4, the better the electrocatalyst is. Thus, ORR is the most studied reaction in low-temperature fuel cells because of the extremely sluggish kinetics at the cathode. Even highly loaded Pt-based electrocatalysts still cannot reach the possible rates of the anode reaction, namely the hydrogen oxidation reaction (HOR). Typically, HOR on Pt-based electrocatalysts have five times higher exchange current density compared to the ORR [78]. Therefore, ORR represents the bottle neck of the performance of a fuel cell, other than the aforementioned problem with the two possible reaction pathways. Pt-based electrocatalysts suffer from several technical problems: they are easily poisoned by CO, they react easily with methanol coming from methanol crossover in direct methanol fuel cells (DMFCs) [79–83]. Moreover, they show low stability in the long run because of Pt particle aggregation and dissolution (Ostwald ripening mechanism [84–86]). Furthermore, the supply of Pt represents a geopolitical problem. This metal is scarce, and mined in few countries. More than 70% of the world-wide Pt production comes from South Africa [87, 88]. These technical and geopolitical problems have been the main reasons to focus research efforts on lowering Pt loading and developing PGM-free electrocatalysts. Many strategies have been developed in this sense, for example alloying Pt with other metals [89–93] or finely controlling the particle size and distribution to obtain electrocatalysts with higher electrochemical surface area (ECSA) [94]. But most of all, the use of earth transition metals and heteroatoms, more abundant on earth crust compared to Pt, becomes an interesting option thanks to the overall good performance demonstrated so far [95–99].

A pioneering work was conducted in 1964 by Jasinski [100] studying new electrocatalysts for fuel cell cathodes based on materials containing non-noble metals. Jasinski studied metal (Fe and Co) phthalocyanines, which are molecular catalysts, as first valid alternative to noble metals. In 2009, Gong et al. [101] pioneered the use of metal-free electrocatalysts by presenting N-doped carbon nanotubes with performance close to Pt/C in alkaline media. This led the research towards the development of N-doped carbon structures, which have been considered the best starting point for next generation of ORR electrocatalysts. A porous structure is extremely important in developing efficient electrocatalytic surfaces. In fact, materials presenting mesopores facilitate the diffusion of chemical species through the electrocatalyst layer. Thus, the development of porous carbons, which are also electrically conductive, is of utmost importance [102, 103].

Considering the different ORR mechanisms in acid and alkaline media previously discussed, PGM-free electrocatalysts exhibit better performance in alkaline conditions compared to acid ones. Moreover, in alkaline media, the adsorption energy of the reactants on the active sites is lower because water molecules coordinate with metal ions, instead of metal particles [27, 48, 69, 70]. Nitrogen doping is an effective and interesting strategy because its incorporation into the sp^2 carbon structure increases the electrochemical activity and the electron-donor properties. In fact, doping with N atoms leads to a stronger interaction of C atoms with oxygen because of a different charge distribution in the carbon structure. Such a different charge distribution depends on the higher electronegativity of nitrogen. In this way, adjacent C atoms become more positively charged, allowing a greater interaction with oxygen molecules in the dissociative adsorption [104].

The deconvolution of N 1s peak in X-ray photoelectron spectroscopy (XPS) spectra allows the identification of four types of N–C bonding configurations, which highly affect the ORR activity. Pyridinic-N (at ≈398.3 eV) denotes N atoms at the edges, which bond to two C atoms and donate one p-electron to the π-system. Pyrrolic-N atoms refer to N atoms in a five ring, bound to two C atoms. Pyrrolic-N atoms contribute with two p-electrons to the π-system and have higher binding energy (at ≈400.1 eV). Graphitic-N (or quaternary-N) atoms (at ≈400.9 eV) replace a C atom bonding to three adjacent C atoms. Respect to pyridinic-N, pyridinic-N-oxide is linked to two C atoms and one oxygen and it is identified with a shift in binding energy of + 5 eV (at ≈403.5 eV) [105, 106]. Because of the dependence on the electronegativity, not all bonding configurations have the same effect, and also the structure of graphitic carbon network affects the ORR activity. Even if some researchers did not find a net correlation [107], most of the researchers agree that N-doping improves ORR activity [108]. Moreover, the type of functionalities is important: according to most of the literature, pyridinic-N and graphitic-N provide the highest activity enhancement [105–110].

Another strategy to increase the ORR activity consists of doping the carbon structure with heteroatoms such as sulfur (S), phosphorous (P), boron (B), silicon (Si), and halogens [111–114]. This specific doping gives rise to synergistic effects thanks to the different size and electronegativity of those heteroatoms compared to carbon. As a result, adjacent C atoms are more polarized, favoring thus the adsorption of oxygen [115]. The progresses achieved on metal-free electrocatalysts and doped porous carbon materials from

different chemicals and methods have been reported in recent reviews [116–123].

3 Biomass—Issue

Biomass is abundant, low cost and renewable [42, 124–133]. Therefore, the conversion of biomass into carbon nanostructures with an electrocatalytic activity has drawn the attention of researchers in the last decades. These materials have been tested either for batteries or supercapacitors [22, 44, 133, 134], as well as hydrogen evolution reaction [125], oxygen evolution reaction [135], and CO_2 capture [26, 90, 135, 136] with satisfactory results. Of course, from lab-scale production to large-scale commercialization, besides the electrochemical activity also other aspects play a crucial role, such as the production processes (usually involving high temperature treatments up to 800–1 000 °C and environmentally harmful) and their costs.

Biomass can either be harvested directly from the source or can be obtained from human/animal waste after its use. Biomass resources can be categorized in different ways. The main subdivision refers to its origin: vegetal source or animal source (Fig. 3A, B). Plant-derived biomass comes from biological photosynthesis and embraces any kind of vegetal residues, such as trees, grass, fruits, seeds, flowers, leaves, fungi, bacteria, and microorganisms. The main constituent of the cell walls is lignocellulose, that is a combination of cellulose, hemicellulose and lignin. Figure 3C shows the chemical formula of these three main constituents. Cellulose is a polysaccharide formed by repeated units of glucopyranose, with beta 1,4 glycosidic bonds and intermolecular hydrogen bonds within the matrix, resulting in a different orientation and degree of polymerization. It forms the skeleton of the walls of the cell, delimited by hemicellulose and lignin [137, 138]. The structure is packed thanks to hydrogen forces and van der Waals interactions, leading to a crystalline structure constituted by long chains of cellulose (microfibrils). Animal-derived biomass includes waste of animal origins such as manure, feathers, horns, skin, blood, cells, as well as human waste. These resources are composed mainly by proteins, aminoacids, and minerals. Most of the biomass

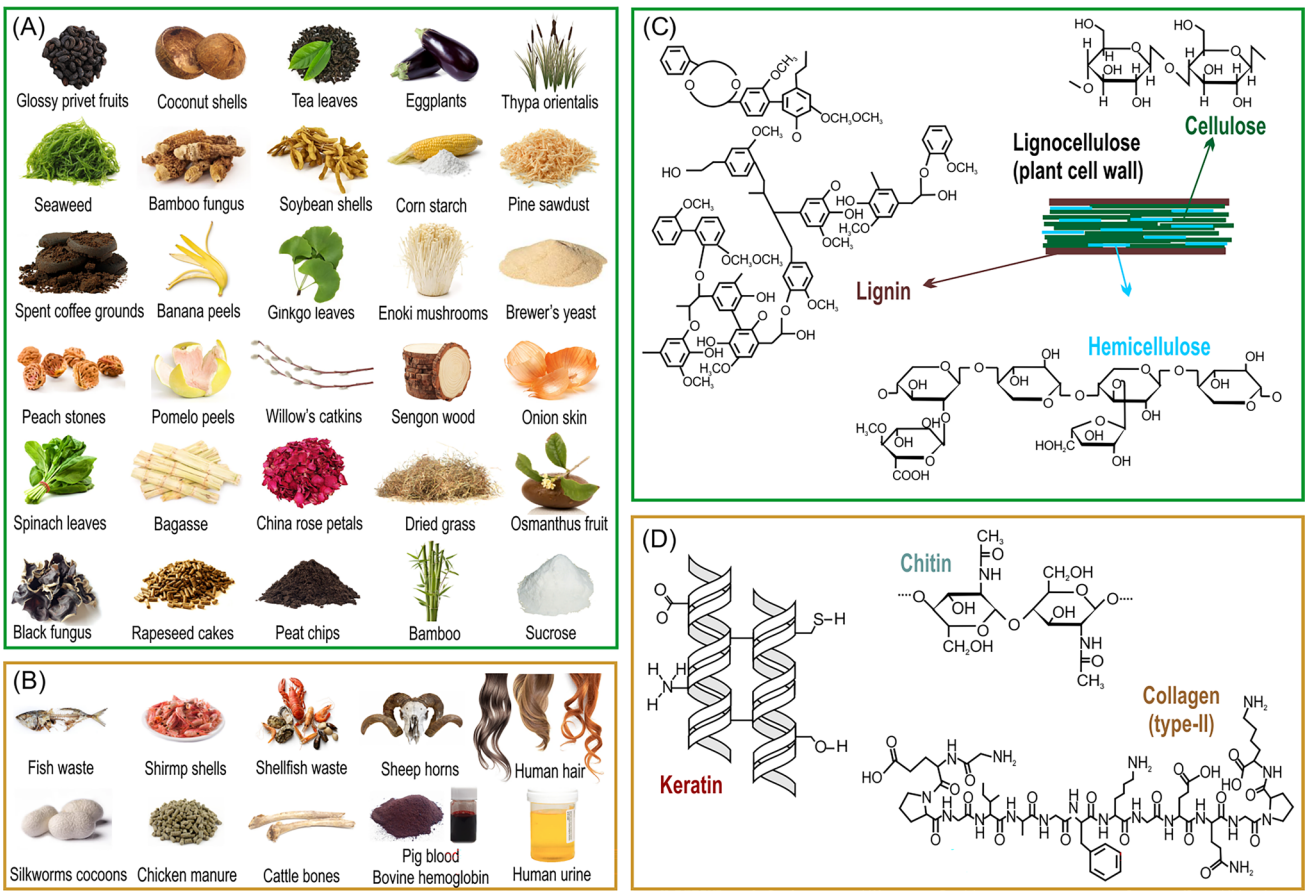

Fig. 3 Examples of biomass of **A** vegetal origin and **B** animal origin examined in this review. **C** Chemical formulas of the main components of lignocellulose, present in vegetal biomass: lignin, hemicellulose, and cellulose. **D** Chemical formulas of the main components present in animal biomass: keratin, chitin, and collagen

typically used as a source of carbon for electrocatalysts is composed of keratin (the most abundant structural protein of epithelial cells), chitin (the main component of insects' exoskeleton), or collagen (the primary protein building block of skin, tendons, muscles, and other connective tissues). Figure 3D shows their chemical formula. In particular, keratin consists of protein building blocks with aminoacid chains, coiled and cross-linked, containing N, S, and P. Thus, such heteroatoms can constitute natural doping agents for the carbon matrix of the electrocatalysts [41, 139].

Isolated cellulose consists of cellulose nanofibers (CNFs) and cellulose nanocrystals (CNCs). CNFs are typical in the range of 4–20 nm, a high aspect ratio and length in the range of micrometers. They can be isolated from the bleaching of pulp fibers via a high pressure and velocity impact grinding, homogenization, or micro-fluidization. CNCs are in the range of 100–1 000 nm, and can be extracted by acid hydrolysis, giving raise to crystalline and rigid particles [140].

Another type of cellulose is the bacterial cellulose, chemically identical to the plant-derived cellulose, but with a higher degree of crystallinity and stronger mechanical properties [141]. The 3D network of nanofibers has higher purity because it does not contain lignin or hemicellulose [142].

Lignin is a 3D amorphous organic polymer complex composed of aromatic units that differ in substituents, connected by oxygen bridging bonds and C–C bonds. It serves to connect cellulose, hemicellulose, and pectin providing rigidity and mechanical resistance to the walls of the cell, as well as antimicrobial and hydrophobic properties. Lignin is obtained in the form of black liquor, produced in cellulosic pulp mills and burned for cogeneration purposes or chemical recovery [43]. Therefore, the main source of lignin is paper industry, but mostly it is consumed as a fuel [143]. Hemicellulose is a hetero-polysaccharide, with variable composition depending on the sources, mainly xylans and glucomannans [144]. Acetylation in the chains are possible and usually the polymerization grade is lower than 200 and only amorphous phase is present [145–147].

Other types of polysaccharides have been studied as precursor for electrocatalysts. Starch is a glucan, whose main components are amylopectin and amylose, held together by glycosidic bonds [148]. Chitin has a similar fibrillary structure to cellulose and is the main component of the walls of the cell in fish scales and fungi, as well as exoskeletons of arthropods [149]. After deacetylation, chitin can be converted into chitosan, a copolymer of N-acetyl-glucosamine and glucosamine. In neutral pH, chitosan is insoluble in aqueous solutions. In low acidic pH, it is possible to protonate its aminic groups and obtain dissolution [150].

Biomass mainly comes from fungi, bacteria, marine algae or plants, agriculture-, human-, industrial- (usually contaminated biomass), and animal-derived waste. Most of the worldwide available biomass is commonly used in Africa and India for heating and cooking purposes. In these ways, the use of biomass is not efficient and not renewable. More advanced and efficient applications of biomass can be found in paper and pulp industry, building and power industry. For example, green nanocomposites and ionic conductors are prepared from biopolymers. Biofuels can be burnt by keeping the net CO_2 emissions equal to zero. Regrettably, biofuels are only slightly better than fossil fuel because the lower environmental impact is compensated by side effects on food availability, land and water resources requirements [151–153]. In fact, biofuels' production is strongly related with the water-energy-food-land (WEFL) nexus, that is the correct evaluation of the interfaces between science, policy, and businesses to realize long-term environmental, economic, and social goals and avoid conflicts for the accessibility of water and land for food harvesting [154–157]. Recent interesting applications focus on the production of syngas starting from high-density polyethylene (HDPE) and biomass waste, obtaining both a H_2-rich gas mixture and carbon nanotubes, with possible exploitation of the latter as supports for electrocatalysts [158]. Or the co-pyrolysis of biomass, plastic wastes (such as polyethylene PE, polypropylene PP, polystyrene PS, and polyethylene terephthalate PET) and COVID-19 waste (such as paper tissues and masks) to improve environmental sustainability and reduce plastic waste segregation [159–162].

As mentioned before, high electrocatalytic activity and high electrical conductivity are necessary requisites for ORR electrocatalysts, that translate into materials with high specific surface area and porosity, with accessible and stable active sites. Thus, the choice of the synthesis method is crucial to obtain these desirable materials. Among the various synthesis strategies studied for valorizing biomass resources, the most interesting and used ones are the hydrothermal carbonization, pyrolysis, ammoxidation, chemical or physical activation, and templating methods (hard or soft templating), as exemplified in Fig. 4. Single and multiple step processes, and combination of different processes have been deeply studied. All these studies commonly use N- or heteroatom-containing reagents, as well as transition metals (mostly Fe and Co), since all of these atoms have been proved to enhance the electrocatalytic properties of the desired electrocatalysts.

Hydrothermal carbonization (HTC) involves dehydration, condensation, polymerization, and aromatization to obtain a carbon material from a biomass resource, usually under self-generated pressures and temperatures below 200 °C [163, 164]. Due to the mild conditions of synthesis, HTC-derived carbons show quite low specific surface areas (lower than 10 $m^2\ g^{-1}$) and poor electron conductivity. Therefore, further treatments are needed, such as activation or graphitization. In iono-thermal carbonization (ITC), ionic liquids (ILs) are commonly used, instead of water, because of their high

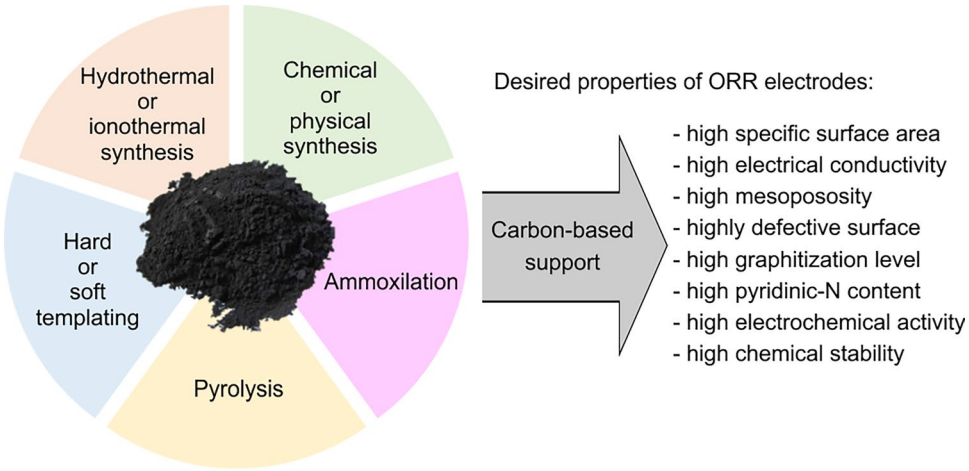

Fig. 4 Main synthesis methods for producing biomass-derived C-based supports for ORR electrocatalysts

thermal stability, low volatility, and ability of stabilizing the reactive mixture [165].

Chemical activation usually involves impregnation of biomass with specific dehydrating reagents (such as KOH, NaOH, H_2PO_4, $ZnCl_2$), followed by a pyrolysis step at temperatures higher than 300 °C [166]. As for physical activation, there are two steps involved: a first carbonization in inert atmosphere at around 500 °C, and a second physical activation with either steam or CO_2 at around 1 000 °C [167]. High specific surface area can be obtained with NH_3 treatment, a process called ammoxidation [168–171], which involves the formation of nitrogen radicals by attacking atomic nitrogen and hydrogen on carbon fragments to form N-containing electroactive sites [172].

In the hard-templating method, a sacrificial scaffold is used, for example mesoporous silica, zeolite, or clay. The purpose is to tune the formation of meso- and micro-pores during the pyrolysis step [173–177]. In the soft-templating method, on the other hand, surfactant agents or polymers are used to bind the carbon precursors and templating agents, which mold the organic structure [44, 171, 178–182].

An alternative option to avoid templating or chemical activation is the use of carbon aerogels to obtain highly porous carbons. Carbon aerogels can be synthesized from polysaccharides (starch, cellulose, chitosan, chitin [44]), polyphenolic complexes (lignin, tannin [183–185]), alkyl-resorcinols or poly-resorcinols [185–187]. The typical synthesis' steps comprise the development of a hydrogel, followed by the substitution of the solvent with a lower-surface-tension liquid, lyophilisation (or freeze drying), and carbonization [44].

The aforementioned synthesis methods include a step of pyrolysis or carbonization as unavoidable step to eliminate volatile compounds such as CO_2, CH_4, CO, and organic compounds, leaving only a carbon-based solid material with increased conductivity. Typical temperatures of pyrolysis range between 700 and 1 000 °C. Finally, a post-treatment with mild acidic solutions is sufficient to remove inorganic residues after the pyrolysis step [188]. The pyrolysis of biomass is highly interesting to favor the formation of the desired level of porosity. The biomass, in fact, is characterized by a typical hierarchically porous morphological architecture, which is usually maintained in the final electrocatalysts after the pyrolysis, giving raise to the so-called "memory effect" [182, 189, 190].

4 Electrochemical Techniques

Cyclic voltammetry (CV) and linear sweep voltammetry (LSV) are the most used techniques for the electrochemical characterization of electrocatalysts, included the analysis of the ORR kinetics. Typical instruments are the rotating disc electrode (RDE) and rotating ring-disk electrodes (RRDEs). The CV technique involves the measuring of potential-intensity curves in a potential range, and allows the observation of oxidation and reduction peaks typical of the materials under investigation. The curves obtained by LSV at low potential scan rate are interpreted with the Koutecky-Levich (KL) model for kinetic information. In particular, from LSV curves we determine the two major descriptors used for discriminating the ORR electrocatalytic activity, namely the onset potential, E_{onset}, defined as the potential required to produce an ORR Faradic current of 0.1 mA cm^{-2}, and the half-wave potential, $E_{1/2}$, assumed as the potential where half of the maximum current density is reached [191].

Controlled-potential chrono-amperometry (CA) is an electrochemical technique used to monitor the Faradic current and assess the stability of the electrocatalysts. The functional relationship between current response and time provides a first estimation of the stability of the electrode. Such a technique discriminates the activity of various materials. The more the current remains constant at a fixed potential, the more stable the electrocatalyst is. Moreover, during

CA, methanol can be injected in the electrolytic solution to evaluate the tolerance of the electrocatalyst towards this compound. The less the electrocatalyst reacts with methanol, the better the performance. This test is important for direct methanol fuel cells (DMFCs), which suffer of methanol crossover [79–81]. Methanol crossover is the undesired effect for which part of the methanol fed at the anode reaches the cathode crossing the membrane together with protons. The crossed methanol can in principle react on the cathodic electrocatalyst, reducing dramatically the open cell circuit voltage. The mixed potential arising from the simultaneous oxygen reduction and methanol oxidation on the same catalytic active site lowers the cell voltage. On this point of view, Pt-based electrocatalysts are highly active towards methanol oxidation, giving rise to the mixed potential. In contrast, PGM-free electrocatalysts are inactive towards methanol oxidation, and then highly desirable for ORR reaction [82, 83].

The number of total transferred electrons (n) can be calculated from the slope of the KL graphs at different potentials. The use of the RRDE provides a method for directly measuring the in-situ hydrogen peroxide formation during the reaction. In fact, the ring around the disk serves as a hydrogen peroxide amperometric sensor and it is set at a constant potential (independent of the disk potential) at which hydrogen peroxide oxidation is under mass transport control [65].

5 Biomass-Derived Electrocatalysts Tested in RDE/RRDE

All the physical–chemical and electrochemical data of the examined electrocatalysts tested in RDE/RRDE configuration are listed in Table 2. Figures from 5 to 12 show experimental data as reported in the original references, with potential values as used by the various authors. We converted the onset potential (E_{onset}) and half-wave potential ($E_{1/2}$) values in V vs. RHE, when reported in different potential values in the related references, and listed them in Table 2, to favor a comparative data analysis.

6 Electrocatalysts of Vegetal Origin (Plant-Derived Biomass)

Borghei et al. [192] worked with coconut shells and obtained a highly porous N-, P-doped carbon structure after an activation of the biomass with phosphoric acid and urea at mild temperature (550 °C), followed by functionalization and pyrolysis at 1 000 °C. Figure 5A shows the main results obtained with this coconut-derived electrocatalyst. Coconut shells are good starting materials because of high carbon content, high density, low ash content, thanks to the lignin amount up to 50% [193]. The structure can endure the pyrolysis without shrinking thanks to the binding of phosphate and phosphate ester to the lignocellulose. A very high specific surface area was obtained. The authors speculated that a prior functionalization treatment aimed at forming oxygen groups in the surface could improve the N content thanks to a better anchoring of urea. With a short 13 h chronoamperometry, the authors assessed the stability of the coconut shell-derived electrocatalyst, which decreased to values similar to those of a commercial Pt/C used as a comparison term. Anyway, the degradation of the biomass electrode reached a plateau, while the degradation of Pt/C displayed a sharper slope.

Liu et al. [20] synthesized ORR electrocatalysts from the fruits of glossy privet (*Ligustrum lucidum*) as a raw material. The synthesis steps comprise a hydrothermal treatment at 180 °C, $KHCO_3$ activation at 900 °C, N-doping with melamine, further heat treatments at 450 and 650 °C to produce graphene-like and defect-rich carbon sheets with N doping, as shown in Fig. 5B. The procedure is sustainable, low-cost, non-toxic, and easily scalable. The electrocatalyst results highly conductive, with a high specific surface area and a defective structure with edges, pores, forks, and cracks, showing a typical stack structure, as visible from TEM images. The synergistic effect of N-doping atoms and topological defects provide good electrocatalytic properties for ORR and moderate activity for OER. Moreover, the electrocatalyst resulted also very stable, according to a CA of 11 h: the electrode retained almost 94% of the initial current density, while the commercial Pt/C used as a comparison retained only 40%. This electrocatalyst has been successfully tested also for rechargeable ZAB, providing a peak power density of 68 mW cm^{-2}.

An electrocatalyst with good electroactivity and stability towards fuel crossover and continuous cycling was synthetized by Gao et al. [194] from bamboo fungus, a type of fungus with high protein content and little medical value. Because of the source, the material is naturally N-enriched without further doping. The synthesis involved hydrothermal treatment and only one heat treatment at 800 °C, which guarantees an ultra-high specific surface area. The approach appears to be quite straightforward for different types of starting biomass without need of adding reactants (Fig. 5C). The produced electrocatalyst exhibits excellent electrocatalytic activity for ORR via a dominant four-electron pathway in a 0.1 M (1 M = 1 mol L^{-1}) KOH aqueous solution. Moreover, it also showed methanol and CO tolerance compared to a commercial Pt/C electrocatalyst, and excellent stability.

A N-, F-doped porous carbon from tea residue (tea leaves after brewing, T-NFC) was obtained by a one-step pyrolysis at 1 000 °C, without activation or any post treatment (Fig. 5D) by Wu et al. [195]. Both N and F atoms are already

Table 2 Physico-chemical-electrochemical data of biomass-derived electrocatalysts. Atomic % (or weight % if the number is marked with an asterisk) from XPS analysis (relative % for N1: pyridinic-N; N2: N-Me; N3: pyrrolic-N; N4: graphitic-N; N5: oxidized-N; N6: other N-types). Specific surface area (S.S.A.), total volume (V_{TOT}) and micropore volume (V_{micro}) and average pore size (P.S.) from N_2 physisorption analysis. Onset potential (E_{onset}) and half-wave potential ($E_{1/2}$) from RDE/RRDE measurements in acid and/or alkaline electrolyte

Electrocatalysts derived from	$T_{pyrolysis}$/°C	Atoms, at.% (wt.% if *)										S.S.A./ ($m^2\ g^{-1}$)	V_{TOT}/ ($cm^3\ g^{-1}$)	V_{micro}/ ($cm^3\ g^{-1}$)	P.S./ nm	E_{onset}/(V vs. RHE)	$E_{1/2}$/ (V vs. RHE)	Electrolyte acid/alk.	Figure [Ref.]
		N	(N1	N2	N3	N4	N5	N6)	P	S	Fe/Co								
		From XPS (or from ICP if * presents)										From N_2 physisorption				From RDE measurements			
Biomass of vegetal origin																			
Coconut shell	1 000	1.10	(31.1	–	24.8	33.6	10.5	–)	2.3			1 071	1.15	0.30	4.8	0.944	0.754	0.1 M KOH	5A [192]
Glossy privet fruits	900	3.71	(40.0	–	23.0	–	–	–)				1 559	0.90	0.82	2	0.92	0.81	0.1 M KOH	5B [20]
Bamboo fungus	800	2.33	(39.1	–	30.0	28.1	2.1	–)				1 896	1.07			0.854	0.793	0.1 M KOH	5C [194]
Tea residues	1 000	2.8	(41.9	–	21.7	36.4	–	–)				856	0.65		3	0.81	0.66	0.1 M KOH	5D [195]
Tea leaves	800	2.74	(		n.a.			–)	1.03		0.44/–	346	0.10		2.9	0.95	0.79	0.1 M KOH	5E [196]
Seaweeds	900	0.1	(		n.a.			–)				1 377				1.01	0.83	0.1 M KOH	6A [197]
																	0.60	0.5 M H_2SO_4	
Eggplants	1 000	1.04	(34.6	–	52.8	12.6	–	–)				1 969				0.884	0.784	0.1 M KOH	6B [198]
																	0.55	0.1 M $HClO_4$	
Soybean shells	1 000	5.73	(48.5	–	28.4	7.6	15.5	–)				1 152	0.67			0.96	0.94	0.1 M KOH	6C [199]
																	0.55	0.1 M $HClO_4$	
Soybean straw	800	6.24	(		n.a.			–)			1.79*/–	521	2.20		3.8	0.989	0.854	0.1 M KOH	6D [200]
																0.886	0.754	0.1 M $HClO_4$	
Soybean dregs	800	7.69	(50.6	–	10.3	21.1	18.2	–)			0.43/–	239	0.88	0.02	4	0.951	0.831	0.1 M KOH	6E [19]
Spent coffee	800	3.54	(		n.a.			)	1.15			1 018	0.21		4.3	0.98	0.86	0.1 M KOH	7A [201]
Banana peels	1 000	3.11	(46.6	–	13.6	32.6	7.2	)				1 756			2.8	0.934	0.794	0.1 M KOH	7B [202]
																	0.586	0.1 M $HClO_4$	
Dried aronia	950	1.23	(20.0	–	21.0	–	–	–)			0.21/–	561	0.37	0.23	1.9	0.84	0.67	0.1 M NaOH	7C [203]
Peach stones	950	0.63	(25.0	–	24.0	–	–	–)			0.57/–	846	0.53	0.37	1.6	0.92	0.78	0.1 M NaOH	7C [203]
Gingko leaves	800	2.30	(	–	n.a.			–)				583	0.41		3.5	0.91	0.88	0.1 M KOH	7D [204]
Willow catkins	800	4.15	(45.9	21.6	24.4	8.1	–	–)			1.7/–	462			3	0.87	0.77	0.1 M KOH	7E [205]
																	0.76	0.5 M H_2SO_4	
Onion chips	900	5.32	(38.8	–	–	50.3	10.3	–)		2.23		1 859				0.964	0.814	0.1 M KOH	8A [208]
Brewer's yeast	900	3.90	(34.8	–	18.7	40.0	6.5	–)	0.46		0.8/–	791			4	0.985	0.861	0.1 M KOH	8B [207]
Spinach leaves	900	3.94	(21.1	–	8.9	43.9	6.3	–)	0.21		0.32/–	290	0.91			0.98	0.88	0.1 M KOH	8C [40]

Table 2 (continued)

Electrocatalysts derived from	$T_{pyrolysis}$/°C	Atoms, at.% (wt.% if *)										S.S.A./ ($m^2\ g^{-1}$)	V_{TOT}/ ($cm^3\ g^{-1}$)	V_{micro}/ ($cm^3\ g^{-1}$)	P.S./ nm	E_{onset}/(V vs. RHE)	$E_{1/2}$/ (V vs. RHE)	Electrolyte acid/alk.	Figure [Ref.]
		N	(N1	N2	N3	N4	N5	N6)	P	S	Fe/Co						0.75	0.1 M $HClO_4$	
Microalgae	1 000	0.70	(29.3	–	10.7	45.1	15.0	–)								1.00	0.864	0.1 M KOH	8D [39]
Beancurd	900	5.02	(28.0	–	52.0	14.0	6.0	–)				988	0.69			0.96	0.81	0.1 M KOH	8E [209]
Sengon wood	900	3.97	(17.9	–	5.3	76.8	–	–)			4.86/–	55	0.19		3	0.91	0.84	0.1 M KOH	9A [211]
Enoki mushrooms	900	3.20	(		n.a.			)				305			3	0.94	0.81	0.1 M KOH	9B [212]
																0.86	0.6	0.5 M H_2SO_4	
Monkey grass	–	3.37	(		n.a.			)								0.884		0.1 M KOH	9C [213]
China rose petals	900	3.80	(8.8	–	22.4	68.9	–	–)		0.6		1 478				1.03	0.81	0.1 M KOH	9D [214]
																	0.55	0.1 M $HClO_4$	
Typha orientalis	800	9.10	(33.2	–	40.9	5.6	20.3	–)		0.06		646	0.36	0.24		0.9	0.8	0.1 M KOH	9E [215]
								–)								0.725		0.5 M H_2SO_4	
Osmanthus fruit	900	5.77	(		n.a.			)	0.34	0.4		295	0.93	0.10	3.7	0.88		0.1 M KOH	10A [216]
																0.69		0.1 M $HClO_4$	
Pomelo peels	900	5.96	(		n.a.			)				1 194			4	0.96	0.86	0.1 M KOH	10B [217]
Bagasse	1 000	2.40	(25	–	8	67	–	–)				1 284			2	0.88	0.76	0.1 M KOH	10C [218]
																0.69	0.5	0.5 M H_2SO_4	
Corn starch	1 000	2.42	(37.7	–	7.1	46.4	8.8	–)				1 569			12.4	0.934	0.831	0.1 M KOH	10D [219]
																0.876		0.5 M H_2SO_4	
Pine sawdust	1 000	1.85	(48.1	–	24.9	7.6	19.5	–)	0.19		0.04/–	2 066	1.24	0.29	3	1.05	0.874	0.1 M KOH	10E [219]
Biomass of animal origin																			
Sheep horn	900	3.14	(	–	n.a.			–)		0.22		322			4.2	0.904	0.734	0.1 M KOH	11A [230]
Cattle bones	800	3.20	(55.7	–	17.1	10.2	17.0	–)	3.96			1 516	0.98	0,54	3.8	0.924	0.828	0.1 M KOH	11B [231]
Fish scales	900	3.80	(29.5	–	29.9	40.6	–	–)				850	0.53		2.5	1.00	0.87	0.1 M KOH	11C [232]
																0.86	0.72	0.1 M $HClO_4$	
Shrimp shells	900	2.53	(13.8	–	26.3	49.1	10.8	–)	1.30			447			8	0.96	0.78	0.1 M KOH	11D [233]
Silkworm cocoons	950	3.65	(		n.a.			)	5.35			135	0.10		1.3	0.94	0.76	0.1 M KOH	11E [234]
Chitosan	1 000	4.36	(27.5	–	7.9	61.7	2.9	–)				1 510	1.32	0.93	2	0.954	0.824	0.1 M KOH	12A [236]
Chicken manure	750	1.07	(62.5	10.2	14.6	–	8.1	–)				692			3.8	0.86	0.78	0.5 M KOH	12B [237]

Table 2 (continued)

Electrocatalysts derived from	$T_{pyrolysis}$/°C	Atoms, at.% (wt.% if *)										S.S.A./ ($m^2\ g^{-1}$)	V_{TOT}/ ($cm^3\ g^{-1}$)	V_{micro}/ ($cm^3\ g^{-1}$)	P.S./ nm	E_{onset}/(V vs. RHE)	$E_{1/2}$/ (V vs. RHE)	Electrolyte acid/alk.	Figure [Ref.]
		N	(N1	N2	N3	N4	N5	N6)	P	S	Fe/Co								
Pig's blood	950	2.30	(23.1	20.7	33.1	–	23.1	–)			4.9*/–	211	0.16			0.86		0.1 M KOH	12C [238]
Human hairs	900	3.80	(	–	n.a.			)		1.73		1 814			4	0.934	0.834	0.1 M KOH	12D [239]
Human urine	1 000	2.60	(	–	n.a.			)	0.2	0.9		811	0.58	0.12	3.1	0.948	0.854	0.1 M KOH	12E [240]
Biomass tested in PEMFC or AEMFC																			
Black fungus (FeNC-BFungus)	950	5.17	(22.1	9.7	46.3	21.9	–	–)		0.17*	0.13*/–	916					0.86 0.65	0.1 M KOH 0.1 M $HClO_4$	13A/16Ac [241]
Peat (CoNC-peat)	1 000	2.11	(38.9	27.8	23.6	9.7	–	–)			–/3.59	273	0.18	0.06	36.4	0.77		0.1 M $HClO_4$	13B/16Ab [242]
Hemoglobin (FeNC-hemo)	900		(		n.a.			)			0.25/–	1 110	1.94		2.5				13C/16Aa [243]
Bamboo (NSC-bamboo)	800	6.32	(44.1	–	28.3	18.5	9.0	–)		1.26		349	0.302	0.216			0.85	0.1 M KOH	14A/16Bb [189]
Sucrose	900		(		n.a.			)			8*/–					0.95	0.81	0.1 M KOH	14B [244]
Rapeseed cakes (FeCoNF-rapeseed)	800	11.4	(48.5	5.0	30.3	10.8	2.5	2.9)	3.33	0.45	0.5/1.2	415	0.61	0.09	3.5	0.95	0.81	0.1 M KOH	14C/16Ba [245]
Hard-templating of inorganic reagents tested in PEMFC or AEMFC																			
FeNC-ZIF	1 050											322	0.46		1	0.98	0.809	0.1 M $HClO_4$	16Ad [254]
FeNC-C29	1 000	2.28	(24.6	–	37.7	22.8	6.1	8.8)			0.62*	700			7	0.80	0.69	0.5 M H_2SO_4	16Ae [253]
FeNC-C30	1 000	2.32	(25.4	–	39.2	25.0	3.0	7.3)		0.18*	1.06*	725			7	0.86	0.76	0.5 M H_2SO_4	16Af [253]
FeCoNC-resorcinol	800	1.4	(27.1	20.0	31.4	11.4	10.1	–)			0.1/0.1	399	0.58	0.12	15	0.96	0.83	0.1 M KOH	16Bc [256]
$Fe_{0.5}NC\text{-}NH_3$	1 050											970				1	0.84	0.1 M $HClO_4$	16Bd [255]
FeNC-PFM11094	1 000	2.3	(11.6	7.1	39.4	22.1	19.8	–)			0.25	593	1.023	0.103	30	1.00	0.846	0.1 M KOH	16Bf [257]

available in the tea leaves, thus no external doping is necessary. The synthesis is very straightforward, and the material shows interesting electroactivity, with an almost 4-electron reaction pathway, high durability and excellent methanol tolerance in alkaline environment. The good electrochemical activity has been assigned to the synergy between nitrogen, which provided a high content of pyridinic- and graphitic-N, and fluorine atoms (2.2 at.%, at.% means atomic percentage). Fluorine is not a common choice as doping atom, it allows a more relevant charge distribution because of its high electronegativity. A stability test conducted after 5 000 potential cycling shows negligible performance loss, sign of a good stability of the as-synthesized electrocatalyst in alkaline medium.

Also Guo et al. [196] started from tea leaves to synthesize ORR electrocatalysts. Tea leaves are interesting starting biomass because they are reach of heteroatoms (N, P, Fe) and possess a 3D structure consisting of natural channels, which can favor the formation of a hierarchically porous carbon framework with micro-, meso-, and macropores. A preliminary preparation of the samples involved impregnation of the pristine tea leaves with ferric chloride to obtain polyphenols-iron complexes. After a freeze-drying process, a one-step pyrolysis was conducted. Various temperatures were investigated. The best sample was obtained at 800 °C (Fig. 5E), with a micro/mesoporous structure and a relatively small specific surface area. The material displayed a positive onset potential and half wave potential which surpassed the performance of a commercial 20 wt.% (wt.% means weight percentage) Pt/C in alkaline environment, demonstrating that tea can be a great starting material for ORR electrocatalysts. A short stability test by chronoamperometry demonstrated that the electrocatalyst retained 93% of the starting cathodic current after 10 h. On the contrary, in the same testing conditions the commercial 20 wt.% Pt/C electrocatalyst retained only 85% of its initial current. The better electrocatalytic stability of the tea-derived electrocatalysts was attributed to the high degree of graphitization of the carbon matrix obtained during the pyrolysis step. Moreover, the electrocatalyst displayed also a stable amperometric response after the introduction of methanol in the solution, while the Pt/C suffered a sharp decrease of the current due to the reaction with methanol.

Hao et al. [197] prepared defective carbon materials with a so-called N-doping-removal process using sodium alginate derived from seaweed biomass. Seaweed-derived sodium alginate contains carboxyl and hydroxyls groups, which give rise to a 3D carbon structure by pyrolysis. The process involves doping and early removal of nitrogen atoms, obtaining an almost 100% porous carbon structure but with defects left in the position previously occupied by nitrogen, giving rise to a defective porous carbon. The pyrolysis at high temperature guarantees the stability of the structure. The content of defects, the characteristics of the pores, and electron conductivity of these materials depend on pyrolysis temperature and viscosity of sodium alginate. These parameters, in fact, influence the ORR activity. The most performing material, pyrolyzed at 900 °C, shows a highly defective porous structure with hierarchical porosity, good conductivity and a large specific surface area. The electrocatalyst exhibited good ORR activity in alkaline electrolyte, comparable to commercial Pt/C, but with better stability and methanol tolerance (Fig. 6A). This catalyst resulted also active in acid electrolyte, but in a lesser extent compared to Pt/C.

Eggplants were used by Zhou et al. [198] as a carbon source to synthetize N-doped porous graphene to outperform Pt/C electrocatalysts in alkaline media. Ultrahigh specific surface area graphene structure was obtained by two steps: first KOH activation for 24 h at room temperature. Then, first pyrolysis in Ar at 800 °C for 1 h to obtain porous graphene. The latter was then subjected to a second pyrolysis in Ar at 1 000 °C for 1.75 h, followed by a 1 min injection of NH_3 to obtain the final N-doped porous graphene (Fig. 6B), with a relatively high content of pyrrolic-N. No further treatments or extra metal addition was necessary to form an active electrocatalyst. Eggplants possess a unique porous-plate like structure that absorbs KOH solution helping the formation of ultrathin layers, suitable for the formation of porous graphene. Measured ORR activity appears to be slightly superior to that of commercial 20 wt.% Pt/C in alkaline condition, and in acidic condition as well, although the onset potential is lower. Moreover, also stability and methanol tolerance resulted higher than the commercial Pt/C. The combination of large specific surface area, high conductivity, and efficient nitrogen content due to the doping with NH_3, were associated to the good performance obtained.

The same group of Zhou et al. [199] used the same synthesis technique to prepare other ORR electrocatalysts starting from soybean shells, a quite common waste product in local Chinese markets. Soybean shells produce a highly porous graphene structure which possesses high conductivity and specific surface area. As for the case of eggplants, the role of ammonia is crucial in increasing N doping level, especially pyridinic-N, necessary to favor the formation of ORR active sites. The final electrocatalyst obtained reached a performance very similar to that of the commercial 20 wt.% Pt/C electrocatalyst, with a more stable performance after potential cycling and very good tolerance to methanol (Fig. 6C).

Soybean straws (Fig. 6D) have been used by Liu et al. [200] for the development of an electrocatalyst with honeycomb-like porous structure, co-doped with Fe and N. The process for the synthesis consists in a one-step pyrolysis of 2 h at 800 °C of the biomass together with melamine (N source), ferric nitrate (Fe source) and magnesium oxide as templating agent. A final leaching was performed to remove

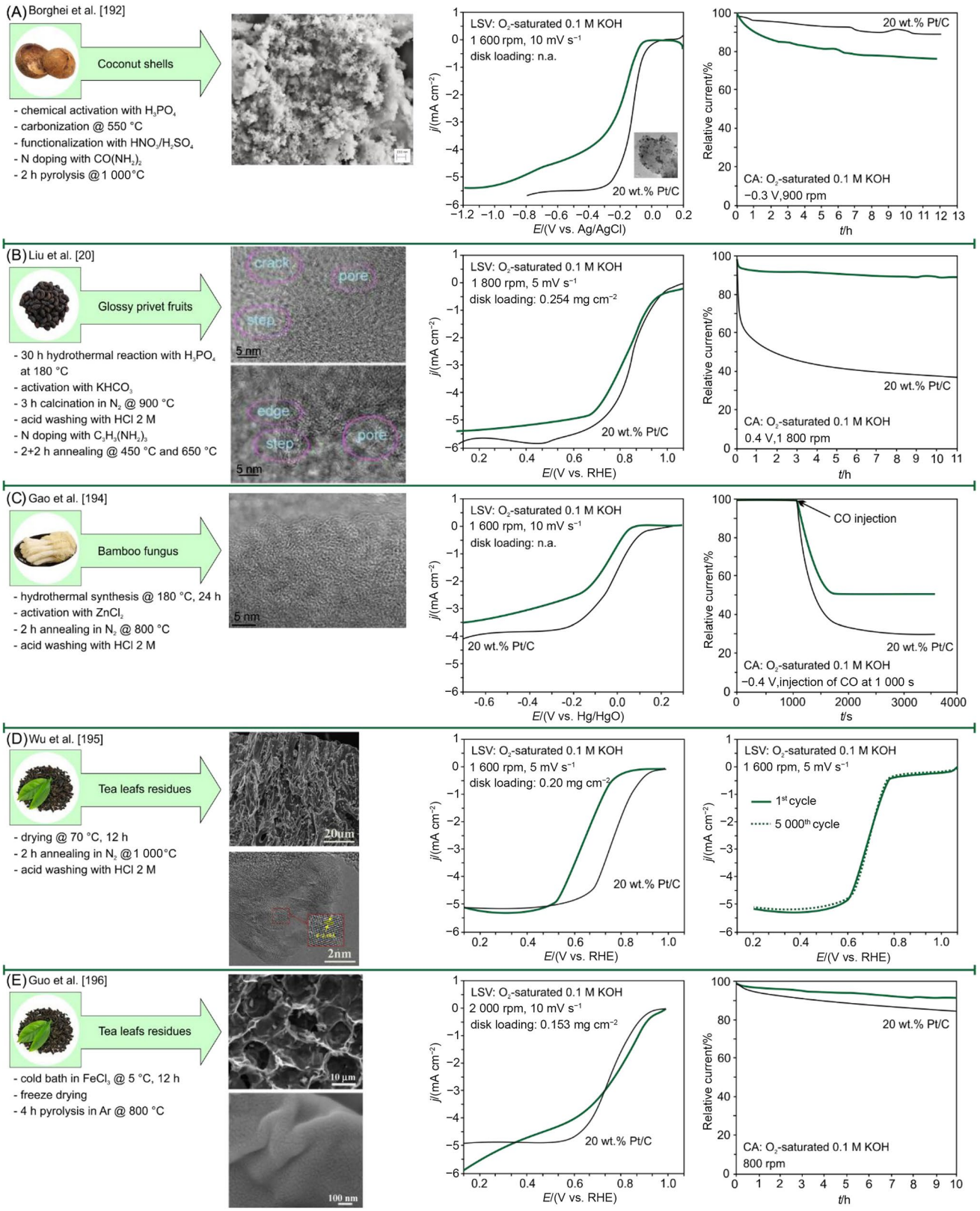

the templating agent. The resulting electrocatalyst shows a honeycomb-like porous structure (memory effect) composed of a graphitic carbon matrix encapsulating Fe_3C and Fe_3O_4 nanoparticles. The material exhibits interesting electrochemical properties, better in alkaline than in acid environment compared to the activity of a commercial Pt/C, with an

◂**Fig. 5** **A** Coconut-derived electrocatalysts: synthesis steps, SEM characterization, electrochemical characterization via LSV and CA. Reproduced with permission from Ref. [192]. Copyright © 2017, Elsevier **B** Glossy privet-derived electrocatalysts: synthesis steps, characterizations via SEM, LSV, and CA. Reproduced with permission from Ref. [20]. Copyright © 2020, American Chemical Society. **C** Bamboo fungus-derived electrocatalysts: synthesis steps, characterizations via TEM, LSV, and CA (with addition of CO in the solution). Reproduced with permission from Ref. [194]. Copyright © 2014, Royal Society of Chemistry. **D** Tea leaf-derived electrocatalyst: synthesis steps, characterizations via SEM and HRTEM, and LSV before and after potential cycling. Reproduced with permission from Ref. [195]. Copyright © 2018, Elsevier. **E** Tea leaf-derived electrocatalyst: synthesis method, characterizations via SEM, LSV and CA. Reproduced with permission from Ref. [196]. Copyright © 2016, Springer Nature

almost 4-electron process. Moreover, the material was more stable than a Pt/C counterpart, and also methanol tolerant.

Soybean dregs, a bio-waste from the industrial production of soybean milk (Fig. 6E), have been used by Yao et al. [19] for the development of an ORR electrocatalyst with favorable ORR electrocatalytic activity and superior durability than that of commercial Pt/C in alkaline medium, with outstanding methanol tolerance. After a pre-step of soybean dregs purification with H_2SO_4, the synthesis process consists in a one-step pyrolysis of 2 h at 800 °C of the pretreated biomass together with graphene oxide (produced from natural graphite with the modified Hummers' method), $Fe(C_2H_3O_2)_2$ and g-C_3N_4 (obtained by annealing urea in air at 500 °C). During the pyrolysis, the soybean dregs convert into a graphitic structure with a high number of edge planes and high degree of disorder. The final electrocatalysts possess a high content of pyridinic- and graphitic-N, as well as iron, which explain the good activity recorded towards ORR.

Srinu et al. [201] synthesized a series of ORR electrocatalysts starting from spent coffee grounds. After a carbonization process at 800 °C to obtain a porous structure, the porous carbon was co-doped with N and P using melamine and triphenyl phosphine. The ORR behavior of the dual doped material, with a high specific surface area, has been compared to that of commercial 20 wt.% Pt/C and showed higher electrocatalytic activity, with superior performance also to potential cycling and resistance to CO poisoning in alkaline medium (Fig. 7A). The porous network and the charge delocalization offered by the dopants is considered the reason of this behavior, together with the higher number of edge sites and high degree of disorder, mainly caused by P. In fact, phosphorus in the carbon lattice induces a high degree of open edge sites and defect sites, usually considered active sites for ORR.

Zhang et al. [202] obtained an active electrocatalyst from banana peels, which contains an intrinsically porous type of cellulose. The starting banana peels, after a pre-carbonization treatment, were grinded in a planetary ball mill and subsequently heat-treated at 800 °C with KOH activation, then 2 h final pyrolysis at 1 000 °C with ammonia injection in the last 15 min, with a procedure very similar to that adopted by Zhou et al. [198, 199] for treating eggplants. The final structure of the best electrocatalyst consists of at 3D defective porous carbon structure composed of graphene-like nanosheets with few layers, abundant of mesopores, high amount of pyridinic-N, and with an extremely high specific surface area. As ORR electrocatalyst, the onset and half-wave potential are very interesting both in acidic and alkaline environment, compared to a 20 wt.% Pt/C electrocatalyst, together with high stability, methanol tolerance, and CO poisoning resistance (Fig. 7B). This electrocatalyst has been successfully tested also as air electrode in a ZAB, reaching a peak power density of 208 mW cm^{-2}.

Pérez-Rodríguez et al. [203] prepared active ORR electrocatalysts starting from agricultural by-products such as dried aronia (DA) residues and peach stones (PS). First, activated carbons were prepared via carbonization and water steam activation of the two biomasses. Then, urea and iron nitrate, as cheap and abundant nitrogen and metal precursors, were added to the activated nanoporous carbons. Two thermal treatments of 1 h each at 950 °C in N_2 atmosphere, with intermediate acid lixiviation, allowed to obtain the final electrocatalysts (Fe–N–C–AR from aronia residues, Fe–N–C–PS from peach stones). The best activity in alkaline medium was recorded by testing the Fe–N–C–PS (Fig. 7C), with an activity only 20 mV far to a commercial 20 wt.% Pt/C electrocatalyst as half-wave potential. The best electrocatalyst, subjected to 4 000 potential cycling between 0.6 and 1.0 V vs. RHE, lost only 53 mV as half-wave potential. The good ORR activity and stability of the peach stone-derived electrocatalyst was attributed to the formation of graphitic planes during the carbonization of the starting biomass, as well as the presence of mesopores which favored the fixing of iron nanoparticles, and high content of pyridinic- and pyrrolic-N. In fact, by Mössbauer analysis, the Fe–N–C–PS resulted with the highest content of FeN_xC_y moieties, which are known to be active towards ORR [95].

Gao et al. [204] prepared a nitrogen-doped fullerene-like carbon shell material starting from ginkgo leaves, which were pyrolized for 2 h at 800 °C, followed by a simple washing with 2 M (1 M = 1 mol L^{-1}) HCl to remove metal residues. Considering the high natural content of N in the gingko leaves (from 10 to 15 wt.% of proteins content), no further doping of N is necessary to obtain an active electrocatalyst. The obtained material exhibits one of the rare examples of fullerene-like structure, namely N-C_{60}, (Fig. 7D). In fact, the structure contains graphene flakes and fullerene-like cavities, with graphitic crystallites able to integrate N. The integration of N atoms changes the structure favoring the formation of a ring structure, mostly pentagonal. As a consequence, the structure results to be more active than the basal

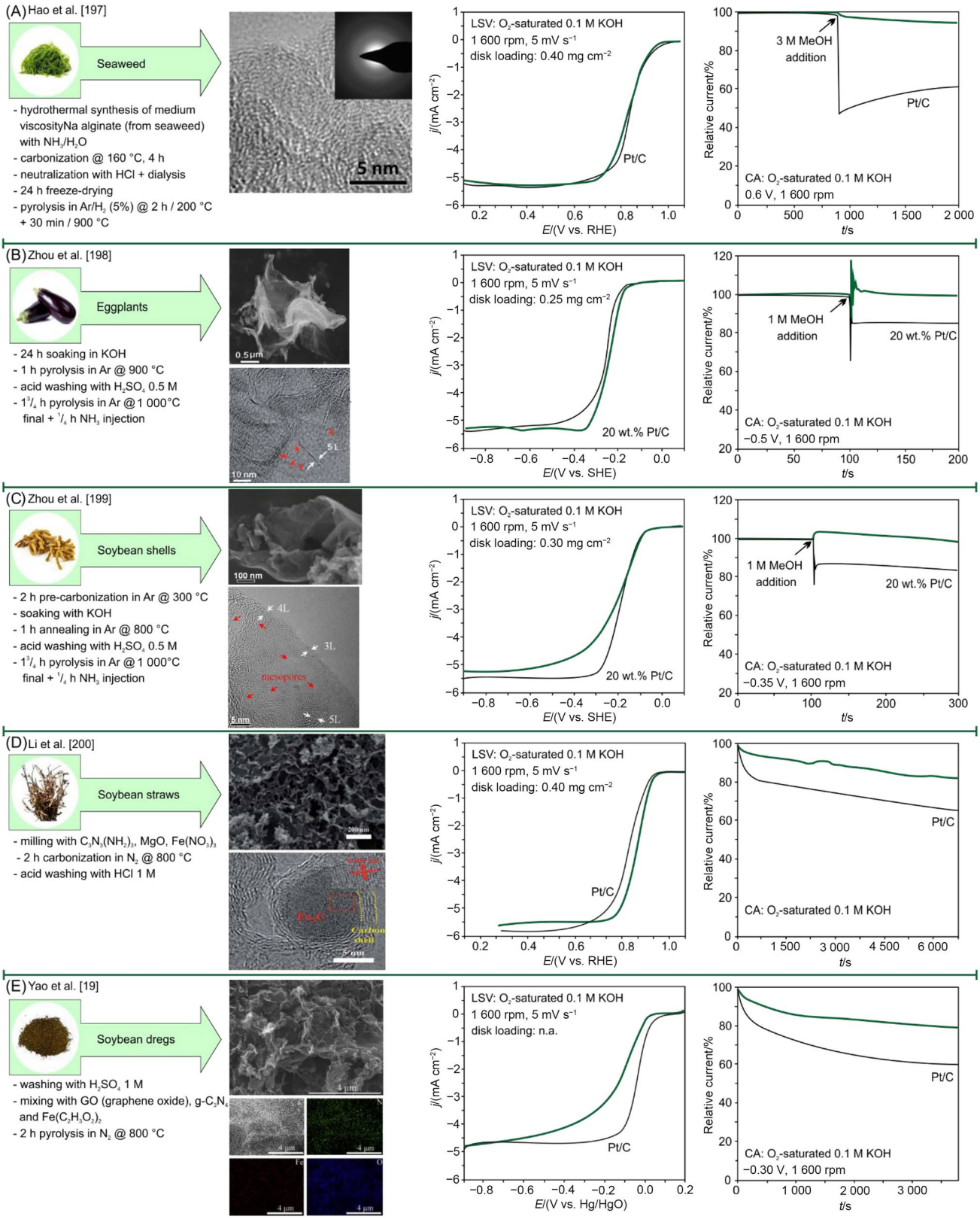
(A) Hao et al. [197]
Seaweed
- hydrothermal synthesis of medium viscosityNa alginate (from seaweed) with NH_3/H_2O
- carbonization @ 160 °C, 4 h
- neutralization with HCl + dialysis
- 24 h freeze-drying
- pyrolysis in Ar/H_2 (5%) @ 2 h / 200 °C + 30 min / 900 °C
5 nm
LSV: O_2-saturated 0.1 M KOH
1 600 rpm, 5 mV s^{-1}
disk loading: 0.40 mg cm^{-2}
Pt/C
j/(mA cm^{-2})
E/(V vs. RHE)
3 M MeOH addition
Pt/C
CA: O_2-saturated 0.1 M KOH
0.6 V, 1 600 rpm
Relative current/%
t/s
(B) Zhou et al. [198]
Eggplants
- 24 h soaking in KOH
- 1 h pyrolysis in Ar @ 900 °C
- acid washing with H_2SO_4 0.5 M
- 1 3/4 h pyrolysis in Ar @ 1 000 °C final + 1/4 h NH_3 injection
0.5 μm
10 nm
5 L
LSV: O_2-saturated 0.1 M KOH
1 600 rpm, 5 mV s^{-1}
disk loading: 0.25 mg cm^{-2}
20 wt.% Pt/C
j/(mA cm^{-2})
E/(V vs. SHE)
1 M MeOH addition
20 wt.% Pt/C
CA: O_2-saturated 0.1 M KOH
−0.5 V, 1 600 rpm
Relative current/%
t/s
(C) Zhou et al. [199]
Soybean shells
- 2 h pre-carbonization in Ar @ 300 °C
- soaking with KOH
- 1 h annealing in Ar @ 800 °C
- acid washing with H_2SO_4 0.5 M
- 1 3/4 h pyrolysis in Ar @ 1 000 °C final + 1/4 h NH_3 injection
100 nm
4L
3L
mesopores
5 nm
5L
LSV: O_2-saturated 0.1 M KOH
1 600 rpm, 5 mV s^{-1}
disk loading: 0.30 mg cm^{-2}
20 wt.% Pt/C
j/(mA cm^{-2})
E/(V vs. SHE)
1 M MeOH addition
20 wt.% Pt/C
CA: O_2-saturated 0.1 M KOH
−0.35 V, 1 600 rpm
Relative current/%
t/s
(D) Li et al. [200]
Soybean straws
- milling with $C_3N_3(NH_2)_3$, MgO, $Fe(NO_3)_3$
- 2 h carbonization in N_2 @ 800 °C
- acid washing with HCl 1 M
200nm
5 nm
Fe_3C
Carbon shell
LSV: O_2-saturated 0.1 M KOH
1 600 rpm, 5 mV s^{-1}
disk loading: 0.40 mg cm^{-2}
Pt/C
j/(mA cm^{-2})
E/(V vs. RHE)
Pt/C
CA: O_2-saturated 0.1 M KOH
Relative current/%
t/s
(E) Yao et al. [19]
Soybean dregs
- washing with H_2SO_4 1 M
- mixing with GO (graphene oxide), g-C_3N_4 and $Fe(C_2H_3O_2)_2$
- 2 h pyrolysis in N_2 @ 800 °C
4 μm
Fe
O
LSV: O_2-saturated 0.1 M KOH
1 600 rpm, 5 mV s^{-1}
disk loading: n.a.
Pt/C
j/(mA cm^{-2})
E/(V vs. Hg/HgO)
Pt/C
CA: O_2-saturated 0.1 M KOH
−0.30 V, 1 600 rpm
Relative current/%
t/s

◂**Fig. 6** **A** Seaweed-derived electrocatalysts: synthesis steps, FESEM and HR-TEM characterization, electrochemical characterization via LSV and CA with methanol addition. Reproduced with permission from Ref. [197]. Copyright © 2018, Elsevier. **B** Eggplant-derived electrocatalysts: synthesis steps, characterizations via FESEM and HRTEM, LSV, and CA. Reproduced with permission from Ref. [198]. Copyright © 2016, Royal Society of Chemistry. **C** Soybean shell-derived electrocatalysts: synthesis steps, FESEM and HR-TEM characterization, electrochemical characterization via LSV and CA with methanol addition. Reproduced with permission from Ref. [199]. Copyright © 2016, Royal Society of Chemistry. **D** Soybean straw-derived electrocatalysts: synthesis steps, SEM and HR-TEM characterization, electrochemical characterization via LSV and CA. Reproduced with permission from Ref. [200]. Copyright © 2020, Royal Society of Chemistry. **E** Soybean dreg-derived electrocatalysts: synthesis steps, SEM and EDX characterization, electrochemical characterization via LSV and CA. Reproduced with permission from Ref. [19]. Copyright © 2020, Elsevier

plane of graphitic carbon. Interestingly, here the fullerene-like structure can be obtained at relatively low temperature (800 °C instead of 3 000 °C) thanks to the presence of N, which promotes the rearrangement of the C atoms at lower temperature compared to pure non-doped carbon. In terms of electrochemical performance, this fullerene-like electrocatalyst shows high values of onset and half-wave potential in alkaline environment, only slightly smaller compared to a commercial 20 wt.% Pt/C, as well as good stability. Moreover, it is almost 100% selective towards 4-electron ORR pathway. An accelerated stability test was conducted by CA, showing the better stability of the biomass-derived electrocatalyst compared to Pt/C.

Catkins produced by willow, a cosmopolitan plant, were used by Li et al. [205] for the synthesis of porous carbon fibers (PCFs), that were subsequently doped with melamine and ferric chloride to form Fe, N-doped carbon nanotubes Fe/N/CNT@PFCs), as shown in Fig. 7E. The Fe/N/CNT@PFC structure is constituted by a series of hollow carbon fibers with diameters of 2–5 µm, where both the inner and outer walls of the hollow carbon fibers are covered by large amounts of CNTs. Overall, the specific surface area results relatively high, with a high content of pyridinic-N, thanks to the double role of both melamine and $FeCl_3$ precursors. In fact, they catalyzed the growth of nanotubes enabling high specific surface area and porous structure, but they also facilitated the transformation of N species to pyridinic- and pyrrolic-N, enhancing the ORR activity. The high electrochemical activity of the electrocatalyst is confirmed in both alkaline and acidic media compared to a 20 wt.% Pt/C electrocatalyst. The electrocatalyst also proved to be more stable than Pt/C.

Edible substances such as spinaches, onions, and yeast [40, 206–208] have been widely studied as well. As an example, Zhang et al. [208] developed hierarchically porous nitrogen and sulfur dual-doped carbon nanosheet networks, with a procedure involving the pyrolysis of onion (*Allium cepa*) chips impregnated with thiourea and KOH. N and S elements are naturally present in the starting biomass in relatively high percentage, thus they give origin to a large number of electrocatalytically active sites (such as pyridinic- and quaternary-N and thiophene-S), together with a porous structure. Such a structure has a hierarchically layered architecture, due to the naturally layered structure of *Allium cepa* (memory effect), and ultra-large specific surface area. The positive onset and half-wave potentials obtained with the final electrocatalyst (Fig. 8A) in alkaline conditions are proof of good activity toward ORR, with a better stability compared to a commercial 20 wt.% Pt/C catalyst. The electrocatalyst has also been tested in a ZAB, outperforming the commercial Pt/C electrocatalyst in terms of discharge current density, peak power density (221 mW cm^{-2}), specific capacity, rate performance and open circuit potential.

Wang et al. [207] worked with brewer's yeast powder (BYP), a by-product of brewing beer industry, as a natural source rich of C, N, and P atoms to obtain a high-performance, spherical, heteroatom-doped Fe–N–P–C electrocatalyst. The synthesis procedure consists in a hydrothermal treatment process and subsequent double pyrolysis with acid leaching starting from BYP, ferric chloride, and ammonium hydroxide as precursors. The resulting final electrocatalyst is composed of spherical hollow carbon aggregates with a rough surface covered of small sheet-like nanoparticles, and a high content of pyridinic- and graphitic-N. The electrochemical properties show a better ORR performance in alkaline medium compared to that of 20 wt.% Pt/C (Fig. 8B). Moreover, the BPY-Fe electrocatalyst resulted to be highly tolerant to methanol, and more stable compared to Pt/C.

Spinach derived electrocatalysts were synthetized by Liu et al. [40]. Spinaches were selected as a natural source of C, Fe, and N atoms. Moreover, they also contain small amounts of S and P atoms, both considered as effective dopants and activity enhancer for ORR active sites. The synthesis forecasts a freeze-dry process of the spinaches, followed by an addition of melamine as a further N promoter, and NaCl/KCl as micro- and meso-pores former to increase the porosity of the final electrocatalyst (Fig. 8C). After two pyrolysis steps in Ar at 900 °C each, with an intermediate acid leaching treatment, the resulting material possesses graphene-like carbon sheet-like structure full of defects and wrinkles, with a high content of pyridinic- and graphitic-N, and traces of thiophene S, which is also known to be active towards ORR [210]. The obtained material, tested both in acid and alkaline media, outperformed a commercial Pt/C electrocatalyst, especially in terms of short and long term use (up to 60 days of storage in alkaline solution). The higher activity and stability originate from the abundance of Fe-N_x active centers, as well a highly mesoporous structure. It is interesting to note in this work the choice of a plant already containing Fe, an approach that could be used with other biomass to

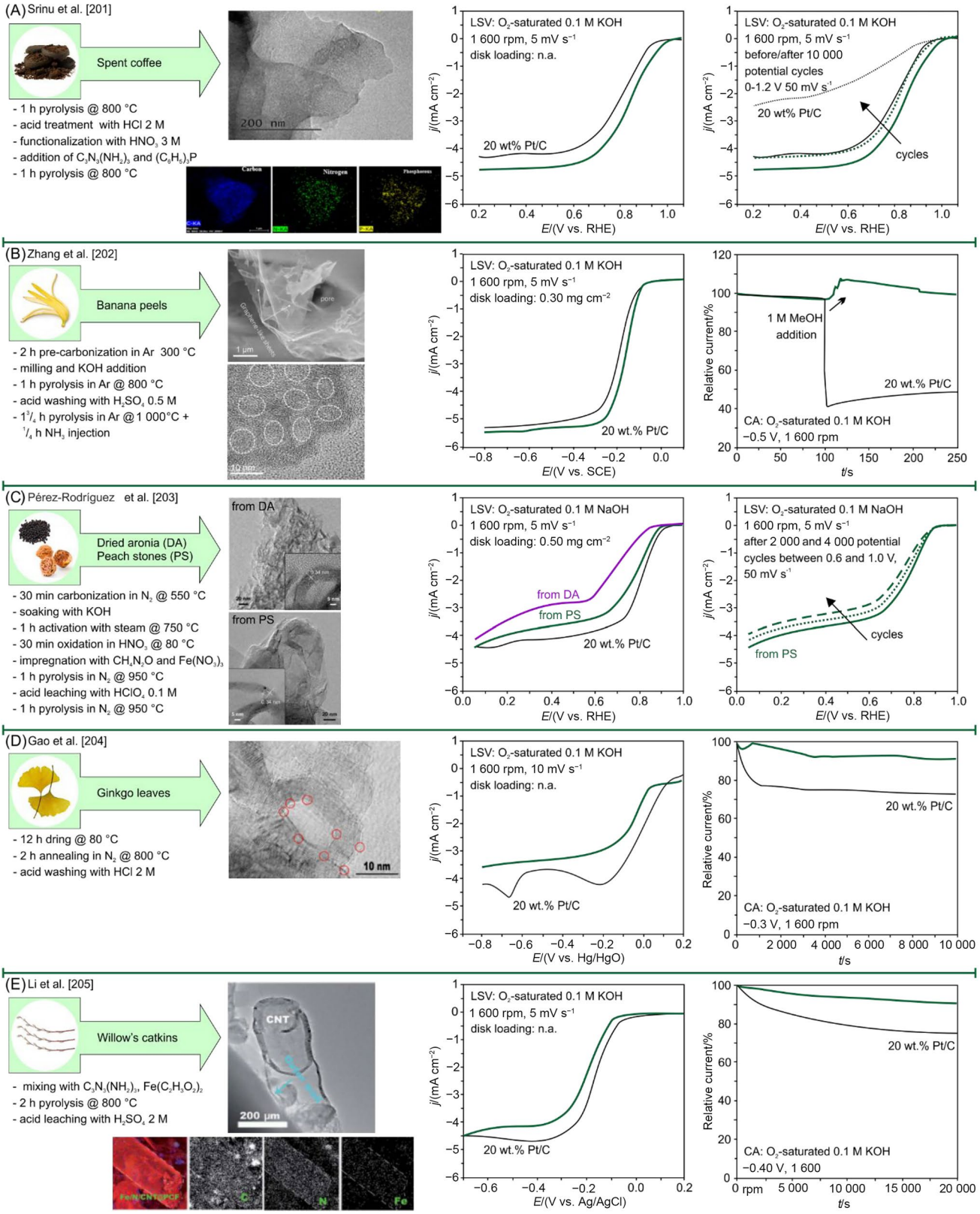
(A) Srinu et al. [201]
Spent coffee
- 1 h pyrolysis @ 800 °C
- acid treatment with HCl 2 M
- functionalization with HNO3 3 M
- addition of C3N3(NH2)3 and (C6H5)3P
- 1 h pyrolysis @ 800 °C
200 nm
Carbon
Nitrogen
Phosphorous
LSV: O2-saturated 0.1 M KOH
1 600 rpm, 5 mV s−1
disk loading: n.a.
20 wt% Pt/C
j/(mA cm−2)
E/(V vs. RHE)
LSV: O2-saturated 0.1 M KOH
1 600 rpm, 5 mV s−1
before/after 10 000
potential cycles
0-1.2 V 50 mV s−1
20 wt% Pt/C
cycles
(B) Zhang et al. [202]
Banana peels
- 2 h pre-carbonization in Ar 300 °C
- milling and KOH addition
- 1 h pyrolysis in Ar @ 800 °C
- acid washing with H2SO4 0.5 M
- 1 3/4 h pyrolysis in Ar @ 1 000°C +
1/4 h NH3 injection
pore
Graphene-like sheets
1 μm
10 nm
LSV: O2-saturated 0.1 M KOH
1 600 rpm, 5 mV s−1
disk loading: 0.30 mg cm−2
20 wt.% Pt/C
E/(V vs. SCE)
1 M MeOH
addition
20 wt.% Pt/C
CA: O2-saturated 0.1 M KOH
−0.5 V, 1 600 rpm
Relative current/%
t/s
(C) Pérez-Rodríguez et al. [203]
Dried aronia (DA)
Peach stones (PS)
- 30 min carbonization in N2 @ 550 °C
- soaking with KOH
- 1 h activation with steam @ 750 °C
- 30 min oxidation in HNO3 @ 80 °C
- impregnation with CH4N2O and Fe(NO3)3
- 1 h pyrolysis in N2 @ 950 °C
- acid leaching with HClO4 0.1 M
- 1 h pyrolysis in N2 @ 950 °C
from DA
from PS
LSV: O2-saturated 0.1 M NaOH
1 600 rpm, 5 mV s−1
disk loading: 0.50 mg cm−2
from DA
from PS
20 wt.% Pt/C
LSV: O2-saturated 0.1 M NaOH
1 600 rpm, 5 mV s−1
after 2 000 and 4 000 potential
cycles between 0.6 and 1.0 V,
50 mV s−1
cycles
from PS
(D) Gao et al. [204]
Ginkgo leaves
- 12 h dring @ 80 °C
- 2 h annealing in N2 @ 800 °C
- acid washing with HCl 2 M
10 nm
LSV: O2-saturated 0.1 M KOH
1 600 rpm, 10 mV s−1
disk loading: n.a.
20 wt.% Pt/C
E/(V vs. Hg/HgO)
20 wt.% Pt/C
CA: O2-saturated 0.1 M KOH
−0.3 V, 1 600 rpm
(E) Li et al. [205]
Willow's catkins
- mixing with C3N3(NH2)3, Fe(C2H3O2)2
- 2 h pyrolysis @ 800 °C
- acid leaching with H2SO4 2 M
CNT
200 μm
Fe/NCNT/PCF
C
N
Fe
LSV: O2-saturated 0.1 M KOH
1 600 rpm, 5 mV s−1
disk loading: n.a.
20 wt.% Pt/C
E/(V vs. Ag/AgCl)
20 wt.% Pt/C
CA: O2-saturated 0.1 M KOH
−0.40 V, 1 600
rpm

◂**Fig. 7** **A** Spent coffee ground-derived electrocatalysts: synthesis steps, HR-TEM and EDAX characterization, electrochemical characterization via LSV before and after 10 000 potential cycles. Reproduced with permission from Ref. [201]. Copyright © 2018, John Wiley and Sons. **B** Banana peel-derived electrocatalysts: synthesis steps, characterizations via SEM and TEM, LSV, and CA. Reproduced with permission from Ref. [202]. Copyright © 2017, Elsevier. **C** Aronia dried (AD) and peach stones (PS) derived electrocatalysts: synthesis steps, TEM characterization, electrochemical characterization via LSV before and after 4 000 potential cycles. Reproduced with permission from Ref. [203]. Copyright © 2021, The Author(s). Published by Elsevier Ltd. **D** Ginkgo leaf-derived electrocatalysts: synthesis steps, SEM and HR-TEM characterization, electrochemical characterization via LSV and CA. Reproduced with permission from Ref. [204]. Copyright © 2015, Elsevier. **E** Willow's catkin-derived electrocatalysts: synthesis steps, TEM and EDS characterization, electrochemical characterization via LSV and CA. Reproduced with permission from Ref. [205]. Copyright © 2015, Royal Society of Chemistry

avoid the doping step to form the desired active sites in the final electrocatalysts.

Wu et al. [39] obtained a nitrogen doped graphitic carbon from a biomass derived from microalgae, easily found in rivers and acting as a good carbon source. To achieve the N doping, ammonia is used during the pyrolytic process and iron salts are introduced as catalysts for the synthesis. The combination of iron carbide and graphitic C layers leads to activity towards ORR in alkaline environment, as shown by electrochemical tests (Fig. 8D). The performance does not decrease after 10 000 potential cycles, meaning this electrocatalyst is able to outperform commercial Pt/C in terms of stability.

Zheng et al. [209] obtained performing electrocatalysts by pyrolysis of soybean beancurd with addition of NaCl as a catalyst and urea to reach high N-doping level (5.02 at.%) (at.% means atomic percentage) and hierarchically porous structure (Fig. 8E). Urea acts as an extra nitrogen source, while NaCl acts as a green template tuning both porosity and morphology, bringing to a structure composed of interconnected nanosheets. Due to the presence of minor gypsum in the starting biomass as a coagulator, the synthesis requires a further step between the two pyrolysis, with the addition of a solution of sodium carbonate, to remove the gypsum. The final electrocatalyst reached the benchmark established performance of a commercial Pt/C electrocatalyst, outperforming the stability of the commercial one. The good performance is attributed to the high content of N species, particularly pyridinic-N and graphitic-N, as well as the porous 3D hierarchical structure from micro- to macro-scale, that allows an efficient mass transfer of oxygen. The electrocatalyst was also employed in a ZAB displaying good power density (peak power density of 207.5 mW cm^{-2}), specific capacity and rate capability compared to the noble metal.

Conversion of Sengon wood to reduced graphene oxide (RGO) has been achieved by Sudarsono and co-workers [211]. In fact, RGO is one of the key emerging carbon supports. Sengon wood is an abundant bio-resource, which paves the way to the production of efficient electrocatalysts from natural resources. Sengon wood-derived RGO has a sheet-like structure and many defect sites, as well as low oxygen content and a high degree of graphitization. All of these characteristics are desired features for an electrocatalyst support (Fig. 9A). The obtained RGO, when treated with ferric chloride and choline chloride, $[(CH_3)_3NCH_2CH_2OH]Cl$, and subjected to pyrolysis at 900 °C, allows anchoring and doping of iron and nitrogen particles on the surface. The performance is comparable of that of a commercial Pt/C electrocatalyst, also in terms of stability, but with better tolerance to methanol. The good activity of this electrocatalyst can be ascribed to its morphology and elemental composition. This specific RGO possesses a defective graphene sheet-like structure, which in principle should favor the formation of active sites. This morphology favors the adsorption of choline chloride during the synthesis, which is a highly water-miscible organic salt containing nitrogen, thus able to penetrate deeply the complex porous matrix of the Sengon wood. Thus, during the pyrolysis, the organic salt in the RGO matrix is able to better fix the nitrogen, and favor also the anchoring of Fe from the ferric chloride, giving rise to a highly active electrocatalyst.

Guo et al. [212] tested a metal free electrocatalyst obtained from protein-rich enoki mushrooms (*Flammulina velutipes*) mixed with carbon nanotubes (CNTs) in alkaline and acidic conditions (Fig. 9B). The easy and low-cost synthesis consists only in drying the biomass, mixing with CNT to increase the conductivity of the final material, and pyrolyzing at 900 °C. The biomass acts both as a C atom and heteroatom source, while the nanotubes act as structural matrix for the structure. In terms of ORR activity, the performance was better than a commercial Pt/C only in alkaline environment, but the stability was superior both in alkaline and acid electrolyte. The authors suggest that the good performance of the electrocatalyst can be linked with the high percentage of graphitic- and pyrrolic-N in the carbon lattice, which act as active sites towards the direct 4-electron ORR.

Zhang et al. [213] presented a facile, environmentally friendly and low cost method to obtain high quality nitrogen-doped carbon nanodot/nanosheet aggregates (N-CNAs) from dried monkey grass (*Ophiopogon japonicus*). The synthesis required only a hydrothermal treatment at 180 °C of the sole dried grass, without the addition of synthetic chemicals and without the pyrolysis step (Fig. 9C). The fabricated N-CNAs have an N/C atomic ratio of 3.41%, subdivided into pyridinic-, pyrrolic-, and graphitic-N, with pyridinic-N in the highest content. Experimental results showed that the ORR performance is very similar to that of a commercial Pt/C

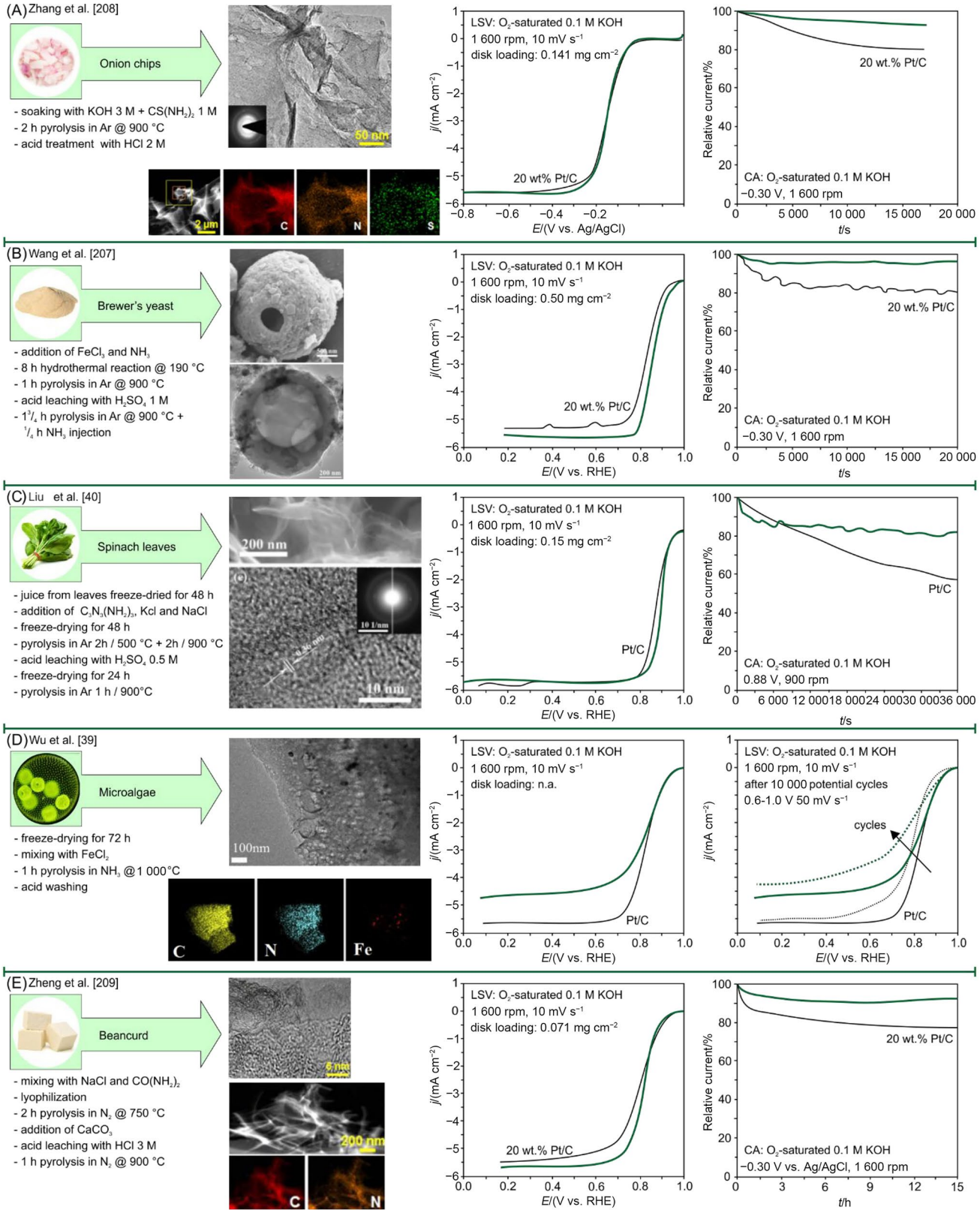

electrocatalyst, following a 4-electron pathway, but stability and methanol tolerance are superior. Theoretical studies conducted by density functional theory (DFT) explained that pyridinic-N has a higher positive charge, which favors O_2 adsorption on the electrocatalyst's surface, with an enhanced ORR performance. Moreover, DFT calculations

◂**Fig. 8** **A** Onion chip-derived electrocatalysts: synthesis steps, HR-TEM and EDAX characterization, electrochemical characterization via LSV and CA. Reproduced with permission from Ref. [208]. Copyright © 2020, Springer Nature. **B** Brewer yeast-derived electrocatalysts: synthesis steps, SEM and TEM characterization, electrochemical characterization via LSV and CA. Reproduced with permission from Ref. [207]. Copyright © 2016, Elsevier. **C** Spinach derived-electrocatalysts: synthesis steps, SEM and TEM characterization, electrochemical characterization via LSV and CA. Reproduced with permission from Ref. [40]. Copyright © 2020, American Chemical Society. **D** Microalgae-derived electrocatalysts: synthesis steps, TEM and EDS characterization, electrochemical characterization via LSV before and after potential cycling. Reproduced with permission from Ref. [39]. Copyright © 2019, Elsevier. **E** Beancurd-derived electrocatalysts: synthesis steps, STEM and EDS characterization, electrochemical characterization via LSV and CA. Reproduced with permission from Ref. [209]. Copyright © 2020, The Electrochemical Society. Published by IOP Publishing, Ltd.

also confirmed that O_2 adsorption on pyridinic-N is stronger compared to the other types of N. Indeed, the 4-electron ORR process can be explained with the mechanism of dissociative adsorption of O_2 molecules.

Xiao et al. [214] synthetized a tri-heteroatom (N, S, O) co-doped porous electrocatalyst from China Rose petals, showing promising electroactivity both in acidic and alkaline environment. China rose is a perennial evergreen shrub, which can easily grow and bloom anywhere and almost all year-round. The petals of the flower have an interesting hierarchical micro- and nano-structure that can be easily maintained during the preparation of the carbons (memory effect). Moreover, China rose has a high content of magnesium and potassium salts, which can rise to a high porosity during the pyrolysis. Indeed, the saccharides and amino-acids present in the petals favor the formation of a naturally doped carbon matrix rich in N, S and O atoms. The synthesis process involved a freeze dry step of petals, followed by pre-carbonization, KOH activation, and two steps of pyrolysis with an intermediate addition of melamine. The final electrocatalyst presented a high activity, comparable to that of a Pt/C electrocatalyst in alkaline medium, and only slightly lower in acid environment. Interestingly, the electrocatalyst showed much better stability, and high tolerance to the presence of methanol. The ORR performance has been ascribed to a synergistic effect of the hierarchical micro- and meso-porous structure, together with the co-doping of S, N, and O heteroatoms (Fig. 9D).

Typha orientalis, also known as cattail or bulrush, is a conveniently available plant that grows easily on the edges of ponds, lakes and slow flowing rivers and streams. Chen et al. [215] deployed a simple hydrothermal process using pyrolysis in ammonia gas to obtain a metal free electrocatalyst with high specific surface area and numerous micropores, without the addition of extra-chemicals for doping the carbon-based matrix (Fig. 9E). The final structure consists of a series of highly N-doped carbon nanosheets (with a high N content, most of it as pyridinic- and pyrrolic-N), thanks to the pyrolysis conducted in ammonia. Interestingly, the pyrolysis leads to the formation of an oil, which was considered helpful for the formation of the final microporous structure thanks to an etching effect on the carbon matrix. Tests conducted to characterize ORR activity both in alkaline and acidic environment showed a highly active electrocatalyst, with a performance comparable to that of a commercial Pt/C, especially in alkaline medium. Indeed, the ORR activity was superior in terms of stability, evaluated by chronoamperometry in the presence of methanol, both in acid and alkaline environment.

Liu et al. [216] obtained a low-cost electrocatalyst from natural and cheap osmanthus fruits, which are rich in N, S and P heteroatoms, with the addition of dicyandiamide and ferric sulfate as additives (Fig. 10A). N, P, and S are naturally present in the sweet fruit, thus the process requires only a hydrothermal synthesis, and a fast pyrolysis in ammonia after the addition of the extra chemicals. SEM analysis confirms the final electrocatalyst has a nano-porous carbon structure rich of carbon nanotubes. The use of both dicyandiamide and ferric sulfate increases significantly the amount of micro- and meso-pores, compared to similar electrocatalysts produced without, or using only one of the two chemicals. This result suggests a synergistically action when the two additives are used together. The three heteroatoms remain present in the final electrocatalyst. The electrochemical activity was comparable to that of a commercial 47.6 wt.% Pt/C in alkaline conditions, while in acid the performance was slightly lower. The electrocatalysts resulted also very stable in both environments, and also methanol tolerant.

Hierarchical porous carbon was obtained by Kong et al. [217] using waste biomass from pomelo peels mixed with graphene oxide (GO) in a rate of 1 mg of GO every gram of pomelo peel (Fig. 10B). After a simple hydrothermal reaction, and a 2 day freeze-drying process, the resulting biomass was pyrolyzed in ammonia atmosphere, without any further treatment. The absence of any acid or basic precursors makes this synthesis environmentally friendly and simple, and leads to a N-doped structure with an extremely high specific surface area. The final electrocatalysts possess a network porous structure with high conductivity, mainly due to the presence of reduced graphene oxide (RGO). Electrochemical tests demonstrated a considerable activity in both alkaline and acid environment, as well as long term durability and methanol tolerance, with an almost 4-electron pathway reaction.

Bagasse is a waste that remains after crushing sugarcane or sorghum stalks to extract their juice. As an environmental waste, it is extremely abundant and low cost, thus Yuan and coworkers [218] used it to produce ORR electrocatalysts active in both acid and alkaline electrolyte (Fig. 10C). The ease synthesis consists only in a freeze drying step followed by a pyrolysis in ammonia flow, without any further

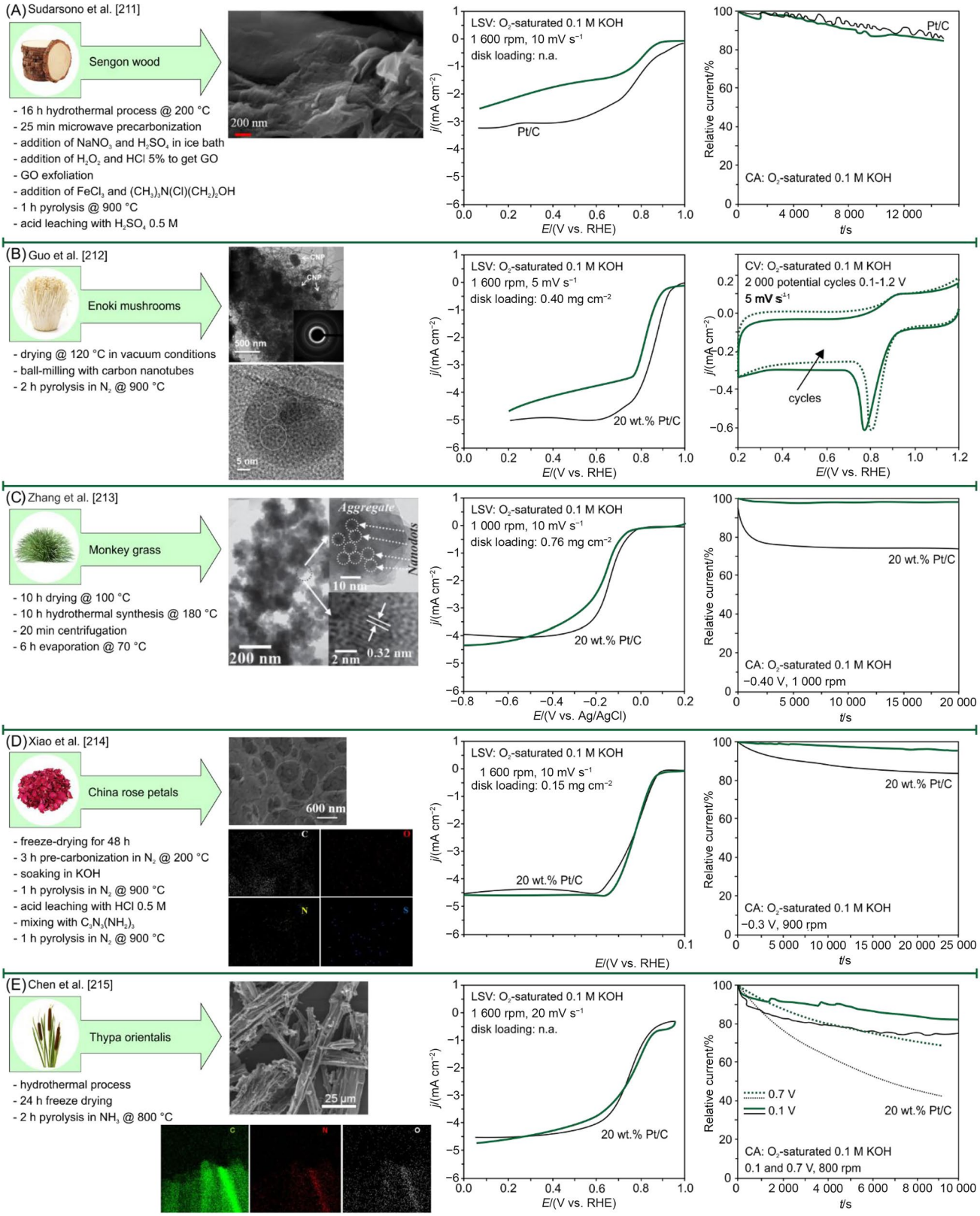
(A) Sudarsono et al. [211]
Sengon wood
- 16 h hydrothermal process @ 200 °C
- 25 min microwave precarbonization
- addition of NaNO3 and H2SO4 in ice bath
- addition of H2O2 and HCl 5% to get GO
- GO exfoliation
- addition of FeCl3 and (CH3)3N(Cl)(CH2)2OH
- 1 h pyrolysis @ 900 °C
- acid leaching with H2SO4 0.5 M
200 nm
LSV: O2-saturated 0.1 M KOH
1 600 rpm, 10 mV s−1
disk loading: n.a.
Pt/C
j/(mA cm−2)
E/(V vs. RHE)
Relative current/%
CA: O2-saturated 0.1 M KOH
t/s
(B) Guo et al. [212]
Enoki mushrooms
- drying @ 120 °C in vacuum conditions
- ball-milling with carbon nanotubes
- 2 h pyrolysis in N2 @ 900 °C
CNP
500 nm
5 nm
LSV: O2-saturated 0.1 M KOH
1 600 rpm, 5 mV s−1
disk loading: 0.40 mg cm−2
20 wt.% Pt/C
CV: O2-saturated 0.1 M KOH
2 000 potential cycles 0.1-1.2 V
5 mV s−1
cycles
(C) Zhang et al. [213]
Monkey grass
- 10 h drying @ 100 °C
- 10 h hydrothermal synthesis @ 180 °C
- 20 min centrifugation
- 6 h evaporation @ 70 °C
Aggregate
Nanodots
10 nm
200 nm
2 nm
0.32 nm
LSV: O2-saturated 0.1 M KOH
1 000 rpm, 10 mV s−1
disk loading: 0.76 mg cm−2
20 wt.% Pt/C
E/(V vs. Ag/AgCl)
CA: O2-saturated 0.1 M KOH
−0.40 V, 1 000 rpm
(D) Xiao et al. [214]
China rose petals
- freeze-drying for 48 h
- 3 h pre-carbonization in N2 @ 200 °C
- soaking in KOH
- 1 h pyrolysis in N2 @ 900 °C
- acid leaching with HCl 0.5 M
- mixing with C3N3(NH2)3
- 1 h pyrolysis in N2 @ 900 °C
600 nm
C
O
N
S
LSV: O2-saturated 0.1 M KOH
1 600 rpm, 10 mV s−1
disk loading: 0.15 mg cm−2
20 wt.% Pt/C
CA: O2-saturated 0.1 M KOH
−0.3 V, 900 rpm
(E) Chen et al. [215]
Thypa orientalis
- hydrothermal process
- 24 h freeze drying
- 2 h pyrolysis in NH3 @ 800 °C
25 μm
C
N
O
LSV: O2-saturated 0.1 M KOH
1 600 rpm, 20 mV s−1
disk loading: n.a.
20 wt.% Pt/C
0.7 V
0.1 V
CA: O2-saturated 0.1 M KOH
0.1 and 0.7 V, 800 rpm

◂**Fig. 9** **A** Sengon wood-derived electrocatalysts: synthesis steps, FE-SEM characterization, electrochemical characterization via LSV and CA. Reproduced with permission from Ref. [211]. Copyright © 2019, John Wiley and Sons. **B** Enoki mushroom-derived electrocatalysts: synthesis steps, HR-TEM characterization, electrochemical characterization via LSV and CV. Reproduced with permission from Ref. [212]. Copyright © 2015, Royal Society of Chemistry. **C** Monkey grass-electrocatalysts: synthesis steps, HR-TEM characterization, electrochemical characterization via LSV and CA. Reproduced with permission from Ref. [213]. Copyright © 2014, John Wiley and Sons. **D** China rose petals-electrocatalysts: synthesis steps, FESEM and EDX characterization, electrochemical characterization via LSV and CA. Reproduced with permission from Ref. [214]. Copyright © 2016, Royal Society of Chemistry. **E** *Thypa orientalis* flower spike-derived electrocatalysts: synthesis steps, SEM and EDX characterization, electrochemical characterization via LSV and CA. Reproduced with permission from Ref. [215]. Copyright © 2014, Royal Society of Chemistry

treatment or addition of extra chemicals. The obtained carbon-based structure presents a two-dimensional sheet structure with a curved shape, resulting from the original structure of bagasse (memory effect), mainly constituted of disordered and amorphous carbon. The specific surface area is extremely high, and rich of incorporated nitrogen, mainly graphitic- and, in lower extent, pyridinic-N. The electrochemical activity towards ORR is very similar to that of a commercial Pt/C in alkaline medium, while in acid it is lower. The stability and methanol tolerance are better compared to the commercial electrocatalyst, in both electrolytes.

An ORR active electrocatalyst was obtained from corn starch by Zhao and coworkers [219] by simple pyrolysis with urea, with two steps of temperature, first at 550 °C and then at 1 000 °C (Fig. 10D). Except for the addition of urea, no other chemicals were used in the synthesis. The slow pyrolysis, with the intermediate step at 550 °C, aimed at increasing the N doping level during the formation of carbon nanosheets. In fact, at this intermediate temperature, urea decomposes to NH_3 and forms graphene-like carbon nitride C_3N_4 sheets, which can act as template agents. Thus, ammonia formation can trigger the N-doping of the biomass-derived carbon matrix. When the temperature raises during the second step of the pyrolysis, at around 700 °C the amorphous carbon starts crystallizing on the layered g-C_3N_4 sheets previously formed, forming a nanosheets structure rich of N in the form on $C_2N_2^+$, $C_3N_2^+$, and $C_3N_3^+$. Thus, the layered g-C_3N_4 sheets act as sacrificial templates, providing the morphological structure to the carbon, which results highly doped in N. The final resulting material has a high degree of crystallization and graphitization, with a very high specific surface area, rich of meso- and macro-pores. The overall N content is high, in prevalence graphitic-N. The activity of the electrocatalyst is very similar to that of the commercial Pt/C in alkaline medium, slightly lower in acid medium, while the stability and methanol tolerance are better.

Li et al. [119] synthetized a series of Fe,P-doped electrocatalysts derived from various pine woody biomass (sawdust, wood flakes, and pulping fibers) with a very simple method, an impregnation with $FeCl_3$ and H_3PO_4 followed by a pyrolysis in ammonia (Fig. 10E). Pine woody materials are renewable biomasses, commonly available as waste in the wood and paper industry, and constitute low-cost raw materials. The morphological analysis showed that the specific surface areas are extremely high, with a consistent micro- and meso-porosity. The most active biomass-derived electrocatalyst comes from pine sawdust, with an alkaline ORR activity comparable to that of a commercial Pt/C, which becomes even better if Fe precursor is used as a co-doping agent during the synthesis. Both electrocatalysts, with and without Fe, result also very stable and methanol tolerant. The observed significantly better activity derives from the presence of traces of atomically dispersed Fe in the N- and P-doped carbon matrix.

Many other similar examples of PGM-free ORR electrocatalysts from biomass can be found in the very recent literature, all with very similar performance in alkaline medium both in term of onset potential and methanol tolerance: pistachio shells [220], tea leaves [221, 222], pepper powder [223], coconut shells [224], starch [225], cotton pads [226], soybean dreads starch [227], home-made biocompost [228], or vegetable market wastes [229].

7 Electrocatalysts of Animal Origin (Animal-Derived Biomass)

Animal proteins can be used as a source of aminoacid thanks to the presence of N and C in the molecules. For example, sheep horns, a common biomass waste, has been used by Amiinu et al. [230] to obtain N-, S-doped graphene by a synthesis involving the pyrolysis of the biomass, which is mostly composed of keratin. Keratin is naturally rich of N- and S- atoms from cysteine, thus the synthesis of bi-doped ORR electrocatalysts does not require the addition of external heteroatoms to obtain a doped carbon. Thus, the synthesis is facile, requiring only a cleaning step of the horns to remove any residual organic compound, mixing with graphene oxide (GO, to increase the level of carbon), a pyrolysis in argon, and a final acid leaching (Fig. 11A). The thermochemical disintegration of horn moieties during pyrolysis releases functional reactive species. These are able to react with the functional groups of GO, giving rise to a final 3D porous structure of different shapes and sizes. Moreover, the function groups containing N- and S-reactive species from the breakage of the keratin serve as self-source for doping the GO. The effect of the temperature provokes a surface wrinkling, also attributable to the different bond length of C–N, C–S, and C–C bonds in the graphene matrix.

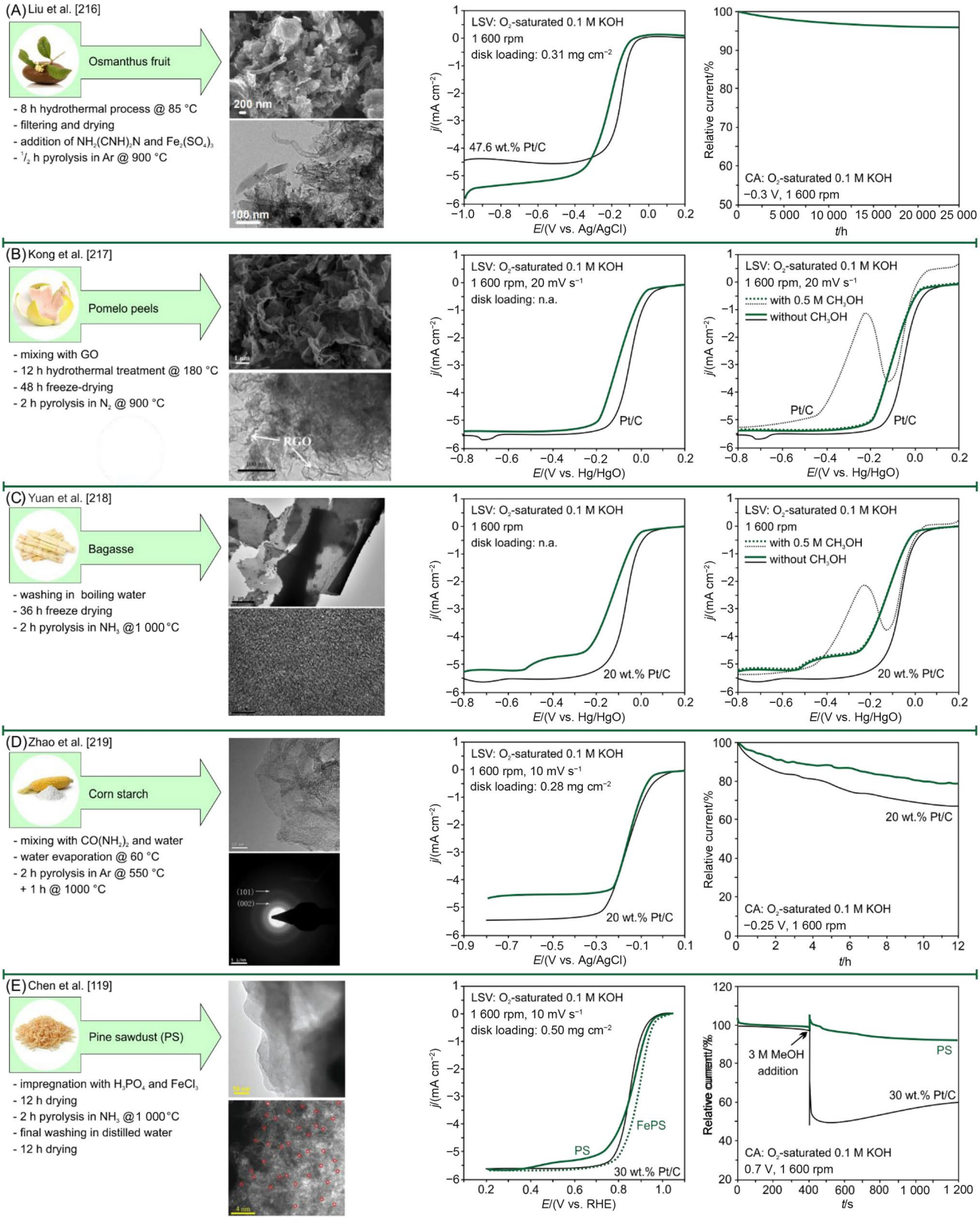
(A) Liu et al. [216]
Osmanthus fruit
- 8 h hydrothermal process @ 85 °C
- filtering and drying
- addition of $NH_2(CNH)_2N$ and $Fe_2(SO_4)_3$
- 1/2 h pyrolysis in Ar @ 900 °C
200 nm
100 nm
LSV: O_2-saturated 0.1 M KOH
1 600 rpm
disk loading: 0.31 mg cm^{-2}
47.6 wt.% Pt/C
j/(mA cm^{-2})
E/(V vs. Ag/AgCl)
CA: O_2-saturated 0.1 M KOH
−0.3 V, 1 600 rpm
Relative current/%
t/h
(B) Kong et al. [217]
Pomelo peels
- mixing with GO
- 12 h hydrothermal treatment @ 180 °C
- 48 h freeze-drying
- 2 h pyrolysis in N_2 @ 900 °C
RGO
LSV: O_2-saturated 0.1 M KOH
1 600 rpm, 20 mV s^{-1}
disk loading: n.a.
Pt/C
E/(V vs. Hg/HgO)
with 0.5 M CH_3OH
without CH_3OH
(C) Yuan et al. [218]
Bagasse
- washing in boiling water
- 36 h freeze drying
- 2 h pyrolysis in NH_3 @1 000 °C
20 wt.% Pt/C
(D) Zhao et al. [219]
Corn starch
- mixing with $CO(NH_2)_2$ and water
- water evaporation @ 60 °C
- 2 h pyrolysis in Ar @ 550 °C
+ 1 h @ 1000 °C
(101)
(002)
LSV: O_2-saturated 0.1 M KOH
1 600 rpm, 10 mV s^{-1}
disk loading: 0.28 mg cm^{-2}
20 wt.% Pt/C
CA: O_2-saturated 0.1 M KOH
−0.25 V, 1 600 rpm
(E) Chen et al. [119]
Pine sawdust (PS)
- impregnation with H_3PO_4 and $FeCl_3$
- 12 h drying
- 2 h pyrolysis in NH_3 @1 000 °C
- final washing in distilled water
- 12 h drying
4 nm
LSV: O_2-saturated 0.1 M KOH
1 600 rpm, 10 mV s^{-1}
disk loading: 0.50 mg cm^{-2}
PS
FePS
30 wt.% Pt/C
E/(V vs. RHE)
3 M MeOH addition
CA: O_2-saturated 0.1 M KOH
0.7 V, 1 600 rpm
t/s

◂**Fig. 10** **A** Osmanthus fruit-derived electrocatalysts: synthesis steps, TEM characterization, electrochemical characterization via LSV and CA. Reproduced with permission from Ref. [216]. Copyright © 2016, Royal Society of Chemistry. **B** Pomelo peel-derived electrocatalysts: synthesis steps, SEM and TEM characterization, electrochemical characterization via LSV with and without methanol. Reproduced with permission from Ref. [217]. Copyright © 2017, Elsevier. **C** Bagasse-electrocatalysts: synthesis steps, HR-TEM characterization, electrochemical characterization via LSV with and without methanol. Reproduced with permission from Ref. [218]. Copyright © 2016, Elsevier. **D** Corn starch-derived electrocatalysts: synthesis steps, TEM characterization, electrochemical characterization via LSV and CA. Reproduced with permission from Ref. [219]. Copyright © 2016, Springer Nature. **E** Pine sawdust-derived electrocatalysts: synthesis steps, TEM and HAADF-STEM characterization, electrochemical characterization via LSV and CA. Reproduced with permission from Ref. [119]. Copyright © 2018, John Wiley and Sons

In the final electrocatalyst, S is present in the form of thiophenic sulfur and oxidized sulfur, in a lower amount compared to the original amount present in the horns. In fact, the formation of volatile S–O species during pyrolysis can explain the expected lower amount of S. N instead, is mostly present as graphitic- and pyridinic-N, while oxidized- and pyrrolic-N are present in much lower amount. In terms of electrochemical ORR activity, the behavior in alkaline electrolyte is comparable to that of a commercial 20 wt.% Pt/C, while the stability and methanol tolerance are considerably better. This electrocatalyst has been tested successfully also for the oxygen evolution reaction (OER), with an activity comparable to that of IrO_2, the standard catalyst for OER (with a current density of 10 mA cm^{-2} at 0.69 V vs. SCE, compared to 0.64 V of IrO_2).

Another metal-free but N- and P-doped electrocatalyst was synthetized starting from cattle bones by Zan et al. [231], by pyrolyzing carbonized bones with phytic acid (a six-fold dihydrogen phosphate of inositol) and dicyandiamide (Fig. 11B). The final electrocatalyst has a 3D hierarchically porous structure co-doped with N and P, with ultra large specific surface area, which derives from the porous structure of the starting bones, rich of organic collagen. Collagen, in fact is an ideal, and natural, precursor, rich of N and P atoms, which acts both as a hard templating medium during pyrolysis. This gives rise to a 3D hierarchically porous structure, and as a doping agent being a source of N and P heteroatoms. The role of the two dopants is fundamental for ORR activity, as confirmed by synthesizing and testing electrocatalysts with the same process but without one or both N and P atoms. The optimal co-doping is crucial for ORR activity enhancement, as it can increase the number of active sites in terms of pyridinic-N and P–C species. This preserves the 3D hierarchically porous networks to facilitate the mass transport and guarantee the accessibility of the ORR catalytic active sites. The best synthesized co-doped N, P electrocatalyst has an ORR activity higher than that of a Pt/C counterpart in alkaline environment, with the transferred electron number very close to 4. Moreover, also the stability of the co-doped electrocatalyst is better than that of Pt/C. The developed synthesis is easy to try with other types of biomass-derived materials containing collagen in order to obtain new doped carbon materials.

Guo et al. [232] synthesized ORR electrocatalysts starting from fresh scales of *Crassium auratus* fish, which are rich in proteins. The simple synthesis method, which accounts for carbonization and pyrolysis (Fig. 11C), converted the fish bio-waste into a highly defective 3D porous carbon nano-network. The most active electrocatalysts, pyrolyzed at 900 °C, are rich in N, especially graphitic- and pyrrolic-N, thanks to the addition of $ZnCl_2$ before the pyrolysis step. In fact, $ZnCl_2$ is known to fasten the carbonization process, reducing the loss of nitrogen during the pyrolysis step, and increasing the content of micro- and meso-pores. Moreover, the laminar structure of the fish scales is partially preserved during the pyrolysis, favoring the formation of a 3D network structure, with a highly rough surface. The ORR electrocatalytic activity of the best sample is almost overlapping that of a commercial 20 wt% Pt/C in acid electrolyte, but producing more H_2O_2 at high current density, due to a mixed 2- and 4-electron reaction pathway. While in alkaline environment, the activity of the fish-derived electrocatalyst is much higher compared to that of Pt/C, with more positive onset and half-wave potentials. The stability of the produced electrocatalyst was assessed with a series of repeated cyclic voltammetry, which showed a very limited decay of the performance, demonstrating thus the good stability of this catalyst, much better that the Pt/C counterpart used as a comparison term.

Zheng et al. [233] recycled waste shrimp shells, a very common waste biomass in Asian markets. Shrimp shells are an interesting biomass, rich in chitin and chitosan, which can be helpful in preparing a carbon-based matrix naturally co-doped in N and P heteroatoms. Through a simple and low-cost procedure, these authors first removed calcium carbonate by soaking shells with diluted hydrochloric solution and, contemporarily, forming a porous structure. Then, via a hydrothermal treatment with phosphoric acid followed by a pyrolysis, they obtained a final electrocatalyst highly defective and with large specific surface area (Fig. 11D). In fact, the residual proteins and chitin present in the shells, rich in N, favor the formation of C–N bonds during the pyrolysis. Moreover, the use of phosphoric acid favors the co-doping of P, bonded to either O and C atoms, and increases the defects, giving rise to a very high electrochemical activity towards ORR. The morphological structure of the final electrocatalyst maintains the carbon skeleton of chitin, forming spherical carbon networks. The ORR activity in alkaline environment is only slightly worse than that of a commercial Pt/C, but with a higher stability and high tolerance to methanol.

Silkworm cocoons have been employed by Shi et al. [234] to synthesize $Ca@NP_6C_4$ electrocatalysts with interesting

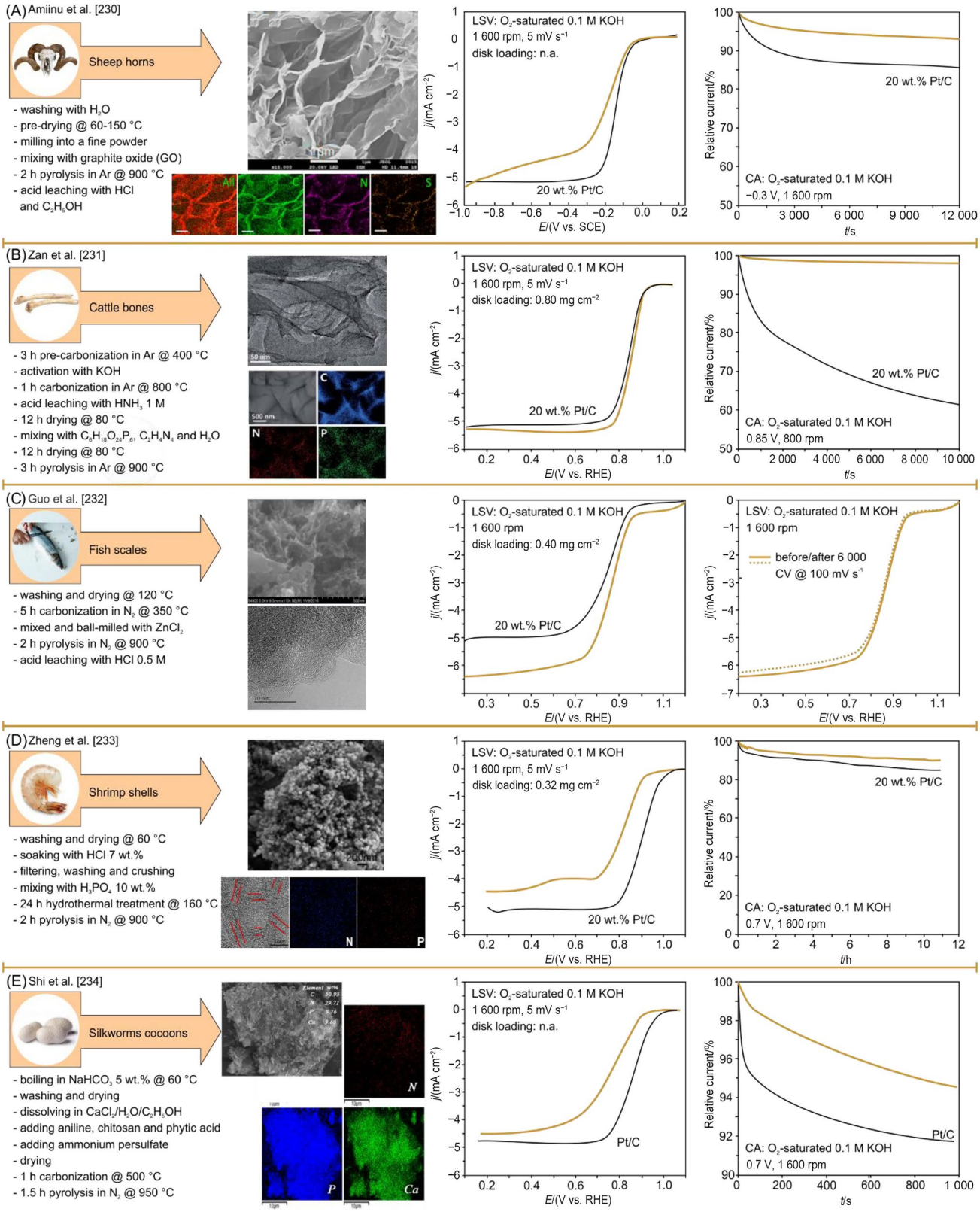

activity towards ORR in alkaline medium. Briefly, silkworm cocoons were dissolved in $NaHCO_3$ to obtain a silk-rich protein solution. Then, aniline, chitosan and phytic acid were added, followed by a further addition of ammonium persulfate. Finally, a carbonization and a pyrolysis at 500 and 950 °C followed. The optimization of the synthesis allowed

◂**Fig. 11** **A** Sheep horn-derived electrocatalysts: synthesis steps, TEM and EDX characterization, electrochemical characterization via LSV and CA. Reproduced with permission from Ref. [230]. Copyright © 2016, American Chemical Society. **B** Cattle bone-derived electrocatalyst: synthesis steps, TEM and EDX characterization, electrochemical characterization via LSV and CA. Reproduced with permission from Ref. [231]. Copyright © 2017, Royal Society of Chemistry. **C** Fish scale-derived electrocatalyst: synthesis steps, SEM and TEM, electrochemical characterization via LSV and CA. Reproduced with permission from Ref. [232]. Copyright © 2017, Elsevier. **D** Shrimp shells-derived electrocatalysts: synthesis steps, SEM elemental, electrochemical characterization via LSV and CA. Reproduced with permission from Ref. [233]. Copyright © 2020, Elsevier. **E** Silkworm cocoon-derived electrocatalysts: synthesis steps, SEM and TEM, electrochemical characterization via LSV and CA. Reproduced with permission from Ref. [234]. Copyright © 2021, Elsevier

obtaining a very well performing material, $Ca@NP_6C_4$ (Fig. 11E), with a performance similar to Pt/C in alkaline medium, and better methanol tolerance. The electrocatalyst has most of the nitrogen as pyridinic and graphitic ones, with P–C and P–O bonds. In the literature, the co-doping of N and P is recognized to weaken the O–O bonding during the ORR, favoring thus the electrocatalytic activity [235].

Liu et al. [236] synthesized nitrogen-doped carbon nanosheets by mixing chitosan (derived from seashells waste) with excess of urea in a water/acetic acid solution and freeze-drying, followed by a slow pyrolysis in Ar at 1 000 °C (Fig. 12A). The best obtained electrocatalyst, optimized with a chitosan/urea ratio of 1.12, had a very high specific surface area, and a high graphitic/pyridinic nitrogen ratio. The morphology presented interconnected ultrathin graphene nanosheets architecture, with a thickness below 1 nm, close to that of a single monolayer of reduced graphene oxide, which suggests a potential use of this material also as an electronic capacitor or for hydrogen storage. It displayed a better activity compared to the commercial 20 wt.% Pt/C, a longer stability and also a better methanol tolerance in alkaline environment.

Chicken manure is rather abundant and has been used as a starting material for preparing metal-free bio-carbons electrocatalysts by Alonso-Lemus et al. [237]. This waste was subjected to several treatments, such as pyrolysis, chemical activation using KOH and H_3PO_4 and solvothermal treatment with hydrazine for further doping. This procedure was performed to modify its properties to obtain N and P co-doped bio-carbons. The resulting materials tested for ORR in alkaline media showed an activity lower than that of a commercial Pt/C. The most active electrocatalyst, obtained only by pyrolysis, without solvothermal treatment and phosphoric acid treatment (sample B_K in Fig. 12B) showed an activity that can be the result of a mixed 4 and $2e^-$ transfer pathway. The solvothermal treatment (sample $B_{K\text{-}ST}$ in Fig. 12B) modified the concentration of N in the samples, by lowering the amount of pyridinic-N and quaternary-N, with a consequent negative effect on ORR activity. Indeed, even if in the literature the doping with P has been reported to be favorable for ORR activity, this was not the case. In fact, the samples prepared with H_3PO_4 worsen the ORR activity compared to those prepared by KOH activation, mostly because of the presence of inactive compounds and low specific surface area. The morphological analysis of the prepared samples revealed that the morphology of B_K sample presents numerous agglomerates or "clouds" of carbon. The latter may be generated by the interaction of K ions with carbon atoms of the bio-carbon structure, thanks to the KOH activation. While the activation with H_3PO_4 generates a rougher morphology, apparently with a larger amount of macropores. Interestingly, the catalytic activity of the best B_K material increased after accelerated degradation tests (3 000 cycles of potential cycling). This could be the result of an increase in surface area due to degradation.

Lee et al. [238] have reported the preparation of electrocatalytic materials using pig's blood as a precursor. Blood is interesting for ORR electrocatalysts, since it naturally contains porphyrin-type Fe-macrocycles. These are well-known as an effective molecule able to form FeN_X active sites for ORR. The preparation procedure forecasts a reaction between coagulated blood and toluene to remove phospholipids from blood. Followed by a hydrothermal step and a pyrolysis in nitrogen. The resulting electrocatalyst is a porous graphitic carbon decorated with Fe_3C/Fe_3O_4 nanoparticles (Fig. 12C). The pre-treatment with toluene plays a key role in generating nanoparticles on porous carbon. Indeed, this also eliminates impurities that damage the active sites of molecular nitrogen carbon bonds during high-temperature treatment. In fact, an ORR electrocatalyst prepared according to the same procedure, but without using toluene showed an insignificant ORR activity. While the toluene-treated electrocatalyst showed an activity on alkaline electrolyte better than a commercial 20 wt.% Pt/C electrocatalyst. Also the temperature for hydrothermal treatment and pyrolysis affects ORR electrocatalytic activity: the higher, the better, since it might produce Fe–Fe bonding, in addition to Fe–C, resulting in a higher ORR activity. In terms of stability, the blood-derived electrocatalyst showed a better activity that Pt/C. The best electrocatalyst obtained delivered a current density of 1.57 mA cm^{-2} at 0.9 V after 10 000 potential cycles at 0.9 V in comparison with Pt/C that exhibited 1.26 mA cm^{-2} at 0.9 V. Using animal blood in general opens a new family of bio-mass catalytic materials that are easily available from slaughter houses all over the world.

Chaudhari et al. [239] obtained a valuable electrocatalyst from human hair, effectively doping the material with N and S after carbonization at 900 °C (Fig. 12D). Interestingly, the α-keratin available in the protein network demonstrated to be an interesting precursor of heteroatoms, and carbon of course, avoiding thus an external doping of S and

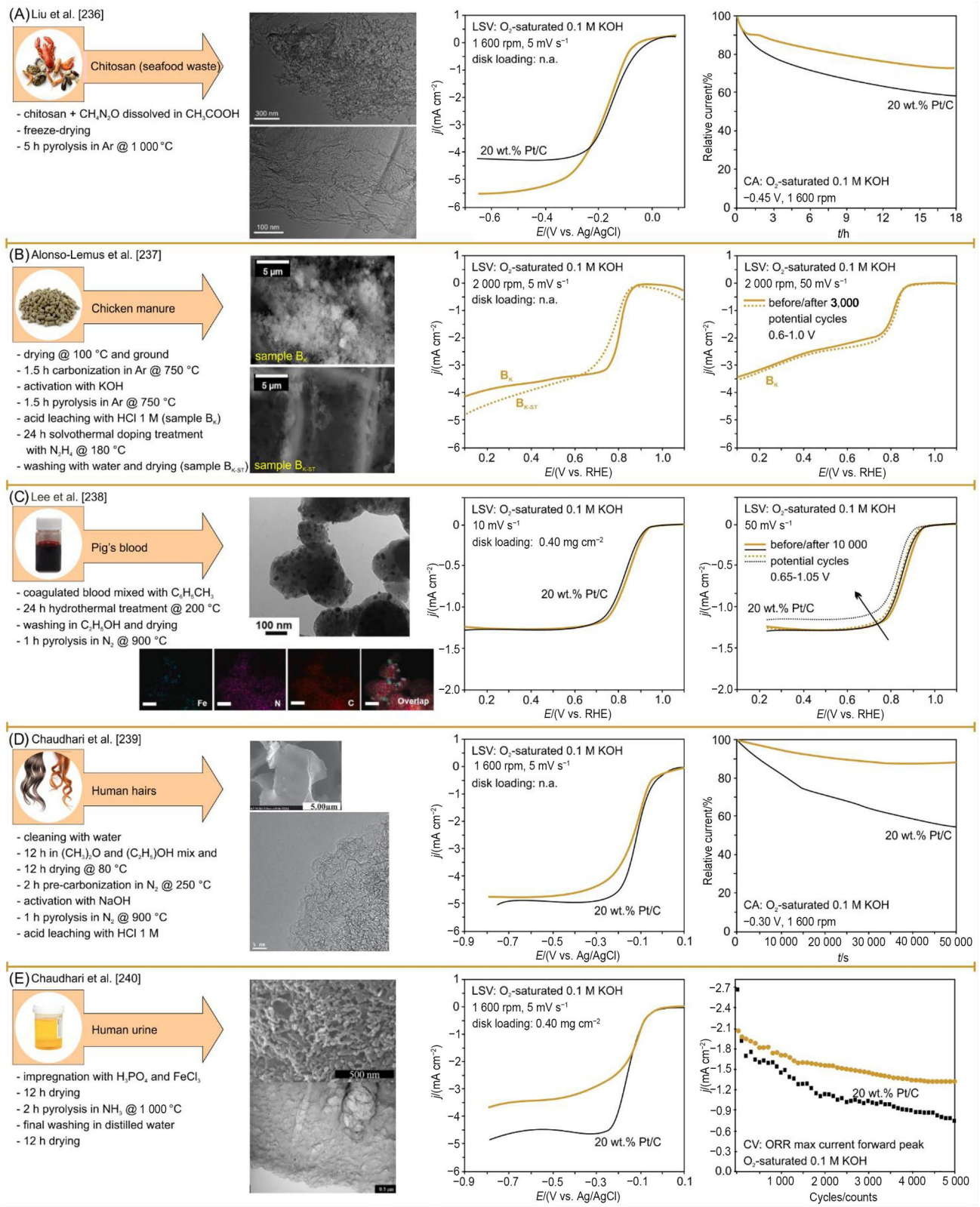

N. The synthesis strategy involves moderate activation and further graphitization to enhance the electrical conductivity. The high-temperature annealing favors a morphology of the electrocatalyst with a wrinkled structure, rich of open edges and thin stacks of disordered carbon layers. The ideal temperature for annealing is 900 °C, since at higher

◂**Fig. 12** **A** Chitosan-derived electrocatalysts: synthesis steps, TEM characterization, electrochemical characterization via LSV and CA. Reproduced with permission from Ref. [236]. Copyright © 2014, American Chemical Society. **B** Chicken manure-derived electrocatalysts: synthesis steps, SEM characterization, electrochemical characterization via LSV before and after potential cycling accelerated degradation test. Reproduced with permission from Ref. [237]. Copyright © 2019, Royal Society of Chemistry. **C** Pig blood-derived electrocatalysts: synthesis steps, TEM and EDX characterization, electrochemical characterization via LSV before and after potential cycling accelerated degradation test. Reproduced with permission from Ref. [238]. Copyright © 2021, Elsevier. **D** Human hair-derived electrocatalysts: synthesis steps, SEM and TEM characterization, electrochemical characterization via LSV and CA. Reproduced with permission from Ref. [239]. Copyright © 2014, John Wiley and Sons. **E** Human urine-derived electrocatalysts: synthesis steps, SEM and TEM characterization, electrochemical characterization via LSV and ORR forward peak maximum current in CV during the repeated potential cycling up to 5 000. Comparison of CV of 20 wt.% Pt/C. Reproduced with permission from Ref. [240]. Copyright © 2014, The author(s). Published by Springer Nature

temperature the percentage of S and P decreases. Moreover, at this temperature the percentage of pyridinic-N is at the highest value. On the electrochemical point of view, the best sample revealed an activity very similar to that of a commercial 20 wt.% Pt/C in alkaline environment, but with much higher stability, and also methanol tolerance. The interesting results obtained demonstrated that human hairs, considering their abundance and ease availability, represent an almost infinite bio-resource able to basically reduce to zero the cost of the carbon source.

To highlight the extent of the kind of biomass that is possible to use, the same group reported the synthesis of highly porous carbon by carbonization of human urine at high temperatures (700–1 100 °C), following by acid washing in a template-free route (Fig. 12E) [240]. Urine is a complex aqueous solution made by various complexes such as urea, tyrosine O-sulfate, and different inorganic salts and minor traces than can be natural sources of heteroatoms such as N and S. The presence of heteroatoms is beneficial because of the possibility to include these atoms in the porous carbon structure in a single step without the need of further activation. Moreover, the removal of the inherently present salt particles is observed to create high porosity in the form of micro-, meso- and macro-pores on the surface and inside the structure. The sample carbonized at 800 °C had a maximum specific surface area of 1 436.8 $m^2\ g^{-1}$, with high nitrogen content (8.5%). The yield was quite low (0.03–0.04 wt.%), meaning only 300–400 mg of porous carbon is obtained from 1 L of human urine. The best electrocatalyst was obtained at 1 000 °C, but with lower specific surface area and lesser N content. Specifically, the electrocatalyst has a higher amount of quaternary-C and pyridinic-N, which highly contributes to the electrocatalytic activity, and small amounts of pyrrolic-N. The activity loss was only 35% after 5 000 cycles, making this electrocatalyst durable in comparison to other biomass-derived material.

8 Biomass-Derived Electrocatalysts Tested in PEMFC/AEMFC

Compared to the synthesis of biomass-derived electrocatalysts, and their characterization in RDE/RRDE configuration, much less data are available in the literature for their applications in low temperature fuels cells, either in acid (PEMFC) or alkaline (AEMFC) medium. Here we are going to examine some examples. All the data referring to tests in fuel cells are listed in Table 3, while the physico-chemical characteristics of the electrocatalysts are listed in Table 2.

Wang et al. [241] started from a freeze-dried black fungus powder from northern China, treated with melamine and zinc chloride under nitrogen (Fig. 13A). No other precursors reagents were employed. The mixed reagents were subjected to a pyrolysis under nitrogen at 950 °C. The resulting electrocatalyst exhibited good ORR activity in RRDE measurements using both alkaline and acid media, but lower compared to a commercial 20 wt.% Pt/C electrocatalyst. This electrocatalyst was tested in a single 1 cm^2 active area H_2/O_2 PEMFC, using Nafion® NRE211 as a membrane. The PEMFC performance reached a peak power density of 255 mW cm^{-2}, at 710 mA cm^{-2}, using an optimized electrocatalyst pyrolyzed at 950 °C for 2 h at the cathode. Even if the cell performance cannot be considered as high as expected, especially if compared with other PGM-free electrocatalysts available in the literature, the durability, tested under constant current mode at 100 mA cm^{-2} for 32 h, was excellent. The cell voltage decreased of only 15%. The good electrocatalytic activity was attributed to the presence of Fe, N, and S ions in the raw material, enhanced by the additional N doping in the pyrolysis process.

Peat-derived carbons were synthesized in a study of Jäger et al. [242], using various carbonization protocols, resulting in a series of carbons with various elemental composition, surface morphologies and porosity. The carbons were then Co and N co-doped with $Co(NO_3)_2$ and 2,2'-bipyridine. The ORR activity tested at RDE level in acidic environment showed a lower activity compared to a commercial 20 wt.% Pt/C catalyst. The activation of pyrolized peat with $ZnCl_2$ provided the best active ORR electrocatalyst (Fig. 13B) that was tested in a 5 cm^2 H_2/O_2 PEMFC, reaching a maximum power density peak of 210 mW cm^{-2} at 80 °C, while the other electrocatalyst reached only 122 mW cm^{-2}. No durability values were reported. Comparing the two electrocatalysts, the better electrocatalytic activity of the sample Co–N/C-2($ZnCl_2$) was ascribed to the higher N content and higher surface oxides species. The main value of this study is the possible application of decomposed peat, which is no

Table 3 PEMFC (Fig. 16) and AEMFC (Fig. 17) specifications: MEA characteristics, anode/cathode loading, and testing conditions (b.p.: back pressure; a.p.: atmospheric pressure; a.t.: ambient temperature)

Electrocatalysts	Membrane		MEA loading		Testing conditions				Peak power density	Figure [Ref.]
	Type	Area	Cathode	Anode	H_2	O_2	T_{cell}	b.p.		
	Commercial name	cm^2	$mg_{PGM\text{-}free}\ cm^{-2}$	$mg_{PGM}\ cm^{-2}$	slpm/ R.H.	slpm/ R.H.	°C	kPa	$mW\ cm^{-2}$	
PEMFC										
FeNC-BFungus	Nafion® NRE211	1	4	0.2 (20 wt.% Pt/C)	0.1/100	0.1/100	80	200	255 @ 700 mA cm^{-2}	13A/16Ac [241]
CoNC-peat	Nafion® HP	5	4	1 (60 wt.% Pt/C)	0.1/100	0.1/100	80	100	255 @ 750 mA cm^{-2}	13B/16Ab [242]
FeNC-hemo	Nafion® N112	5	5	0.5 (Pt/C)	0.2/100	0.2/100	80	a.p.	125 @ 390 mA cm^{-2}	13C/16Aa [243]
FeNC-ZIF	Nafion® NRE211	4.84	4	0.5 (Pt/C)	0.6/100	0.6/100	80	100	440 @ 1 000 mA cm^{-2}	16Ad [254]
FeNC-C29	IRD fuel cells	5	2.5	0.2 (50 wt.% Pt/C)	0.5/100	1./100	80	150	645 @ 1 850 mA cm^{-2}	16Ae [253]
FeNC-C30	IRD fuel cells	5	2.5	0.2 (50 wt.% Pt/C)	0.5/100	1.0/100	80	150	837 @ 1 850 mA cm^{-2}	16Af [253]
Pt/C-PEMFC	IRD fuel cells	5	0.1 $mg_{Pt}\ cm^{-2}$	0.2 (50 wt.% Pt/C)	0.5/100	1.0/100	80	150	1 000 @ 1 550 mA cm^{-2}	16Ag [253]
AEMFC										
NC-bamboo	Fumapem® FAA-3–50	5	2 (+0.2 $mg_{Pt}\ cm^{-2}$)	0.5 (60 wt.% Pt/C)	0.8/80	1.0/90	60		217 @ 570 mA cm^{-2}	14A/16Bb [189]
FeNC-sucrose	AHA-neosepta	4	4	2.5 (Pt/C)	1.5/100	1.0/100	a.t.	a.p.	118 @ 240 mA cm^{-2}	14B [244]
FeCoNC-rapeseed	Aemion AF2-HLE-10-X	5	2	0.8 (Pt/Ru/C 50:25:25)	0.8/50	1.0/90	60	200	131 @ 250 mA cm^{-2}	14C/16Ba [245]
FeCoNC-resorcinol	HTM-PMBI	5	2	0.6 (Pt/Ru/C 50:25:25)	0.1/100	0.1/100	60	200	415 @ 820 mA cm^{-2}	16Bc [258]
$Fe_{0.5}NC\text{-}NH_3$	ETFE		1.5	0.9 (40 wt.% PtRu/C 40:20:60)	1.0	1.0	60	a.p.	1 040 @ 2 260 mA cm^{-2}	16Bd [255]
CoFeNC	HDPE	5	0.01	0.7 (40 wt.% Pt/Ru/C 40:20:60)	1.0	1.0	60	200	1 120 @ 2 000 mA cm^{-2}	16Be [256]
FeNC-PFM11904	HDPE	5	1	0.6 (40 wt.% Pt/Ru/C 40:20:60)	1.0/100	1.0/100	60	200	1 250 @ 2 600 mA cm^{-2}	16Bf [257]
Pt/C-AEMFC	ETFE		0.45 $mg_{Pt}\ cm^{-2}$ (40 wt.% Pt/C)	0.6 (40 wt.% Pt/Ru/C 40:20:60)	1.0	1.0	60	a.p.	1 530 @ 2 870 mA cm^{-2}	16Bg [255]

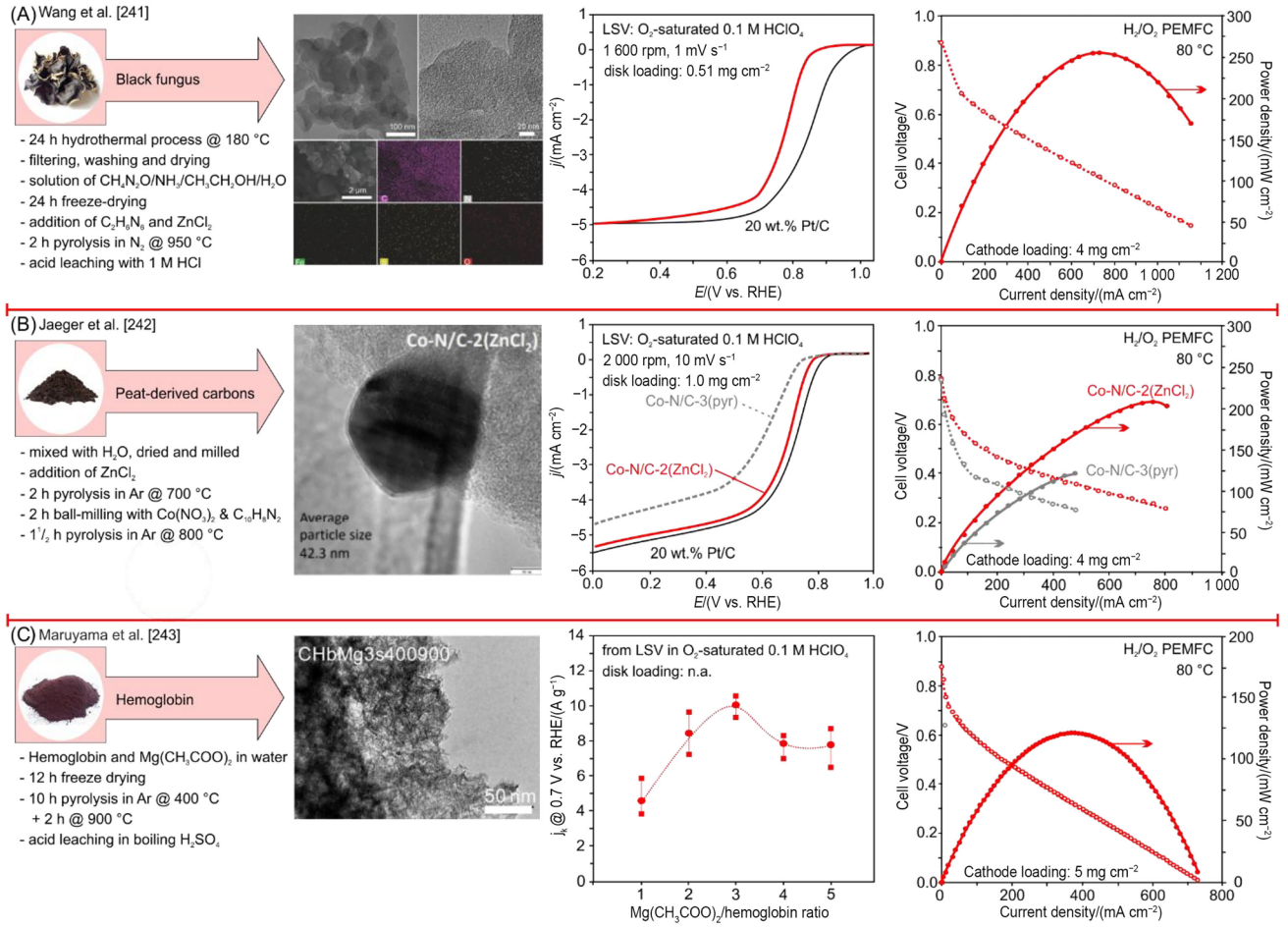

Fig. 13 Biomass-derived electrocatalysts tested in PEMFC. **A** Black fungus-derived electrocatalysts: TEM characterization, LSV in acid electrolyte, PEMFC performance. Reproduced with permission from Ref. [241]. Copyright © 2019, Springer Nature. **B** Peat-derived electrocatalysts: TEM characterization, LSV in acid electrolyte, PEMFC performance. Reproduced with permission from Ref. [242]. Copyright © 2021, The Author(s). Published by MDPI. **C** Hemoglobin-derived electrocatalysts: TEM characterization, j_k optimization via LSV, PEMFC performance. Reproduced with permission from Ref. [243]. Copyright © 2011, American Chemical Society

longer used as a fuel for heating purposes, or in agriculture for as a fertilizer.

Hemoglobin from bovine blood, which is an abundant, natural and inexpensive source, is an interesting starting material for preparing electrocatalysts. This is because it contains the proper components to obtain Fe–N–C electrocatalysts without adding other Fe- or N-based precursors. [243] prepared aqueous solutions containing hemoglobin and $Mg(CH_3COO)_2$ in various ratios that were frozen and placed in a vacuum chamber overnight. The mixtures were then pyrolyzed in flowing Ar at 400 °C for 10 h and then finely ground. A second pyrolysis followed in flowing Ar at 900 °C for 2 h. The materials, finely ground again, were washed first in boiling H_2SO_4 then in water, and finally dried to remove any soluble Mg and Fe species (Fig. 13C). The high temperature pyrolysis allowed obtaining a series of amorphous carbonaceous materials containing MgO, which was leached out by the acid treatment, leading to the formation of a porous structure. The optimization of the hemoglobin/$Mg(CH_3COO)_2$ ratio allowed obtaining the highest kinetic current at 0.7 V versus RHE, tested using a RDE, with a value equal to 3. This electrocatalyst has a high specific surface area and pore volume. Extended X-ray absorption fine structure (EXAFS) investigations highlighted the presence of Fe-N_4 moieties in the electrocatalyst, derived from the protoheme of the hemoglobin. The performance of this electrocatalyst in a 5 cm^2 H_2/O_2 PEMFC was equal to 125 mW cm^{-2}, at 390 mA cm^{-2}, with a 40% decrease of the performance after 200 h of continuous testing at 0.5 V and 80 °C.

Bamboo is a widely spread, fast growing plant already studied for pollutant absorption. It is known for a porous and conductive structure of its charcoal. Kim and co-workers [189] obtained a hierarchically porous S, N-co-doped carbon

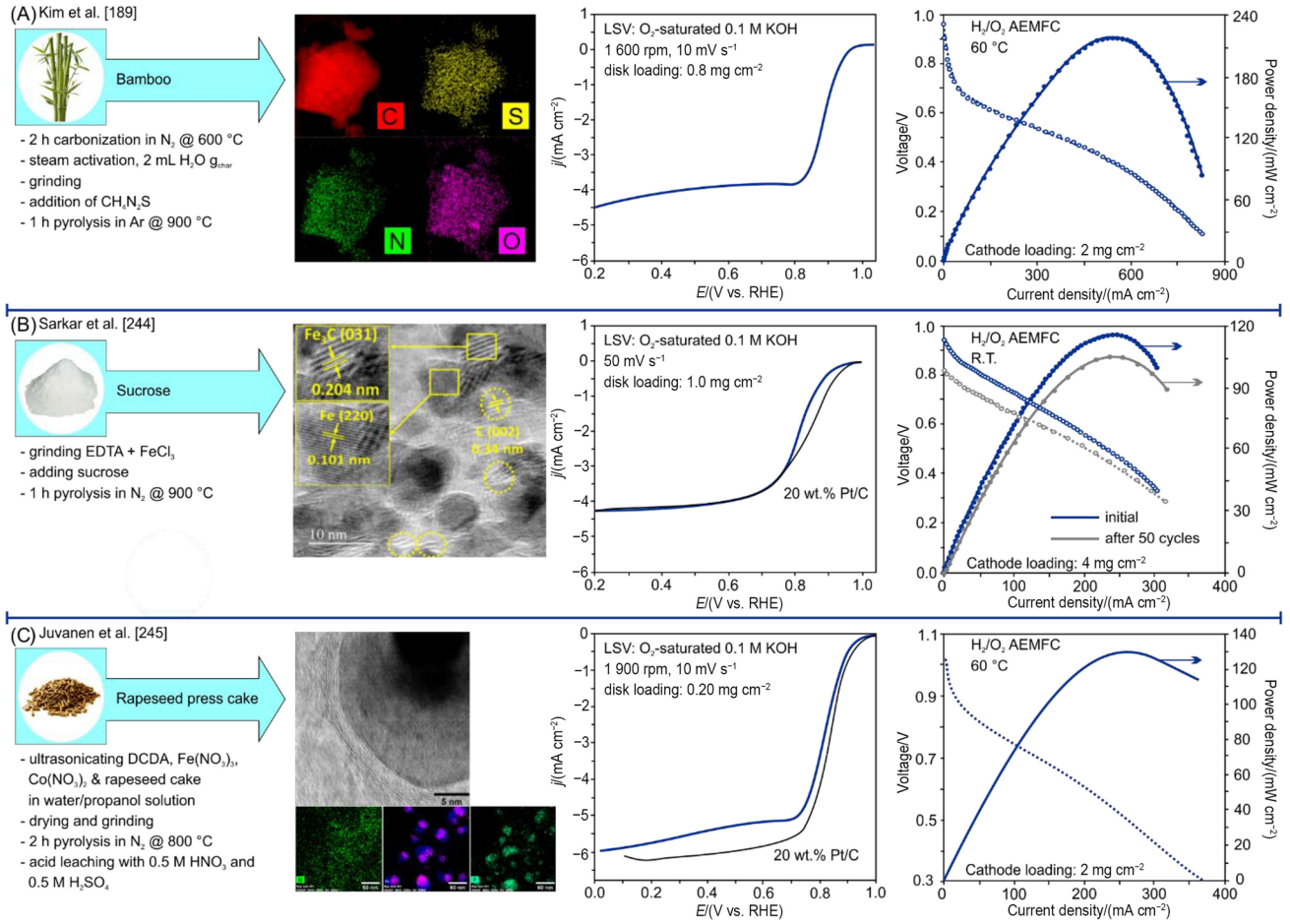

Fig. 14 Biomass-derived electrocatalysts tested in AEMFC. **A** Bamboo-derived electrocatalysts: TEM/EDS characterization, LSV in alkaline electrolyte, AEMFC performance. Reproduced with permission from Ref. [189]. Copyright © 2019, American Chemical Society. **B** Sucrose-derived electrocatalysts: TEM characterization, LSV in alkaline electrolyte, AEMFC performance. Reproduced with permission from Ref. [244]. Copyright © 2020, Springer Nature. **C** Rapeseed-derived electrocatalysts: TEM-EDS characterization, LSV in alkaline electrolyte, AEMFC performance. Reproduced with permission from Ref. [245]. Copyright © 2022, Elsevier

electrocatalyst derived from carbonized bamboo, activated with a flow of steam at 600 °C, and further doping with thiourea. A final pyrolysis was then conducted (Fig. 14A). The optimized synthesis, with a char/thiourea equal to 1:2, and the pyrolysis conducted at 900 °C, allowed to produce an electrocatalyst with an irregular shape, rich in micro- and meso-pores, and high content of S and N heteroatoms located on the basal structure of the carbon. Such an electrocatalyst was tested in a 5 cm^2 H_2/O_2 AEMFC, reaching a maximum power density of 217 mW cm^{-2} at 570 mA cm^{-2}. At equal testing conditions, a MEA prepared in the same conditions but with only commercial Pt/C was only slightly better, reaching 268 mW cm^{-2} at 590 mA cm^{-2}. The explanation of the relatively good activity of the bamboo-derived electrocatalyst could be attributed to its large pores, which enhance mass transport in the catalyst layer. Moreover, the electrocatalyst was tested also in a primary ZAB, with a performance of 156 mW cm^{-2} at 830 mA cm^{-2}, respectively.

Sarkar et al. [244] used sucrose of biological origin to synthesize a Fe–N–C electrocatalyst in a one-step, solvent-free scalable synthesis. Sucrose was mechanically grinded with a solid-state coordination complex obtained by mixing $FeCl_3$ and ethylene-diamine-tetra acetic acid (EDTA). The obtained powder was the pyrolyzed at 900 °C. The optimized electrocatalyst was obtained with a 10:1 mass ratio between sucrose and $FeCl_3$ (Fig. 14B). The role of EDTA, an hexadentate ligand, lies in its complexation action, favoring the Fe–N linking in the form FeN_4 coordination, to increase the formation of active sites in the final electrocatalyst. Moreover, during the pyrolysis step, EDTA decomposes releasing NH_3 and CN_x^+ radical species, increasing thus the penetration of N in the carbon lattice. Sucrose, in addition to acting as a carbon source, pyrolyzes as graphitic carbon thanks to the presence of Fe^{3+} ions, which is reduced to metallic Fe. Physical–chemical analyses revealed the presence of Fe_3C species, embedded Fe nanoparticles with a

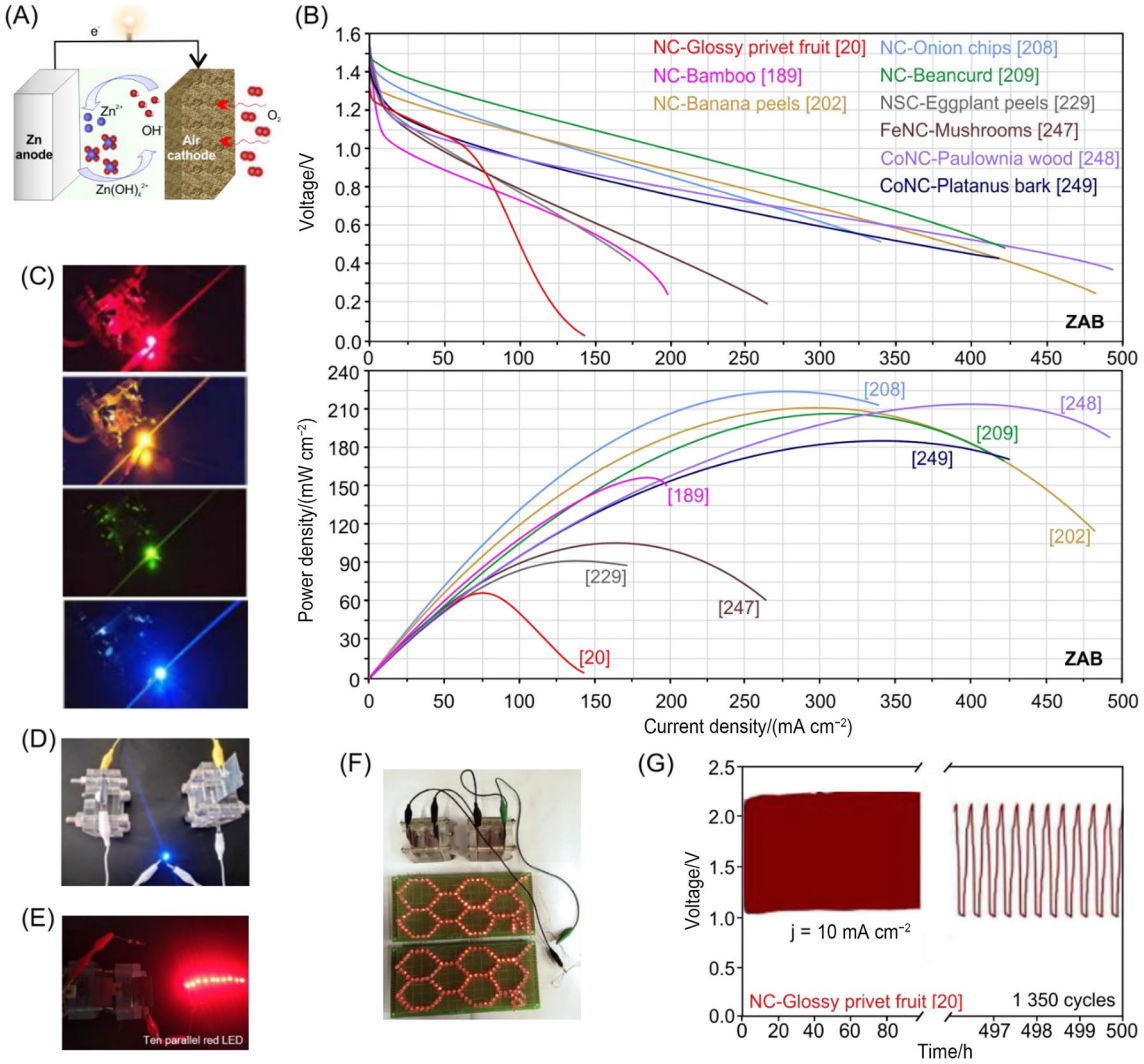

Fig. 15 **A** Scheme of a primary ZAB. **B** Polarization curves and power density curves of various ZABs tested with biomass-derived electrocatalysts listed in Table 4. Reproduced with permission from Ref. [20]. Copyright © 2020, American Chemical Society. Reproduced with permission from Ref. [189]. Copyright © 2019, American Chemical Society. Reproduced with permission from Ref. [202]. Copyright © 2017, Elsevier. Reproduced with permission from Ref. [208]. Copyright © 2020, Springer Nature. Reproduced with permission from Ref. [209]. Copyright © 2020, The Electrochemical Society. Published by IOP Publishing Ltd. Reproduced with permission from Ref. [229]. Copyright © 2022, Elsevier. Reproduced with permission from Ref. [247]. Copyright © 2022, Elsevier. Reproduced with permission from Ref. [248]. Copyright © 2023, Elsevier. Reproduced with permission from Ref. [249]. Copyright © 2022, Elsevier. Images of ZAB providing energy to led lamps tested with **C** glossy privet fruits (reproduced with permission from Ref. [20], copyright © 2020, American Chemical Society), **D** onion chips (reproduced with permission from Ref. [208], copyright © 2020, Springer Nature), **E** banana peels (reproduced with permission from Ref. [202], copyright © 2017, Elsevier), **F** eggplant peels (reproduced with permission from Ref. [229], copyright © 2022, Elsevier). **G** Charge–discharge voltage gap of a ZAB with glossy privet fruits derived electrocatalyst. Reproduced with permission from Ref. [20]. Copyright © 2020, American Chemical Society

mean size of 5 nm, and a high content of both pyridinic-N and graphitic-N. The electrochemical characterization in RDE with an alkaline electrolyte showed a performance almost comparable to that of a 20 wt.% commercial Pt/C. The optimized electrocatalyst was tested in a 4 cm^2 H_2/O_2 AEMFC at room temperature, producing 118 mW cm^{-2} at 240 mA cm^{-2}. The AEMFC was then cycled held at 2 voltages (1.4 V for 30 s and 0.6 V for 150 s) for 50 times, to evaluate the performance after the potential cycling. The final polarization was only 11% lower in terms of power peak, compared to the initial performance, showing thus a limited decay. The good performance was ascribed to the synergistic effect between FeN_4 species and the N–C support. A comparison MEA prepared and tested in the same conditions, but with Pt/C at the cathode reached only 82 mW

Table 4 ZAB specifications (Fig. 15): cathode loading, anode characteristics, electrolyte, and testing conditions

Electrocatalyst	Cathode loading		Anode thickness, Zn plate/μm	Electrolyte	T_{cell}/°C	Peak power density/(mW cm^{-2})	Ref.
	$mg_{PGM\text{-}free}$ cm^{-2}	Type					
NC-glossy privet	1.0	Carbon paper (2 cm × 2 cm)	n.a.	6 M KOH + 0.2 M $Zn(CH_3COO)_2$	25	68	[20]
NSC-obergine peel	1.0	Carbon paper	n.a.	6 M KOH + 0.2 M $Zn(CH_3COO)_2$	25	90	[229]
FeNC-mushrooms	n.a.	(1 cm × 1 cm)	500	6 M KOH	25	94	[247]
NC-bamboo	4.0	Carbon cloth (1 cm × 1 cm)	250	6 M KOH	25	156	[189]
CoNC-platanus bark	1.0	Carbon paper	n.a.	6 M KOH + 0.2 M $Zn(CH_3COO)_2$	25	186	[249]
NC-beancurd	4.0	Carbon paper (2 cm × 2 cm)	500	6 M KOH	25	207.5	[209]
NC-banana peels	0.8	Carbon paper	n.a.	6 M KOH	25	208	[202]
CoNC-paulownia wood	2.0	Carbon paper (1 cm × 1 cm)	n.a.	6 M KOH + 0.2 M $Zn(CH_3COO)_2$	25	215	[248]
NSC-onion chips	1.0	Carbon paper (2 cm × 2 cm)	n.a.	6 M KOH	25	221	[208]

cm^{-2} at 160 mA cm^{-2}, and after potential cycling lost the 56% of the peak power density.

Table 5 2020 technical targets for a H_2/O_2 PEMFC (transportation applications) suggested by DOE [96, 252] for commercializing PEMFC-fueled light-duty vehicles, considering a target price of \$30 kW_{net}^{-1} (for an estimated mass production of 500 000 units per year, 80 kW_{net} systems)

Characteristic	Target
PGM-free activity*	> 44 mA cm^{-2} @ 900 $mV_{IR\text{-}free}$
Loss in performance at 0.8 A cm^{-2}	< 30 mV
PGM total loading (anode side)	< 0.1 mg_{PGM} cm^{-2}
Mass activity	> 440 mA mg_{PGM}^{-1} @ 900 $mV_{IR\text{-}free}$
Loss in initial catalytic activity	< 40% mass activity loss

* Based on a stack with PGM total content on both electrodes of 125 g kW^{-1} at 150 kPa,abs

Juvanen et al. [245] used hot-pressed rapeseed cakes as inexpensive biomass to synthesized transition metal-containing (Fe, Co, and FeCo) nitrogen-doped electrocatalysts (Fig. 14C). Dicyanamide and metal nitrates were used as nitrogen and metal precursors, dissolved in propanol. After ultrasonication and solvent evaporation, the grinded powder was pyrolyzed at 800 °C in N_2, and finally acid leached. The electrocatalysts had an electrocatalytic ORR activity in RDE in alkaline electrolyte, almost comparable to that of a commercial 20 wt.% Pt/C, with a better performance for the bimetallic FeCo–N–C. Moreover, all the metal-N–C electrocatalysts displayed a good tolerance to methanol and high stability in short-time tests. A physicochemical characterization showed the presence of atomically dispersed N-coordinated metal (M–N_x) centers, which are known to provide a high ORR electrocatalytic activity, with a high content of pyridinic-N (almost 48%). P was also detected. The bimetallic FeCo–N–C, tested in a 5 cm^2 H_2/O_2 AEMFC at 60 °C, produced 131 mW cm^{-2} at 250 mA cm^{-2}. No durability data in AEMFC are available.

9 Biomass-Derived Electrocatalysts Tested in Zinc-Air Batteries (ZABs)

Some of the electrocatalysts previously described have been tested also in zinc-air batteries (ZABs). ZABs have drawn increasing attention as post-lithium ion batteries thanks to their high theoretical energy density (1.084 Wh g^{-1}), reliable safety, eco-friendly characteristics and low cost. However, ZAB still suffers from low-power density because of the sluggish ORR kinetics and fast degradation due to the presence of CO_2 in the atmosphere [177, 246]. Figure 15 shows the typical polarization curves of ZAB obtained with N-, Fe–N- or Co–N-doped carbon electrocatalysts derived from glossy privet [20], bamboo [189], banana peels [202], onion chips [208], beancurd [209], eggplant peels [229], mushrooms [247], paulownia wood chips [248], and platanus bark [249].

Table 4 lists the characteristics and testing conditions of these ZABs. With the exception of the very low performance

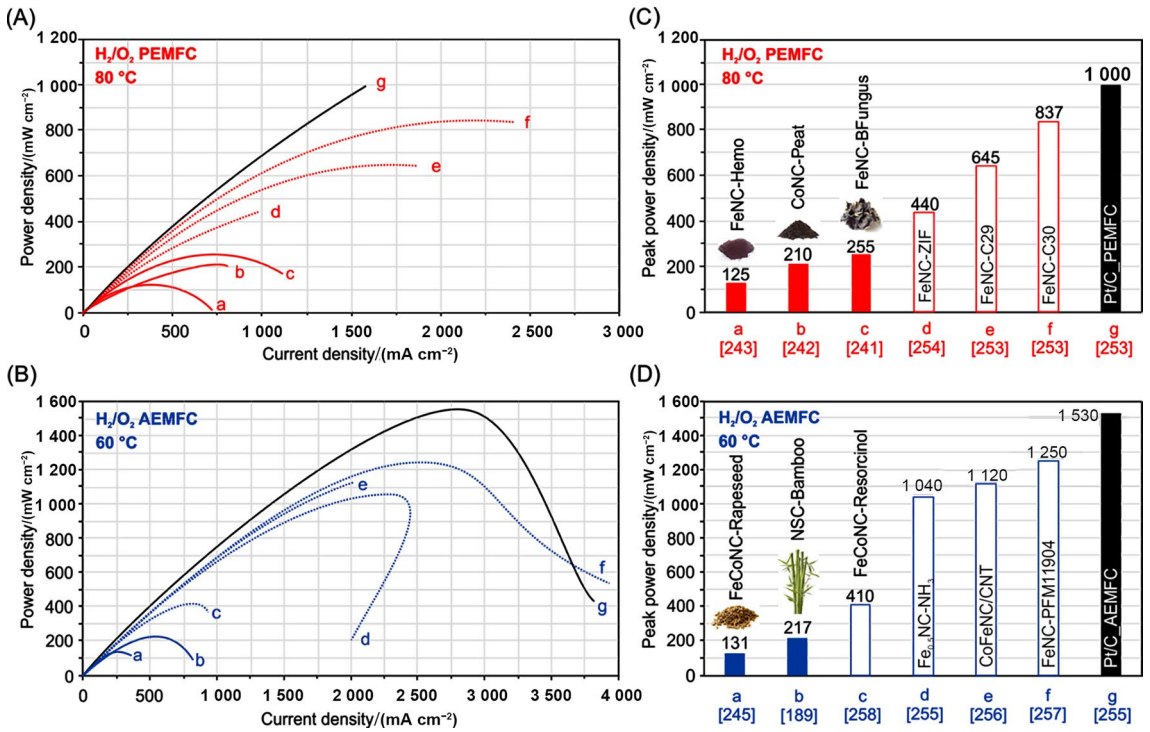

Fig. 16 Polarization curves and related peak power density of **A**, **C** PEMFC and **B, D** AEMFC of biomass-derived electrocatalysts presented in Figs. 13 and 14, compared to the best available electrocatalysts in the literature

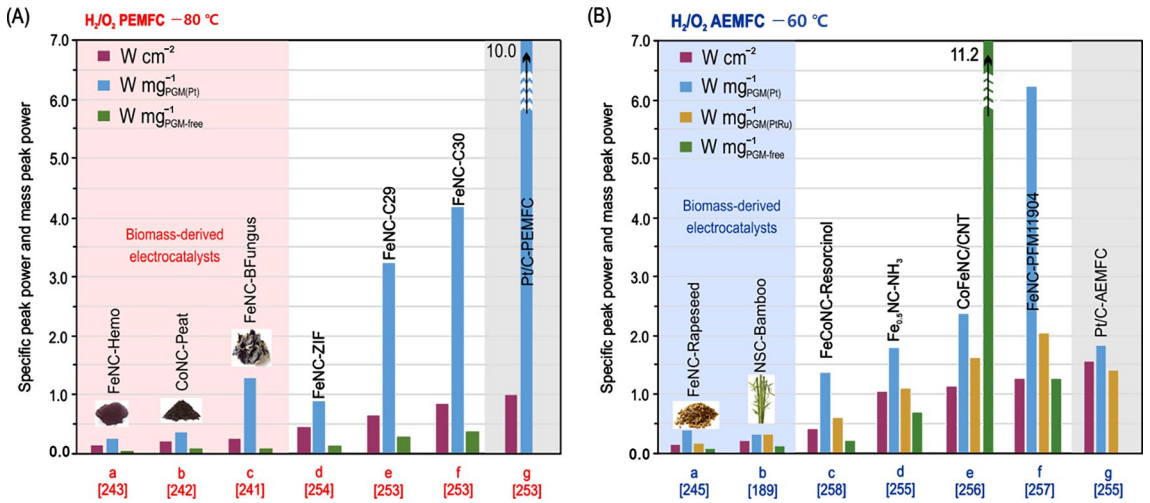

Fig. 17 Specific and mass peak power values of **A** PEMFC and **B** AEMFC of biomass-derived electrocatalysts presented in Fig. 16, compared to the best available FeNC and Pt/C electrocatalysts in the literature

of the ZAB with the glossy privet-derived electrocatalyst, the other ones reached peak power density in the range of 90–221 mW cm^{-2}. These values are in line with the power peak density values of ZABs available in the literature, fabricated with Fe–N–C electrocatalysts (but not derived from biomass), with power density values below 300 mW cm^{-2} [177]. This relatively low performance can be attributed to the moderately low density of Fe-N_x active sites of Fe–N–C electrocatalysts, which obliges to increase the loading on the electrode. As a consequence, the thicker electrocatalytic layer limits the mass transport of air. Indeed, mass transport problems could be enhanced by flooding problems in the case the electrocatalysts have a relatively large micropores volume [250], exactly the same problems affecting the performance in fuel cell applications [173,

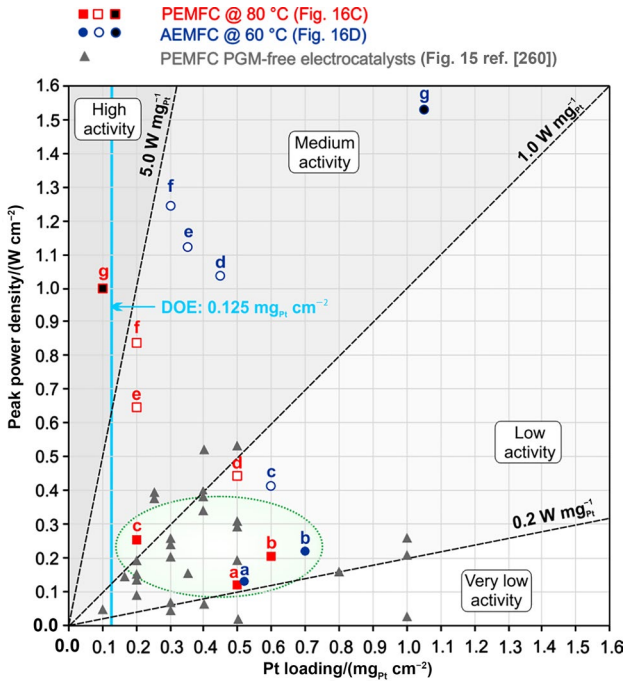

Fig. 18 Peak power density dependency on Pt loading (anode side) for the electrocatalysts analyzed in Fig. 16. Blue symbols: PEMFC at 80 °C. Red symbols: AEMFC at 60 °C. Gray symbols: PGM-free performance of PEMFC as from Fig. 15 of the paper of Brouzgou et al. [260] and its references. The comparison is only qualitative since operative conditions can be different from one reference to another

251]. The biomass-derived ZABs were mostly used to power light-emitting diodes (LED) of different voltage (white, green, blue and red, in the range 3.0–3.2 V) for verifying long time performance. Also the rechargeability of ZAB was assessed, through a series of discharge/charge cycling up to 500 h (with glossy privet fruit derive electrocatalyst), demonstrating a high detention of the initial discharge potential (1.18/1.13 V at the beginning/end of cycling) [20].

10 Critical Considerations on Biomass-Derived Electrocatalysts

So far, we reviewed a good number of papers presenting PGM-free electrocatalysts derived from "any" kind of biomass with electrochemical data acquired in RDE/RRDE, while papers with data acquired in PEMFC/AEMFC are much less abundant. All the examined results share very similar values, either in terms of onset potential or half-wave potential (RDE/RRDE papers) or peak power density (PEMFC/AEMFC papers), making it difficult to create a ranking to identify the best performance. Further, most of the works reported the electrocatalytic properties of the different materials for ORR without testing the same materials for simple outer-sphere redox reactions, in order to estimate the real surface area and the effect of different electrode porosities on the electrochemical response using a simple redox reaction. Thus, the rather large dispersion of data might not only reflect different electrocatalytic activities, but also differences in the real surface area of the various materials, since they have not smooth surfaces.

Focusing the attention on PEMFC or AEMFC testing, the results are presented as "good" or "satisfactory" by the authors. But, if we take into consideration the performance targets suggested by the U.S. Department of Energy (DOE) [96, 252], usually taken as milestone target to become an interesting material for possible scale-up and commercialization (Table 5), all the biomass-derived electrocatalysts results are "not good" and "not satisfactory". They are quite far from the target of 44 mA cm^{-2} @ 900 mV$_{IR\text{-}free}$. This is valid for both PEMFC and AEMFC.

Figure 16 highlights a comparison of polarization curves and peak power densities of the analyzed biomass-derived PEMFC ([241–243] from Fig. 13) and AEMFC ([189, 245] from Fig. 14), compared to the best available and most recent performance of PGM-free electrocatalysts (not derived from biomass) [253–258] and Pt/C-based electrocatalysts [253, 255]. The difference in the peak power density shows great differences (from 125 to 837 mW cm^{-2} for PEMFC, and from 131 to 1 250 mW cm^{-2} for AEMFC), demonstrating that the biomass-derived electrocatalysts are still far from interesting values to be exploited.

To be fair, the performance comparison should be done in terms of specific or mass peak power density, as illustrated in Fig. 17. The mass peak power density can be evaluated considering the total amount of PGM-free electrocatalyst, or the amount of PGM electrocatalyst (present at the anode side, Pt for PEMFC, PtRu for AEMFC). Also considering this point of view, the performance of the biomass-derived electrocatalysts is not comparable to those of the other PGM-free electrocatalysts considered, being the difference more than one order of magnitude lower. Interestingly, the best PGM-free performance, either in PEMFC (at 80 °C) and AEMFC (at 60 °C), has been reached with a series of commercial electrocatalysts [253, 257] produced and commercialized by Pajarito Powder [259] using the VariPore™ method. These electrocatalysts, Fe–N–C type ("precious-metal-free" catalysts C29, C30, PMF-11904 [253, 257]), synthesized by hard-templating method followed by pyrolysis at high temperature, have been on purpose engineered to reach an optimal amount of atomically Fe–N$_x$ active sites (to increase activity), a sufficiently high degree of graphitization (to increase durability), a hierarchical porous structure with micro- and meso-pores (V_{micro} to favor the formation of the active sites and enhance their utilization, V_{meso} to favor the removal of water as reaction product and avoid flooding and starvation), a sufficiently low hydrophilicity (to improve

mass transport properties of water). Indeed, this synthesis method has been scaled-up for industrial production. The performance gap existing between biomass-derived electrocatalysts and Pt/C based ones has been reduced with the commercial engineered Fe–N–C electrocatalysts in acidic environment, and overpassed in alkaline environment.

The low activity of the analyzed AEMFC/PEMFC with biomass-derived electrocatalysts at the cathode is even clearer by considering their activity as a function of the loading of Pt at the anode side, necessary to oxidize hydrogen. Pt is a rare and scarce element, extremely expensive, thus the lower its loading in fuel cells, the better. The limit of Pt loading (anode plus cathode) suggested by the DOE is 0.125 mg cm^{-2} [96, 260]. Fig. 18 shows the performance of the electrocatalysts analyzed in Fig. 16 in terms of maximum peak power density as a function of the total Pt loading. The performance of an electrocatalyst can be classified as high (> 5 W mg_{Pt}^{-1}), medium (between 5 and 1 W mg_{Pt}^{-1}), low (between 1 and 0.2 W mg_{Pt}^{-1}), or very low (< 0.2 W mg_{Pt}^{-1}). The analyzed AEMFCs/PEMFCs with biomass-derived electrocatalysts at the cathode have an anode Pt loading (from 0.2 to 0.7 mg cm^{-2}) higher than the DOE suggestion (0.125 mg cm^{-2}). Thus, their activities can be considered low or very low (green circle in the Figure). The MEAs fabricated with the commercial PGM-free electrocatalysts at the cathode reached a medium activity, with a lower content of Pt at the anode, but still higher compared to the suggested value from DOE. The gray triangles represent the performance of several PEMFCs with PGM-free electrocatalysts at the cathode, according to a literature survey performed by Brougzou et al. [260]: the values are low, and far from the values obtained with commercial PGM-free electrocatalysts, or Pt-based ones. For sake of clarity it is worth noting that in the literature, Adabi et al. [257] reached a peak power density of 2 W cm^{-2} with the commercial PGM-free electrocatalyst PMF-11904 in an AEMFC operating at 80 °C (the same electrocatalyst "f" of Fig. 16B, which provided 1.25 W cm^{-2} at 60 °C). Moreover, the same PMF-11904 electrocatalyst, used to fabricate another MEA with a reduced Pt loading (0.125 mg_{PtRu} cm^{-2}; 0.08 mg_{Pt} cm^{-2}) reached a specific power output of 16.4 W mg_{Pt}^{-1} (10.4 W mg_{PtRu}^{-1}) at 80 °C, which is the best performance reached so far in AEMFCs, to our knowledge. This performance outperformed the 2020 DOE targets of Table 5.

By deeply analyzing Table 2, we can observe that on average, almost all electrocatalysts investigated by various groups and presented in this review have relatively high content of graphitic-N and pyridinic-N, usually a higher content compared to that of oxidized-N and pyrrolic-N. As highly debated in the literature, graphitic-N and pyridinic-N are usually recognized as the most important functionalities not only to form active sites [95, 106, 118, 261], but also to contribute effectively to the ORR activity. Fe–N_4 is commonly recognized as the main active site of Fe–N–C electrocatalysts [95, 106]. Spectroscopic and imaging analyses ascertained that Fe-N_4 sites are bound by pyridinic moieties fused within graphitic sheets [262–265]. Recently, Marshall-Roth et al. [266] proved that pyridine-based bond increases ORR activity thanks to a positive shift of the $Fe^{3+/2+}$ potential. Moreover, graphitic–N is expected to enhance the diffusion-limited current density, and pyridinic-N to improve the onset potential, the surface wettability and electrical conductivity. Besides, also the specific surface area (S.S.A.) and the total pore/micropore volumes (V_{total} and V_{micro}) are expected to impact the ORR activity [103]. In Fig. 19 we tried to correlate the ORR activity with the physical and surface chemistry descriptors we analyzed. It is important to remark that the following comments reflect the state-of-the-art of the papers we analyzed, which represent a small amount of data compared to the vast amount of electrocatalysts developed worldwide. Anyway, the trends we highlighted are in line with the most common findings in the literature, and clearly demonstrate that: i. biomass-derived electrocatalysts perform better in alkaline environment; ii. there is still a hulky performance gap between biomass-derived electrocatalysts and commercial PGM-free electrocatalysts.

The most important observations can be summarized as follows:

1. At RDE/RRDE level, all papers show "good" or "excellent" activity (according to the authors), sometimes even better than that of a commercial Pt/C electrocatalyst used as a reference (in most of the cases, the commercial electrocatalyst is the 20 wt.% Pt/C from Johnson Matthey). Figure 19A highlights the relationship between E_{onset} and $E_{1/2}$. Interestingly, most of the papers present results only in alkaline electrolyte (blue squares in the Figure), in 0.1 M KOH (Table 2). Very few data are available in acid electrolyte (red squares in the Figure). Coincidentally, the better results in terms of E_{onset} and/or $E_{1/2}$ belong to the studies performed in alkaline medium. This is thanks to the greater ease with which the ORR reaction takes place in alkaline environment, as discussed in the introductory part [27]. For sake of comparison, we also added the E_{onset} and $E_{1/2}$ of the best available and most recent PGM-free electrocatalysts not derived from biomass [253, 255–258] (light blue and pink squares in Fig. 19 for alkaline and acid electrolytes). On average, these values are similar, or higher than the respective biomass-derived electrocatalysts' values.
2. The temperature of pyrolysis (Fig. 19B) at which the electrocatalysts have been synthesized show optimal values in the range 900–1 000 °C, where the E_{onset} and $E_{1/2}$ values are higher. According to literature, the quantity of Fe–N_x active sites can be tuned with high-temperature

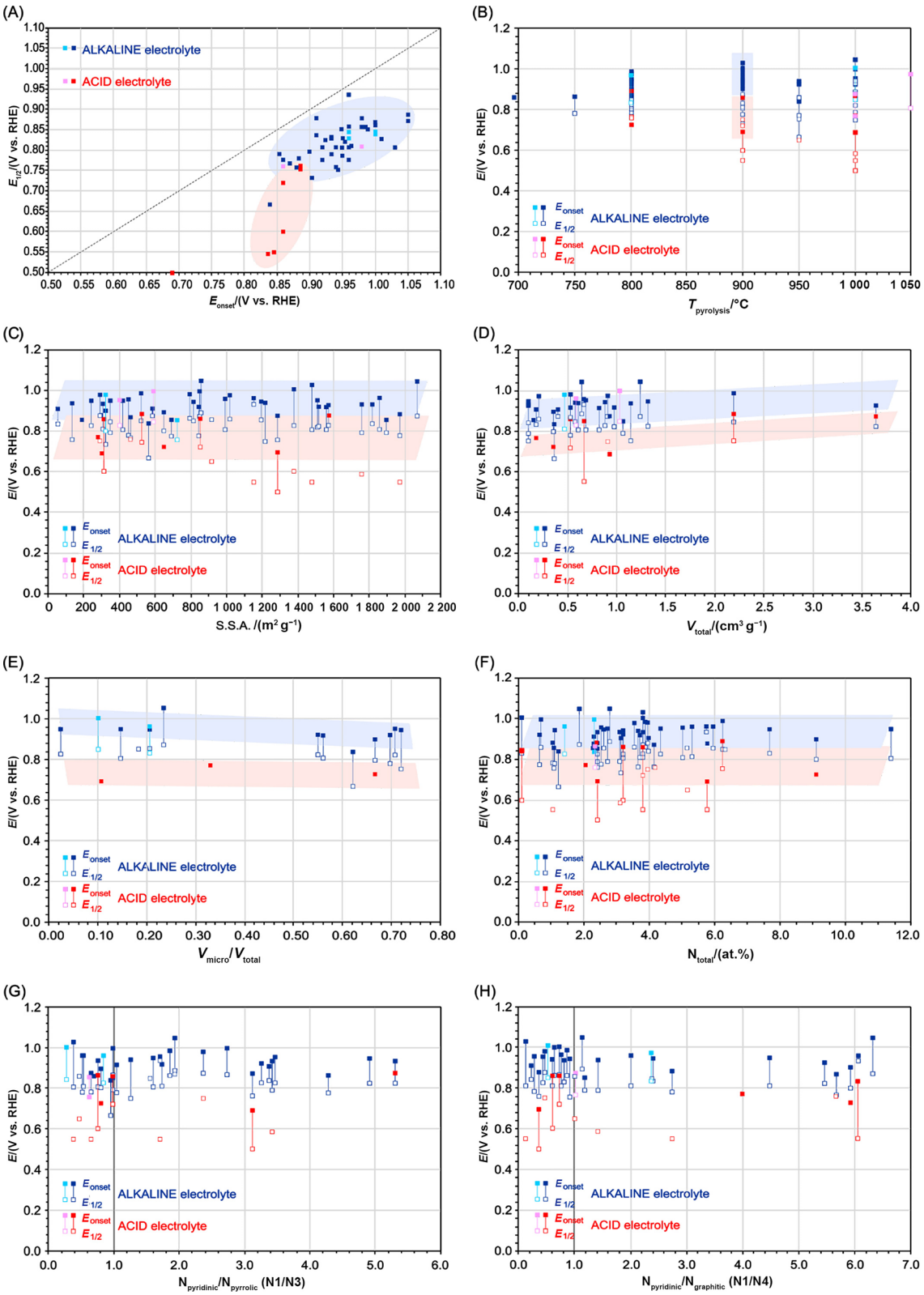

treatments [264]. The gain in the potential attained at 1 000 °C cannot be considered so significant, taking into account of the energy needed during the synthesis to reach such a high temperature. Thus, an optimal temperature of pyrolysis close to 900–950 °C is preferable,

◂**Fig. 19** Possible correlations analyzing all data listed in Table 2 **A** between the onset potential (E_{onset}) and half-wave potential ($E_{1/2}$) in acid or alkaline electrolyte, and then as a function of **B** the temperature of pyrolysis during the synthesis, **C** the specific surface area (S.S.A. from N_2 physisoprtion), **D** the total volume (V_{tot} from N_2 physisoprtion), **E** the ratio between the volume of the micropores and the total volume (V_{micro}/V_{total}), **F** the total nitrogen (N_{tot}, atomic %, from XPS analysis), **G** the N1/N3 ratio (pyridinic-N N1 over pyrrolic-N N3, from XPS analysis), **H** the N1/N4 ratio (pyridinic-N N1 over graphitic-N N4, from XPS analysis). Symbols: PGM-free electrocatalysts of biomass origin (blue) or from inorganic compounds (light blue) tested in alkaline electrolyte; PGM-free electrocatalysts of biomass origin (red) or from inorganic compounds (light red) tested in acid electrolyte

especially in the case of a possible scale-up for a mass production of the electrocatalysts.

3. Observing the physical values from N_2 physisorption analysis (Table 2), E_{onset} and $E_{1/2}$ values are not particularly influenced by the values of the S.S.A. (Fig. 19C). Interestingly, the PGM-free electrocatalysts not derived from biomass taken as a reference have high values of the potential, with relatively low values of the S.S.A. (among them, the two commercial electrocatalysts from Pajarito Powder: FeNC_C30 and FeNC_PFM11904, [253, 257]). In contrast, the pore volume (V_{total}) is playing a more important role: the higher it is, the better the E_{onset} and $E_{1/2}$ are (Fig. 19D). Instead, when the microporosity (V_{micro}) is predominant (Fig. 19E, V_{micro}/V_{total} ratio), the values of E_{onset} and $E_{1/2}$ decrease, because of the reduced mass transport of oxygen into the pores. Interestingly, the two commercial PGM-free electrocatalysts from Pajarito Powder (FeNC-C29 and FeNC-C30, red symbols) have very low values of the V_{micro}/V_{total} ratio. In fact, they have been synthesized on purpose with a higher mesopore volume, with the specific aim of preventing possible flooding effect in fuel cell operation because of capillary water condensation [254, 267, 268]. If pores are somehow blocked, the mass-transport is inhibited, causing an apparent reduction of the ORR activity (till suppression in some cases), even though the intrinsic reaction kinetics is high [269, 270].
4. The overall content of nitrogen (N, at.%, evaluated by XPS analysis, Fig. 19F) contributes to enhance the E_{onset} and $E_{1/2}$ values, because of the higher amount of Fe–N_x (or Co–N_x) active sites for the ORR. Not only, also Fe-free moieties such as pyrrolic-N and pyridinic-N (edge active sites) and graphitic-N (in-plane active site) contribute to ORR activity [95]. Thus, the speciation of N moieties is crucial, because of the plurality of active sites for Fe–N–C electrocatalysts [95]. Fe (or Co) coordination with nitrogen changes depending on nitrogen position in the carbon crystallite. This causes a change in the activity towards ORR. Fe–N_4 and Fe–N_{4+1} are supposed to be the most favorable Fe-containing active sites for the ORR. As an example, Fe-N_{2+2} moieties are preferentially located in micro-pores, while Fe–N_2 (edge moieties), Fe–N_3 and Fe–N_4 (in-plane moieties) in meso-pores. Thus, their activity depends on the orientation of the carbon planes: the more the carbon planes are facing mesopores, the more active the electrocatalyst is [106, 118]. Figure 19G and H correlates the $N_{pyridinic}/N_{pyrrolic}$ (N1/N3, Table 2) and $N_{pyridinic}/N_{graphitic}$ (N1/N4, Table 2) ratios versus the E_{onset} and $E_{1/2}$: it is difficult to outline a specific trend form the data analyzed. Basically, the higher the $N_{pyrydinic}$ and $N_{graphitic}$ values, the better for the ORR activity, in agreement with the literature [264, 266, 271], even if in the literature there are many active electrocatalysts with higher $N_{pyrrolic}$ values, or $N_{pyridinic}/N_{pyrrolic}$ ratio very close to 1. It is important to remark that very recent studies demonstrated that the FeN_x site structure in a pristine catalyst powder is slightly different from the structure it assumes in the electrode [272]. In fact, the presence of solvents (usually water and alcohols) and binders (such as Nafion® ionomer) as binder in the catalytic ink partially modifies the structure of the active sites. The formation of $-O_2$ and $-OH$ bonds during the electrode preparation let the structure of some of the FeN_x sites changing from square planar (or square pyramidal) to octahedral.
5. Even more interestingly, practically all papers display results with better durability (assessed via chronoamperometry or several potential cycling). They also exhibit a better methanol tolerance (assessed by performing chronoamperometry in presence of a high concentration of methanol in the electrolyte) compared to the reference commercial Pt/C (data presented in Figs. 5, 6, 7, 8, 9, 10, 11 and 12). This aspect is common to all PGM-free electrocatalysts (not only the biomass-derived ones), thanks to their zero-selectivity towards the alcohol oxidation [82, 273].

Most of the biomass-derived electrocatalysts examined do not contain Fe, but only non-metal elements such as N, B, P, or S deriving from the original biomass. Practically, the authors used the so-called "naturally" doping effect, using only the chemical characteristics of the biomass, without adding extra Fe or Co. Interestingly, S doping favors oxygen binding and consequently the ORR kinetics [206, 208, 274]. However, oxygen binding should be neither too strong, nor too weak, to be located on or close to the top of the volcano activity correlation, favoring thus the kinetics of ORR [51, 122, 275, 276]. Furthermore, the co-doping of S and N favors also the electronic properties because it affects the π electrons on the carbons by redistributing the spin [277, 278]. According to a series of DTF calculations, the simultaneous doping with N and S on a carbon matrix requires less energy compared to the doping of each single atom, with a

consequent synergistic performance over doping in sequence [279]. The spin redistribution due to the dual doping leads to a large number of carbon active sites [278, 280]. Regrettably, this is not sufficient for a satisfactory ORR activity. Fe, Co, or FeCo, must be added to increase the activity, together with pyridinic nitrogen, to enhance the formation of Fe-N_x active sites, possibly atomically dispersed. As demonstrated by the highest activity reached in AEMFC by Adabi et al. [257] using the commercial Pajarito Powder electrocatalyst, the higher the nitrogen content, the higher the density of Fe-N_x active sites.

Moreover, the synthesis adopted by the various authors never optimized on purpose the porosity of the electrocatalysts to maximize mass transport properties (in fuel cells). The authors mostly looked at the specific surface area. But this descriptor is not indicative of a high activity (see Fig. 16B). Porosity was mainly promoted with KOH activation, which favors the formation of micropores, or H_3PO_4 activation, which favors more the formation of mesopores [281–283]. But none of these treatments allows a specific development of a hierarchical micro-mesoporosity. Thus, while the activity evaluated at RDE/RRDE level reached satisfactory results, the activity evaluated in fuel cell was very low. On this point of view, the specific surface area plays a minor role compared to the nature of the porous structure. Textural properties such a micro-, meso- and macro-pores are of utmost importance to increase the activity of an electrocatalyst towards ORR. Specifically, a narrow pore size distribution in the range of 5–40 nm provides high oxygen accessibility to the active sites during operation while favoring water removal from the reaction sites, especially at high current density. Thus, high peak power density values can be reached. Not by chances the best results with PGM-free electrocatalysts belong to materials prepared with ad-hoc hard templating synthesis where templating agents of several sizes (mostly a mixture of silicas with size from meso to macro). The variety of the templates lead to the formation of a hierarchical porous carbon with networking structure after acid leaching [173, 176, 229, 257, 271, 284, 285]. Additionally, also the graphitization level of the carbon plays an important role in avoiding water starvation, by increasing the hydrophobicity of the electrocatalyst and, of course, the conductivity and stability [286].

Another important aspect is related to the high loading of PGM-free electrocatalyst needed to fabricate MEAs. On a practical point of view, all Fe–N–C electrocatalysts require an average loading of 4 mg cm^{-2} (from 2 to 6 mg cm^{-2}) to compensate for the lower mass activity. The resulting MEAs are very thick (60 to 150 µm), providing further limitation to mass transfer, especially at high operative potentials [114, 287]. As a term of comparison, MEAs realized with PGM electrocatalysts account for Pt loading of 0.05 mg cm^{-2}, resulting thus in thickness of 10 to 20 µm, with much reduced limitations on mass transport [28, 268]. To further improve the performance of PGM-free electrocatalyst performance, it is necessary to increase the density of the active sites that perform the ORR [123].

Considering all these aspects, the provocative paper of Pumera's group [288] is right when it claims that "any crap we put into graphene increases its electroactivity effect". In fact, this electrocatalytic effects does not translate into an effective good performance in the real application, where the performance itself is influenced not only by the intrinsic activity of the electrocatalysts, but also by the mass transport of reactants and products of reaction. On a practical point of view, "the more dopant we use, the more we increase the entropy without a valuable gain".

In the end, considering most of the biomass-derived electrocatalysts synthesized in the recent years, almost all authors claim the use of "waste biomass" as material available for free, that can be recycled. Regrettably, none of them carefully analyzed the production costs in terms of energy required for treating the biomass, or performed a life cycle analysis of the entire production process. In most of the cases, the biomass underwent long-lasting pyrolysis treatments at high temperature, which implied an enormous consumption of energy. The results obtained so far in terms of activity towards ORR are only relatively satisfactory, being order of magnitude far from the activity of some commercial PGM-free electrocatalysts. There is still a great scientific gap to fill.

Interestingly, the biomass starting materials have several advantages over porous graphitic carbons prepared from other precursors like graphene, carbon nanotubes. One of the most important advantages is the low cost, abundance and environmentally friendly. However, due to the great variety of sources, essentially any residues from living matter, the method of preparation and starting materials conditions determine the final properties. This is a very open field of research, highly promising.

This review should be useful for whoever approaches the field and needs to be considered a starting point for the study. Much research work must be done before to obtain an engineered electrocatalyst derived from biomass with a satisfying activity in PEMFC, AEMFC, or ZAB.

11 Conclusions and Perspectives

High catalytic activity is the most important requirement for ORR electrocatalysts, which require specific physical and chemical descriptors such as high specific surface area and hierarchical porosity, high pyridinic-N content, high site density and turn-over frequency. Further, binding energies of O_2 to active sites needs to be moderate according to the Sabatier Principle [72] to obtain the highest activity.

However, durability and selectivity are also important. For example, selectivity for 4-electron reduction of ORR is desired in a fuel cell.

An overview of a number of electrocatalysts obtained by biomass has been reviewed. We have highlighted several types of biomass and different synthetic methods and the role played by these in the structure and their electrocatalytic activity. The enhancement of ORR performance in fuel cells and metal air batteries must be the main driving force for the technological progression in this sector, requiring more efficient, scalable, sustainable and economical materials. The direct preparation of carbonaceous materials from biomass would have a potential advantage on these applications. Because of the renewable nature of the biomass, precursors are easy to produce. Under a controlled pyrolysis process, the structural properties of the biomass can be retained in the final porous carbon material (memory effect), which plays an utmost role in PEMFC/AEMFC and ZAB. The observed trends show that performance improves after doping and/or co-doping with heteroatoms, but yet not enough. These materials suffer from degradation due to corrosion of carbon and leaching of transition metals, even if in a lesser extent compared to Pt/C-based electrocatalysts. This is especially important in acid electrolytes. Already existing commercial PGM-free electrocatalysts outperformed the results obtained so far with biomass-derived materials. However, it is crucial to note that a critical evaluation is important, to avoid the mistake of considering every biomass, even laughable ones (such as hairs, urine, guano), as a valid candidate for electrocatalysts' synthesis, as pointed out by Pumera and coworkers [288]. Biomass heterogeneity and variability of chemical characteristics are still an issue.

The economic feasibility of biomass recycling for electrocatalysts production is still challenging to asses due to the limited data and few full-scale projects in operation. Moreover, the existing performance gap between biomass-derived electrocatalysts and commercial ones is still too high yet to push a process scale-up. In addition, the technology readiness level (TRL) of the examined processes in this review is still too low, below level 3 to 4 ("experimental proof of concept" and "technology validated in lab") to support a solid economic feasibility analysis [289]. Still very far from TRL values 8 and 9 ("system complete and qualified" and "system proven in operational environment with a competitive manufacturing") [289], necessary to afford a possible technological investment. The choice of a technology and its cost-efficiency will depend on factors such as availability of feedstock volume, characteristics and homogeneity, and local policy to favor circular economy and sustainable development [11–13, 290–292]. The next decades will be crucial, the energetic crisis effects are intensifying every day and the industry needs to harvest the developments from new technologies.

Considering the state of the art and benchmarking analysis of biomass-derived electrocatalysts here conducted, we can conclude that these materials are still far to find a niche of application. Even if biomass is an easily available resource, and the synthesis approach to produce electrocatalysts is reproducible, the research has yet to focus on improving the electrocatalytic activity. The good results achieved in terms of better durability towards ORR, and better methanol tolerance compared to Pt/C-based counterparts cannot be considered sufficiently good to replace actual materials. As a general conclusion, there is still room for improvement. Biomass-derived electrocatalysts are in a premature stage of development to be considered yet as a feasible alternative, even if on the point of view of circular economy and sustainable development, this would be a great advantage. The results from this comparative study highlight the actual gap for potential improvement and new development. This review paper is a starting line for researchers, potential investors or institutions aiming at technological solutions for transforming biomass into highly active electrocatalysts for PEM/AEM fuel cells and Zn-air batteries.

Acknowledgements LCS-P acknowledges the ANID Conicyt Doctoral Scholarship No. 21212199 and University of Santiago de Chile. JHZ acknowledges the funding of Fondecyt Grants Nos. 1181260 and 1221798, and Conicyt/ANID PIA Proyect ACT 192175. SS acknowledges the Fondecyt Grant No. 1181037 for funding her visit to University of Santiago de Chile in 2022. SS thanks Prof. Ashwani K. Gupta from University of Maryland (College Park, CT, USA) for the fruitful discussion.

Author contributions Conceptualization: JHZ, SS; Formal analysis and investigation: SZ, LCS-P, JHZ, SS; Writing—original draft preparation: SZ, LCS-P, JHZ, SS; Writing—review and editing: JHZ, SS; Funding acquisition: JHZ; Supervision: JHZ, SS.

Funding Open access funding provided by Politecnico di Torino within the CRUI-CARE Agreement. The authors have no relevant financial or non-financial interests to disclose.

Declarations

Conflict of interest Stefania Specchia is an associate editor for *Electrochemical Energy Reviews* and was not involved in the editorial review or the decision to publish this article. All authors declare that there are no competing interests. The authors have no competing interests to declare that are relevant to the content of this article. The authors have no financial or proprietary interests in any material discussed in this article.

Ethical approval All authors certify that they have no affiliations with or involvement in any organization or entity with any financial interest or non-financial interest in the subject matter or materials discussed in this manuscript.

References

1. Miyamoto, M., Takeuchi, K.: Climate agreement and technology diffusion: impact of the Kyoto Protocol on international patent applications for renewable energy technologies. Energy Policy **129**, 1331–1338 (2019). https://doi.org/10.1016/j.enpol.2019.02.053
2. Mulder, C., Conti, E., Mancinelli, G.: Carbon budget and national gross domestic product in the framework of the Paris climate agreement. Ecol. Indic. **130**, 108066 (2021). https://doi.org/10.1016/j.ecolind.2021.108066
3. Health, T.L.P.: The road to Glasgow. Lancet Planet. Health **5**, e659 (2021). https://doi.org/10.1016/S2542-5196(21)00265-5
4. Maibach, E., Miller, J., Armstrong, F., et al.: Health professionals, the Paris agreement, and the fierce urgency of now. J. Clim. Change Health **1**, 100002 (2021). https://doi.org/10.1016/j.joclim.2020.100002
5. Fragkos, P., Tasios, N., Paroussos, L., et al.: Energy system impacts and policy implications of the European intended nationally determined contribution and low-carbon pathway to 2050. Energy Policy **100**, 216–226 (2017). https://doi.org/10.1016/j.enpol.2016.10.023
6. Seto, K.C., Güneralp, B., Hutyra, L.R.: Global forecasts of urban expansion to 2030 and direct impacts on biodiversity and carbon pools. Proc. Natl. Acad. Sci. USA **109**, 16083–16088 (2012). https://doi.org/10.1073/pnas.1211658109
7. Petković, B., Agdas, A.S., Zandi, Y., et al.: Neuro fuzzy evaluation of circular economy based on waste generation, recycling, renewable energy, biomass and soil pollution. Rhizosphere **19**, 100418 (2021). https://doi.org/10.1016/j.rhisph.2021.100418
8. Chew, K.W., Chia, S.R., Chia, W.Y., et al.: Abatement of hazardous materials and biomass waste via pyrolysis and co-pyrolysis for environmental sustainability and circular economy. Environ. Pollut. **278**, 116836 (2021). https://doi.org/10.1016/j.envpol.2021.116836
9. Velvizhi, G., Balakumar, K., Shetti, N.P., et al.: Integrated biorefinery processes for conversion of lignocellulosic biomass to value added materials: paving a path towards circular economy. Bioresour. Technol. **343**, 126151 (2022). https://doi.org/10.1016/j.biortech.2021.126151
10. Sherwood, J.: The significance of biomass in a circular economy. Bioresour. Technol. **300**, 122755 (2020). https://doi.org/10.1016/j.biortech.2020.122755
11. Jain, A., Sarsaiya, S., Kumar Awasthi, M., et al.: Bioenergy and bio-products from bio-waste and its associated modern circular economy: current research trends, challenges, and future outlooks. Fuel **307**, 121859 (2022). https://doi.org/10.1016/j.fuel.2021.121859
12. Awasthi, M.K., Sarsaiya, S., Patel, A., et al.: Refining biomass residues for sustainable energy and bio-products: an assessment of technology, its importance, and strategic applications in circular bio-economy. Renew. Sust. Energ. Rev. **127**, 109876 (2020). https://doi.org/10.1016/j.rser.2020.109876
13. Kumar Awasthi, M., Yan, B.H., Sar, T., et al.: Organic waste recycling for carbon smart circular bioeconomy and sustainable development: a review. Bioresour. Technol. **360**, 127620 (2022). https://doi.org/10.1016/j.biortech.2022.127620
14. Tuck, C.O., Pérez, E., Horváth, I.T., et al.: Valorization of biomass: deriving more value from waste. Science **337**, 695–699 (2012). https://doi.org/10.1126/science.1218930
15. Tripathi, N., Hills, C.D., Singh, R.S., et al.: Biomass waste utilisation in low-carbon products: harnessing a major potential resource. npj. Clim. Atmos. Sci. **2**, 35 (2019). https://doi.org/10.1038/s41612-019-0093-5
16. United Nations Environment Programme: Converting waste agricultural biomass into a resource-compendium of technologies. United Nations Environment Programme, International Environmental Technology Centre, Osaka/Shiga, Japan. Knowledge Repository (2009)
17. Titirici, M.M., Antonietti, M.: ChemInform abstract: chemistry and materials options of sustainable carbon materials made by hydrothermal carbonization. ChemInform (2010). https://doi.org/10.1002/chin.201016219
18. Schlee, P., Hosseinaei, O., Baker, D., et al.: From waste to wealth: from kraft lignin to free-standing supercapacitors. Carbon **145**, 470–480 (2019). https://doi.org/10.1016/j.carbon.2019.01.035
19. Yao, Z.Z., Ma, J.H., Hoang, T.K.A., et al.: High performance biomass-derived catalysts for the oxygen reduction reaction with excellent methanol tolerance. Int. J. Hydrog. Energy **45**, 27026–27035 (2020). https://doi.org/10.1016/j.ijhydene.2020.07.023
20. Liu, Y.Y., Sun, K., Cui, X.Y., et al.: Defect-rich, graphenelike carbon sheets derived from biomass as efficient electrocatalysts for rechargeable zinc–air batteries. ACS Sustain. Chem. Eng. **8**, 2981–2989 (2020). https://doi.org/10.1021/acssuschemeng.9b07621
21. Fakayode, O.A., Yusuf, B.A., Zhou, C.S., et al.: Simplistic two-step fabrication of porous carbon-based biomass-derived electrocatalyst for efficient hydrogen evolution reaction. Energy Conv. Manag. **227**, 113628 (2021). https://doi.org/10.1016/j.enconman.2020.113628
22. Du, L., Zhang, G.X., Liu, X.H., et al.: Biomass-derived nonprecious metal catalysts for oxygen reduction reaction: the demand-oriented engineering of active sites and structures. Carbon Energy **2**, 561–581 (2020). https://doi.org/10.1002/cey2.73
23. Jiang, M.H., Yu, X.F., Yang, H.Q., et al.: Optimization strategies of preparation of biomass-derived carbon electrocatalyst for boosting oxygen reduction reaction: a minireview. Catalysts **10**, 1472 (2020). https://doi.org/10.3390/catal10121472
24. Kaur, P., Verma, G., Sekhon, S.S.: Biomass derived hierarchical porous carbon materials as oxygen reduction reaction electrocatalysts in fuel cells. Prog. Mater. Sci. **102**, 1–71 (2019). https://doi.org/10.1016/j.pmatsci.2018.12.002
25. Coralli, A., Sarruf, B.J.M., de Miranda, P.E.V., et al.: Fuel cells. In: de Miranda, P.E.V. (ed.) Science and Engineering of Hydrogen-Based Energy Technologies, pp. 39–122. Elsevier, Amsterdam (2019). https://doi.org/10.1016/B978-0-12-814251-6.00002-2
26. Anson, C.W., Stahl, S.S.: Mediated fuel cells: soluble redox mediators and their applications to electrochemical reduction of O_2 and oxidation of H_2, alcohols, biomass, and complex fuels. Chem. Rev. **120**, 3749–3786 (2020). https://doi.org/10.1021/acs.chemrev.9b00717
27. Ramaswamy, N., Mukerjee, S.: Fundamental mechanistic understanding of electrocatalysis of oxygen reduction on Pt and non-Pt surfaces: acid versus alkaline media. Adv. Phys. Chem. **2012**, 1–17 (2012). https://doi.org/10.1155/2012/491604
28. Osmieri, L., Meyer, Q.: Recent advances in integrating platinum group metal-free catalysts in proton exchange membrane fuel cells. Curr. Opin. Electrochem. **31**, 100847 (2022). https://doi.org/10.1016/j.coelec.2021.100847
29. Muhyuddin, M., Friedman, A., Poli, F., et al.: Lignin-derived bimetallic platinum group metal-free oxygen reduction reaction electrocatalysts for acid and alkaline fuel cells. J. Power Sources **556**, 232416 (2023). https://doi.org/10.1016/j.jpowsour.2022.232416

30. Weiss, J., Zhang, H.G., Zelenay, P.: Recent progress in the durability of Fe-N-C oxygen reduction electrocatalysts for polymer electrolyte fuel cells. J. Electroanal. Chem. **875**, 114696 (2020). https://doi.org/10.1016/j.jelechem.2020.114696
31. Osmieri, L., Park, J., Cullen, D.A., et al.: Status and challenges for the application of platinum group metal-free catalysts in proton-exchange membrane fuel cells. Curr. Opin. Electrochem. **25**, 100627 (2021). https://doi.org/10.1016/j.coelec.2020.08.009
32. Choi, C.H., Choi, W.S., Kasian, O., et al.: Unraveling the nature of sites active toward hydrogen peroxide reduction in Fe-N-C catalysts. Angew. Chem.-Int. Edit. **56**, 8809–8812 (2017). https://doi.org/10.1002/anie.201704356
33. Chen, Q., Tan, X., Liu, Y., et al.: Biomass-derived porous graphitic carbon materials for energy and environmental applications. J. Mater. Chem. A **8**, 5773–5811 (2020). https://doi.org/10.1039/c9ta11618d
34. Barrio, J., Pedersen, A., Favero, S., et al.: Bioinspired and bioderived aqueous electrocatalysis. Chem. Rev. **123**, 2311–2348 (2023). https://doi.org/10.1021/acs.chemrev.2c00429
35. Zhang, L.W., Jiao, X.D., He, G.J., et al.: Iron phthalocyanine decorated porous biomass-derived carbon as highly effective electrocatalyst for oxygen reduction reaction. J. Environ. Chem. Eng. **11**, 109676 (2023). https://doi.org/10.1016/j.jece.2023.109676
36. Cao, Y., Sun, Y.G., Zheng, R.T., et al.: Biomass-derived carbon material as efficient electrocatalysts for the oxygen reduction reaction. Biomass Bioenergy **168**, 106676 (2023). https://doi.org/10.1016/j.biombioe.2022.106676
37. Lee, H.J., Lee, J.S., Lim, S.Y.: Durable N-doped carbon electrocatalysts derived from NH_3-activated coffee waste for the oxygen reduction reaction. J. Electroanal. Chem. **938**, 117468 (2023). https://doi.org/10.1016/j.jelechem.2023.117468
38. Jalalah, M., Han, H., Nayak, A.K., et al.: Biomass-derived metal-free porous carbon electrocatalyst for efficient oxygen reduction reactions. J. Taiwan Inst. Chem. Eng. **147**, 104905 (2023). https://doi.org/10.1016/j.jtice.2023.104905
39. Wu, X.X., Chen, K.Q., Lin, Z.P., et al.: Nitrogen doped graphitic carbon from biomass as non noble metal catalyst for oxygen reduction reaction. Mater. Today Energy **13**, 100–108 (2019). https://doi.org/10.1016/j.mtener.2019.05.004
40. Liu, X.J., Culhane, C., Li, W.Y., et al.: Spinach-derived porous carbon nanosheets as high-performance catalysts for oxygen reduction reaction. ACS Omega **5**, 24367–24378 (2020). https://doi.org/10.1021/acsomega.0c02673
41. Zhu, C.Y., Zhao, B., Takata, M., et al.: Biomass derived porous carbon for superior electrocatalysts for oxygen reduction reaction. J. Appl. Electrochem. **53**, 1379–1388 (2023). https://doi.org/10.1007/s10800-023-01859-2
42. Zhang, Z.P., Yang, S.X., Li, H.Y., et al.: Sustainable carbonaceous materials derived from biomass as metal-free electrocatalysts. Adv. Mater. **31**, 1805718 (2019). https://doi.org/10.1002/adma.201805718
43. Borghei, M., Lehtonen, J., Liu, L., et al.: Electrocatalysts: advanced biomass-derived electrocatalysts for the oxygen reduction reaction. Adv. Mater. **30**, 1870171 (2018). https://doi.org/10.1002/adma.201870171
44. De, S., Balu, A.M., Van der Waal, J.C., et al.: Biomass-derived porous carbon materials: synthesis and catalytic applications. ChemCatChem **7**, 1608–1629 (2015). https://doi.org/10.1002/cctc.201500081
45. Koper, M.T.M.: Thermodynamic theory of multi-electron transfer reactions: implications for electrocatalysis. J. Electroanal. Chem. **660**, 254–260 (2011). https://doi.org/10.1016/j.jelechem.2010.10.004
46. Li, Y.H., Li, Q.Y., Wang, H.Q., et al.: Recent progresses in oxygen reduction reaction electrocatalysts for electrochemical energy applications. Electrochem. Energy Rev. **2**, 518–538 (2019). https://doi.org/10.1007/s41918-019-00052-4
47. Stacy, J., Regmi, Y.N., Leonard, B., et al.: The recent progress and future of oxygen reduction reaction catalysis: a review. Renew. Sust. Energy Rev. **69**, 401–414 (2017). https://doi.org/10.1016/j.rser.2016.09.135
48. Ge, X.M., Sumboja, A., Wuu, D., et al.: Oxygen reduction in alkaline media: from mechanisms to recent advances of catalysts. ACS Catal. **5**, 4643–4667 (2015). https://doi.org/10.1021/acscatal.5b00524
49. Shao, M.H., Adzic, R.R.: Spectroscopic identification of the reaction intermediates in oxygen reduction on gold in alkaline solutions. J. Phys. Chem. B **109**, 16563–16566 (2005). https://doi.org/10.1021/jp053450s
50. Sepa, D.B., Vojnovic, M.V., Damjanovic, A.: Kinetics and mechanism of O_2 reduction at Pt in alkaline solutions. Electrochim. Acta **25**, 1491–1496 (1980). https://doi.org/10.1016/0013-4686(80)87167-2
51. Zagal, J.H., Koper, M.T.M.: Reactivity descriptors for the activity of molecular MN_4 catalysts for the oxygen reduction reaction. Angew. Chem.-Int. Edit. **55**, 14510–14521 (2016). https://doi.org/10.1002/anie.201604311
52. Masa, J., Ozoemena, K., Schuhmann, W., et al.: Oxygen reduction reaction using N_4-metallomacrocyclic catalysts: fundamentals on rational catalyst design. J. Porphyrins Phthalocyanines **16**, 761–784 (2012). https://doi.org/10.1142/s1088424612300091
53. Zúñiga, C., Candia-Onfray, C., Venegas, R., et al.: Elucidating the mechanism of the oxygen reduction reaction for pyrolyzed Fe-N-C catalysts in basic media. Electrochem. Commun. **102**, 78–82 (2019). https://doi.org/10.1016/j.elecom.2019.04.005
54. Zagal, J.H., Bedioui, F., Dodelet, J.P. (eds.): N_4-Macrocyclic Metal Complexes. Springer, New York (2006). https://link.springer.com/book/10.1007/978-0-387-28430-9
55. Zagal, J.H., Bedioui, F. (eds.): Electrochemistry of N_4 Macrocyclic Metal Complexes. Springer, Switzerland, Basel (2016). https://link.springer.com/book/10.1007/978-3-319-31172-2
56. Schmickler, W., Santos, E.: Interfacial Electrochemistry, 2nd edn. Springer, Berlin, Heildelberg (2010). https://link.springer.com/book/10.1007/978-3-642-04937-8
57. Wroblowa, H.S., Razumney, G.: Electroreduction of oxygen. J. Electroanal. Chem. Interfacial Electrochem. **69**, 195–201 (1976). https://doi.org/10.1016/S0022-0728(76)80250-1
58. Wroblowa, H.S., Qaderi, S.B.: Mechanism and kinetics of oxygen reduction on steel. J. Electroanal. Chem. Interfacial Electrochem. **279**, 231–242 (1990). https://doi.org/10.1016/0022-0728(90)85179-9
59. Hsueh, K.L., Chin, D.T., Srinivasan, S.: Electrode kinetics of oxygen reduction. J. Electroanal. Chem. Interfacial Electrochem. **153**, 79–95 (1983). https://doi.org/10.1016/s0022-0728(83)80007-2
60. Anastasijević, N.A., Vesović, V., Adžić, R.R.: Determination of the kinetic parameters of the oxygen reduction reaction using the rotating ring-disk electrode. J. Electroanal. Chem. Interfacial Electrochem. **229**, 305–316 (1987). https://doi.org/10.1016/0022-0728(87)85148-3
61. Vesovic, V., Anastasijevic, N., Adzic, R.R.: Rotating disk electrode: a re-examination of some kinetic criteria with a special reference to oxygen reduction. J. Electroanal. Chem. Interfacial Electrochem. **218**, 53–63 (1987). https://doi.org/10.1016/0022-0728(87)87005-5
62. Strobl, J.R., Georgescu, N.S., Scherson, D.: Solution phase superoxide as an intermediate in the oxygen reduction reaction on glassy carbon in alkaline media. Electrochim. Acta **335**, 135432 (2020). https://doi.org/10.1016/j.electacta.2019.135432
63. Ma, R.G., Lin, G.X., Zhou, Y., et al.: A review of oxygen reduction mechanisms for metal-free carbon-based electrocatalysts.

Npj Comput. Mater. **5**, 78 (2019). https://doi.org/10.1038/s41524-019-0210-3
64. Viswanathan, V., Hansen, H.A., Rossmeisl, J., et al.: Universality in oxygen reduction electrocatalysis on metal surfaces. ACS Catal. **2**, 1654–1660 (2012). https://doi.org/10.1021/cs300227s
65. Wroblowa, H.S., Yen-Chi-Pan, Razumney, G.: Electroreduction of oxygen. J. Electroanal. Chem. Interfacial Electrochem. **69**, 195–201 (1976). Doi: https://doi.org/10.1016/s0022-0728(76)80250-1
66. Bagotskii, V.S., Tarasevich, M.R., Filinovskii, V.Y.: Calculation of the kinetic parameters of conjugated reactions of oxygen and hydrogen peroxide. Elektrokhimiya **5**, 1218–1226 (1969)
67. Robson, M.H., Serov, A., Artyushkova, K., et al.: A mechanistic study of 4-aminoantipyrine and iron derived non-platinum group metal catalyst on the oxygen reduction reaction. Electrochim. Acta **90**, 656–665 (2013). https://doi.org/10.1016/j.electacta.2012.11.025
68. Greeley, J., Markovic, N.M.: The road from animal electricity to green energy: combining experiment and theory in electrocatalysis. Energy Environ. Sci. **5**, 9246–9256 (2012). https://doi.org/10.1039/C2EE21754F
69. Wang, Y., Zhang, Z.S., Zhang, X., et al.: Theory-driven design of electrocatalysts for the two-electron oxygen reduction reaction based on dispersed metal phthalocyanines. CCS Chem. **4**, 228–236 (2022). https://doi.org/10.31635/ccschem.021.202000590
70. Tian, Z.Q., Wang, Y., Li, Y.L., et al.: Theoretical study of the effect of coordination environment on the activity of metal macrocyclic complexes as electrocatalysts for oxygen reduction. iScience **25**, 104557 (2022). https://doi.org/10.1016/j.isci.2022.104557
71. Mukherjee, B.: Investigation of FePc nanoribbon as ORR catalyst in alkaline medium: a DFT based approach. J. Electrochem. Soc. **165**, J3231–J3235 (2018). https://doi.org/10.1149/2.291815jes
72. Medford, A.J., Vojvodic, A., Hummelshøj, J.S., et al.: From the Sabatier principle to a predictive theory of transition-metal heterogeneous catalysis. J. Catal. **328**, 36–42 (2015). https://doi.org/10.1016/j.jcat.2014.12.033
73. Jaouen, F., Dodelet, J.P.: O_2 reduction mechanism on non-noble metal catalysts for PEM fuel cells. Part I: experimental rates of O_2 electroreduction, H_2O_2 electroreduction, and H_2O_2 disproportionation. J. Phys. Chem. C **113**, 15422–15432 (2009). https://doi.org/10.1021/jp900837e
74. Jaouen, F.: O_2 reduction mechanism on non-noble metal catalysts for PEM fuel cells. Part II: a porous-electrode model to predict the quantity of H_2O_2 detected by rotating ring-disk electrode. J. Phys. Chem. C **113**, 15433–15443 (2009). https://doi.org/10.1021/jp900838x
75. Liu, K.X., Qiao, Z., Hwang, S., et al.: Mn- and N-doped carbon as promising catalysts for oxygen reduction reaction: theoretical prediction and experimental validation. Appl. Catal. B-Environ. **243**, 195–203 (2019). https://doi.org/10.1016/j.apcatb.2018.10.034
76. Kinoshita, K.: Electrochemical Oxygen Technology. Wiley, London (1992)
77. Chlistunoff, J.: RRDE and voltammetric study of ORR on pyrolyzed Fe/polyaniline catalyst on the origins of variable tafel slopes. J. Phys. Chem. C **115**, 6496–6507 (2011). https://doi.org/10.1021/jp108350t
78. Sui, S., Wang, X.Y., Zhou, X.T., et al.: A comprehensive review of Pt electrocatalysts for the oxygen reduction reaction: nanostructure, activity, mechanism and carbon support in PEM fuel cells. J. Mater. Chem. A **5**, 1808–1825 (2017). https://doi.org/10.1039/c6ta08580f
79. Baglio, V., Aricò, A.S., Antonucci, V., et al.: An NMR spectroscopic study of water and methanol transport properties in DMFC composite membranes: influence on the electrochemical behaviour. J. Power Sources **163**, 52–55 (2006). https://doi.org/10.1016/j.jpowsour.2006.01.065
80. Vasile, N.S., Monteverde Videla, A.H.A., Simari, C., et al.: Influence of membrane-type and flow field design on methanol crossover on a single-cell DMFC: an experimental and multi-physics modeling study. Int. J. Hydrog. Energy **42**, 27995–28010 (2017). https://doi.org/10.1016/j.ijhydene.2017.06.214
81. Simari, C., Vecchio, C.L., Baglio, V., et al.: Sulfonated polyethersulfone/polyetheretherketone blend as high performing and cost-effective electrolyte membrane for direct methanol fuel cells. Renew. Energy **159**, 336–345 (2020). https://doi.org/10.1016/j.renene.2020.06.053
82. Sebastián, D., Serov, A., Matanovic, I., et al.: Insights on the extraordinary tolerance to alcohols of Fe-N-C cathode catalysts in highly performing direct alcohol fuel cells. Nano Energy **34**, 195–204 (2017). https://doi.org/10.1016/j.nanoen.2017.02.039
83. Berretti, E., Osmieri, L., Baglio, V., et al.: Direct alcohol fuel cells: a comparative review of acidic and alkaline system. Electrochem. Electrochem. Energy Rev. **6**, 30 (2023). https://doi.org/10.1007/s41918-023-00189-3
84. Sasaki, K., Naohara, H., Cai, Y., et al.: Core-protected platinum monolayer shell high-stability electrocatalysts for fuel-cell cathodes. Angew. Chem.-Int. Edit. **49**, 8602–8607 (2010). https://doi.org/10.1002/anie.201004287
85. Shao, Y.Y., Dodelet, J.P., Wu, G., et al.: PGM-free cathode catalysts for PEM fuel cells: a mini-review on stability challenges. Adv. Mater. **31**, 1807615 (2019). https://doi.org/10.1002/adma.201807615
86. Shao, M.H., Sasaki, K., Adzic, R.R.: Pd–Fe nanoparticles as electrocatalysts for oxygen reduction. J. Am. Chem. Soc. **128**, 3526–3527 (2006). https://doi.org/10.1021/ja060167d
87. Johnson Matthey precious metals management. http://www.platinum.matthey.com/prices/price-charts
88. Statistica. https://www.statista.com/statistics/273645/global-mine-production-of-platinum/
89. Yang, H., Alonso-Vante, N., Léger, J.M., et al.: Tailoring, structure, and activity of carbon-supported nanosized Pt–Cr alloy electrocatalysts for oxygen reduction in pure and methanol-containing electrolytes. J. Phys. Chem. B **108**, 1938–1947 (2004). https://doi.org/10.1021/jp030948q
90. Esfahani, R.A.M., Vankova, S.K., Monteverde Videla, A.H.A., et al.: Innovative carbon-free low content Pt catalyst supported on Mo-doped titanium suboxide (Ti_3O_5-Mo) for stable and durable oxygen reduction reaction. Appl. Catal. B-Environ. **201**, 419–429 (2017). https://doi.org/10.1016/j.apcatb.2016.08.041
91. Kuroki, H., Tamaki, T., Matsumoto, M., et al.: Platinum–iron–nickel trimetallic catalyst with superlattice structure for enhanced oxygen reduction activity and durability. Ind. Eng. Chem. Res. **55**, 11458–11466 (2016). https://doi.org/10.1021/acs.iecr.6b02298
92. Rudi, S., Teschner, D., Beermann, V., et al.: pH-induced versus oxygen-induced surface enrichment and segregation effects in Pt–Ni alloy nanoparticle fuel cell catalysts. ACS Catal. **7**, 6376–6384 (2017). https://doi.org/10.1021/acscatal.7b00996
93. Čolić, V., Bandarenka, A.S.: Pt alloy electrocatalysts for the oxygen reduction reaction: from model surfaces to nanostructured systems. ACS Catal. **6**, 5378–5385 (2016). https://doi.org/10.1021/acscatal.6b00997
94. Wang, Y., Chen, K.S., Mishler, J., et al.: A review of polymer electrolyte membrane fuel cells: technology, applications, and needs on fundamental research. Appl. Energy **88**, 981–1007 (2011). https://doi.org/10.1016/j.apenergy.2010.09.030
95. Asset, T., Atanassov, P.: Iron-nitrogen-carbon catalysts for proton exchange membrane fuel cells. Joule **4**, 33–44 (2020). https://doi.org/10.1016/j.joule.2019.12.002
96. Thompson, S.T., Wilson, A.R., Zelenay, P., et al.: ElectroCat: DOE's approach to PGM-free catalyst and electrode R&D. Solid State Ion. **319**, 68–76 (2018). https://doi.org/10.1016/j.ssi.2018.01.030

97. Shao, M.H., Chang, Q.W., Dodelet, J.P., et al.: Recent advances in electrocatalysts for oxygen reduction reaction. Chem. Rev. **116**, 3594–3657 (2016). https://doi.org/10.1021/acs.chemrev.5b00462
98. Osmieri, L., Pezzolato, L., Specchia, S.: Recent trends on the application of PGM-free catalysts at the cathode of anion exchange membrane fuel cells. Curr. Opin. Electrochem. **9**, 240–256 (2018). https://doi.org/10.1016/j.coelec.2018.05.011
99. Wang, H., Chen, B., Liu, D.-J., et al.: Nanoarchitectonics of metal-organic frameworks for capacitive deionization via controlled pyrolyzed approaches. Small **18**, 2102477 (2022). https://doi.org/10.1002/smll.202102477
100. Jasinski, R.: A new fuel cell cathode catalyst. Nature **201**, 1212–1213 (1964). https://doi.org/10.1038/2011212a0
101. Gong, K.P., Du, F., Xia, Z.H., et al.: Nitrogen-doped carbon nanotube arrays with high electrocatalytic activity for oxygen reduction. Science **323**, 760–764 (2009). https://doi.org/10.1126/science.1168049
102. Strelko, V.V., Kartel, N.T., Dukhno, I.N., et al.: Mechanism of reductive oxygen adsorption on active carbons with various surface chemistry. Surf. Sci. **548**, 281–290 (2004). https://doi.org/10.1016/j.susc.2003.11.012
103. Jaouen, F., Lefèvre, M., Dodelet, J.P., et al.: Heat-treated Fe/N/C catalysts for O_2 electroreduction: are active sites hosted in micropores? J. Phys. Chem. B **110**, 5553–5558 (2006). https://doi.org/10.1021/jp057135h
104. Srivastava, D., Susi, T., Borghei, M., et al.: Dissociation of oxygen on pristine and nitrogen-doped carbon nanotubes: a spin-polarized density functional study. RSC Adv. **4**, 15225–15235 (2014). https://doi.org/10.1039/C3RA47784C
105. Wu, G., Santandreu, A., Kellogg, W., et al.: Carbon nanocomposite catalysts for oxygen reduction and evolution reactions: from nitrogen doping to transition-metal addition. Nano Energy **29**, 83–110 (2016). https://doi.org/10.1016/j.nanoen.2015.12.032
106. Artyushkova, K., Serov, A., Rojas-Carbonell, S., et al.: Chemistry of multitudinous active sites for oxygen reduction reaction in transition metal–nitrogen–carbon electrocatalysts. J. Phys. Chem. C **119**, 25917–25928 (2015). https://doi.org/10.1021/acs.jpcc.5b07653
107. Oh, H.S., Oh, J.G., Lee, W.H., et al.: The influence of the structural properties of carbon on the oxygen reduction reaction of nitrogen modified carbon based catalysts. Int. J. Hydrog. Energy **36**, 8181–8186 (2011). https://doi.org/10.1016/j.ijhydene.2011.04.139
108. Wang, Z.J., Jia, R.R., Zheng, J.F., et al.: Nitrogen-promoted self-assembly of N-doped carbon nanotubes and their intrinsic catalysis for oxygen reduction in fuel cells. ACS Nano **5**, 1677–1684 (2011). https://doi.org/10.1021/nn1030127
109. Chen, Z., Higgins, D., Tao, H.S., et al.: Highly active nitrogen-doped carbon nanotubes for oxygen reduction reaction in fuel cell applications. J. Phys. Chem. C **113**, 21008–21013 (2009). https://doi.org/10.1021/jp908067v
110. Jin, C., Nagaiah, T.C., Xia, W., et al.: Metal-free and electrocatalytically active nitrogen-doped carbon nanotubes synthesized by coating with polyaniline. Nanoscale **2**, 981–987 (2010). https://doi.org/10.1039/B9NR00405J
111. Ratso, S., Zitolo, A., Käärik, M., et al.: Non-precious metal cathodes for anion exchange membrane fuel cells from ball-milled iron and nitrogen doped carbide-derived carbons. Renew. Energy **167**, 800–810 (2021). https://doi.org/10.1016/j.renene.2020.11.154
112. Martinaiou, I., Monteverde Videla, A.H.A., Weidler, N., et al.: Activity and degradation study of an Fe-N-C catalyst for ORR in direct methanol fuel cell (DMFC). Appl. Catal. B-Environ. **262**, 118217 (2020). https://doi.org/10.1016/j.apcatb.2019.118217
113. Jain, D., Gustin, V., Basu, D., et al.: Phosphate tolerance of nitrogen-coordinated-iron-carbon (FeNC) catalysts for oxygen reduction reaction: a size-related hindrance effect. J. Catal. **390**, 150–160 (2020). https://doi.org/10.1016/j.jcat.2020.07.012
114. Wu, Y.J., Wang, Y.C., Wang, R.X., et al.: Three-dimensional networks of S-doped Fe/N/C with hierarchical porosity for efficient oxygen reduction in polymer electrolyte membrane fuel cells. ACS Appl. Mater. Interfaces **10**, 14602–14613 (2018). https://doi.org/10.1021/acsami.7b19332
115. Liu, J., Song, P., Ning, Z.G., et al.: Recent advances in heteroatom-doped metal-free electrocatalysts for highly efficient oxygen reduction reaction. Electrocatalysis **6**, 132–147 (2015). https://doi.org/10.1007/s12678-014-0243-9
116. Escobar, B., Martínez-Casillas, D.C., Pérez-Salcedo, K.Y., et al.: Research progress on biomass-derived carbon electrode materials for electrochemical energy storage and conversion technologies. Int. J. Hydrog. Energy **46**, 26053–26073 (2021). https://doi.org/10.1016/j.ijhydene.2021.02.017
117. Tabac, S., Eisenberg, D.: Pyrolyze this paper: can biomass become a source for precise carbon electrodes? Curr. Opin. Electrochem. **25**, 100638 (2021). https://doi.org/10.1016/j.coelec.2020.09.005
118. Matanovic, I., Artyushkova, K., Atanassov, P.: Understanding PGM-free catalysts by linking density functional theory calculations and structural analysis: perspectives and challenges. Curr. Opin. Electrochem. **9**, 137–144 (2018). https://doi.org/10.1016/j.coelec.2018.03.009
119. Li, Y.H., Liu, D.B., Gan, J., et al.: Sustainable and atomically dispersed iron electrocatalysts derived from nitrogen- and phosphorus-modified woody biomass for efficient oxygen reduction. Adv. Mater. Interfaces **6**, 1801623 (2019). https://doi.org/10.1002/admi.201801623
120. Wang, W., Jia, Q.Y., Mukerjee, S., et al.: Recent insights into the oxygen-reduction electrocatalysis of Fe/N/C materials. ACS Catal. **9**, 10126–10141 (2019). https://doi.org/10.1021/acscatal.9b02583
121. Zhang, S.M., Chen, M.H., Zhao, X., et al.: Advanced noncarbon materials as catalyst supports and non-noble electrocatalysts for fuel cells and metal–air batteries. Electrochem. Energy Rev. **4**, 336–381 (2021). https://doi.org/10.1007/s41918-020-00085-0
122. Zagal, J.H., Specchia, S., Atanassov, P.: Mapping transition metal-MN_4 macrocyclic complex catalysts performance for the critical reactivity descriptors. Curr. Opin. Electrochem. **27**, 100683 (2021). https://doi.org/10.1016/j.coelec.2020.100683
123. Specchia, S., Atanassov, P., Zagal, J.H.: Mapping transition metal–nitrogen–carbon catalystperformance on the critical descriptordiagram. Curr. Opin. Electrochem. **27**, 100687 (2021). https://doi.org/10.1016/j.coelec.2021.100687
124. Du, L., Shao, Y.Y., Sun, J.M., et al.: Electrocatalytic valorisation of biomass derived chemicals. Catal. Sci. Technol. **8**, 3216–3232 (2018). https://doi.org/10.1039/C8CY00533H
125. Lv, W.M., Wen, F.S., Xiang, J.Y., et al.: Peanut shell derived hard carbon as ultralong cycling anodes for lithium and sodium batteries. Electrochim. Acta **176**, 533–541 (2015). https://doi.org/10.1016/j.electacta.2015.07.059
126. Bar-On, Y.M., Phillips, R., Milo, R.: The biomass distribution on earth. Proc. Natl. Acad. Sci. U. S. A. **115**, 6506–6511 (2018). https://doi.org/10.1073/pnas.1711842115
127. Kalyani, P., Anitha, A.: Biomass carbon & its prospects in electrochemical energy systems. Int. J. Hydrog. Energy **38**, 4034–4045 (2013). https://doi.org/10.1016/j.ijhydene.2013.01.048
128. Zhang, L.X., Liu, Z.H., Cui, G.L., et al.: Biomass-derived materials for electrochemical energy storages. Prog. Polym. Sci. **43**, 136–164 (2015). https://doi.org/10.1016/j.progpolymsci.2014.09.003
129. Tang, W.J., Zhang, Y.F., Zhong, Y., et al.: Natural biomass-derived carbons for electrochemical energy storage. Mater. Res. Bull. **88**, 234–241 (2017). https://doi.org/10.1016/j.materresbull.2016.12.025
130. Gao, Z., Zhang, Y.Y., Song, N.N., et al.: Biomass-derived renewable carbon materials for electrochemical energy storage. Mater.

Res. Lett. **5**, 69–88 (2017). https://doi.org/10.1080/21663831.2016.1250834
131. Wang, J., Nie, P., Ding, B., et al.: Biomass derived carbon for energy storage devices. J. Mater. Chem. A **5**, 2411–2428 (2017). https://doi.org/10.1039/C6TA08742F
132. Yan, L.T., Yu, J.L., Houston, J., et al.: Biomass derived porous nitrogen doped carbon for electrochemical devices. Green Energy Environ. **2**, 84–99 (2017). https://doi.org/10.1016/j.gee.2017.03.002
133. Jiang, J., Zhu, J.H., Ai, W., et al.: Evolution of disposable bamboo chopsticks into uniform carbon fibers: a smart strategy to fabricate sustainable anodes for Li-ion batteries. Energy Environ. Sci. **7**, 2670–2679 (2014). https://doi.org/10.1039/C4EE00602J
134. Liu, M., Wang, L., Zhang, L., et al.: In-situ silica xerogel assisted facile synthesis of Fe-N-C catalysts with dense Fe-N_x active sites for efficient oxygen reduction. Small **18**, 2104934 (2022). https://doi.org/10.1002/smll.202104934
135. Graglia, M., Pampel, J., Hantke, T., et al.: Nitro lignin-derived nitrogen-doped carbon as an efficient and sustainable electrocatalyst for oxygen reduction. ACS Nano **10**, 4364–4371 (2016). https://doi.org/10.1021/acsnano.5b08040
136. Ma, Z.S., Zhang, H.Y., Yang, Z.Z., et al.: Mesoporous nitrogen-doped carbons with high nitrogen contents and ultrahigh surface areas: synthesis and applications in catalysis. Green Chem. **18**, 1976–1982 (2016). https://doi.org/10.1039/C5GC01920F
137. Klemm, D., Philipp, B., Heinze, T., et al.: Comprehensive Cellulose Chemistry: Fundamentals and Analytical Methods. Wiley, New York (1998). https://doi.org/10.1002/3527601929
138. Chen, H.Z.: Chemical composition and structure of natural lignocellulose. In: Biotechnology of Lignocellulose, pp. 25–71. Springer, Dordrecht (2014). https://link.springer.com/chapter/10.1007/978-94-007-6898-7_2
139. Wang, B., Yang, W., McKittrick, J., et al.: Keratin: structure, mechanical properties, occurrence in biological organisms, and efforts at bioinspiration. Prog. Mater. Sci. **76**, 229–318 (2016). https://doi.org/10.1016/j.pmatsci.2015.06.001
140. Habibi, Y., Lucia, L.A., Rojas, O.J.: Cellulose nanocrystals: chemistry, self-assembly, and applications. Chem. Rev. **110**, 3479–3500 (2010). https://doi.org/10.1021/cr900339w
141. Shen, S.H., Zhou, R.F., Li, Y.H., et al.: Bacterium, fungus, and virus microorganisms for energy storage and conversion. Small Methods **3**, 1900596 (2019). https://doi.org/10.1002/smtd.201900596
142. Wu, Z.Y., Liang, H.W., Chen, L.F., et al.: Bacterial cellulose: a robust platform for design of three dimensional carbon-based functional nanomaterials. Acc. Chem. Res. **49**, 96–105 (2016). https://doi.org/10.1021/acs.accounts.5b00380
143. Ago, M., Tardy, B.L., Wang, L., et al.: Supramolecular assemblies of lignin into nano- and microparticles. MRS Bull. **42**, 371–378 (2017). https://doi.org/10.1557/mrs.2017.88
144. Herburger, K., Franková, L., Pičmanová, M., et al.: Hetero-trans-β-glucanase produces cellulose–xyloglucan covalent bonds in the cell walls of structural plant tissues and is stimulated by expansin. Mol. Plant. **13**, 1047–1062 (2020). https://doi.org/10.1016/j.molp.2020.04.011
145. Ayoub, A., Venditti, R.A., Pawlak, J.J., et al.: Development of an acetylation reaction of switchgrass hemicellulose in ionic liquid without catalyst. Ind. Crop. Prod. **44**, 306–314 (2013). https://doi.org/10.1016/j.indcrop.2012.10.036
146. Mugwagwa, L.R., Chimphango, A.F.A.: Optimising wheat straw alkali-organosolv pre-treatment to enhance hemicellulose modification and compatibility with reinforcing fillers. Int. J. Biol. Macromol. **143**, 862–872 (2020). https://doi.org/10.1016/j.ijbiomac.2019.09.147
147. Chadni, M., Grimi, N., Bals, O., et al.: Elaboration of hemicellulose-based films: impact of the extraction process from spruce wood on the film properties. Carbohydr. Res. **497**, 108111 (2020). https://doi.org/10.1016/j.carres.2020.108111
148. Cairns, A.J., Begley, P., Sims, I.M.: The structure of starch from seeds and leaves of the fructan-accumulating ryegrass *Lolium temulentum* L. J. Plant Physiol. **159**, 221–230 (2002). https://doi.org/10.1078/0176-1617-00685
149. Dutta, P.K., Dutta, J., Tripathi, V.S.: Chitin and chitosan: properties and applications. J. Sci. Ind. Res. **63**, 20–31 (2004). https://doi.org/10.1016/j.progpolymsci.2006.06.001
150. Pillai, C.K.S., Paul, W., Sharma, C.P.: Chitin and chitosan polymers: chemistry, solubility and fiber formation. Prog. Polym. Sci. **34**, 641–678 (2009). https://doi.org/10.1016/j.progpolymsci.2009.04.001
151. Kaushik, A., Singh, M., Verma, G.: Green nanocomposites based on thermoplastic starch and steam exploded cellulose nanofibrils from wheat straw. Carbohydr. Polym. **82**, 337–345 (2010). https://doi.org/10.1016/j.carbpol.2010.04.063
152. Bilgili, F., Koçak, E., Kuşkaya, S., et al.: Estimation of the co-movements between biofuel production and food prices: a wavelet-based analysis. Energy **213**, 118777 (2020). https://doi.org/10.1016/j.energy.2020.118777
153. Yukesh Kannah, R., Merrylin, J., Poornima Devi, T., et al.: Food waste valorization: biofuels and value added product recovery. Bioresour. Technol. Rep. **11**, 100524 (2020). https://doi.org/10.1016/j.biteb.2020.100524
154. Lazaro, L.L.B., Giatti, L.L., Bermann, C., et al.: Policy and governance dynamics in the water-energy-food-land nexus of biofuels: proposing a qualitative analysis model. Renew. Sustain. Energy Rev. **149**, 111384 (2021). https://doi.org/10.1016/j.rser.2021.111384
155. Subramaniam, Y., Masron, T.A., Azman, N.H.N.: Biofuels, environmental sustainability, and food security: a review of 51 countries. Energy Res. Soc. Sci. **68**, 101549 (2020). https://doi.org/10.1016/j.erss.2020.101549
156. Abdali, H., Sahebi, H., Pishvaee, M.: The water-energy-food-land nexus at the sugarcane-to-bioenergy supply chain: a sustainable network design model. Comput. Chem. Eng. **145**, 107199 (2021). https://doi.org/10.1016/j.compchemeng.2020.107199
157. You, C., Han, S., Kim, J.: Integrative design of the optimal biorefinery and bioethanol supply chain under the water-energy-food-land (WEFL) nexus framework. Energy **228**, 120574 (2021). https://doi.org/10.1016/j.energy.2021.120574
158. Esfahani, R.A.M., Osmieri, L., Specchia, S., et al.: H_2-rich syngas production through mixed residual biomass and HDPE waste via integrated catalytic gasification and tar cracking plus bio-char upgrading. Chem. Eng. J. **308**, 578–587 (2017). https://doi.org/10.1016/j.cej.2016.09.049
159. Ansari, K.B., Hassan, S.Z., Bhoi, R., et al.: Co-pyrolysis of biomass and plastic wastes: a review on reactants synergy, catalyst impact, process parameter, hydrocarbon fuel potential, COVID-19. J. Environ. Chem. Eng. **9**, 106436 (2021). https://doi.org/10.1016/j.jece.2021.106436
160. Muhyuddin, M., Mustarelli, P., Santoro, C.: Recent advances in waste plastic transformation into valuable platinum-group metal-free electrocatalysts for oxygen reduction reaction. Chemsuschem **14**, 3785–3800 (2021). https://doi.org/10.1002/cssc.202101252
161. Muhyuddin, M., Filippi, J., Zoia, L., et al.: Waste face surgical mask transformation into crude oil and nanostructured electrocatalysts for fuel cells and electrolyzers. Chemsuschem **15**, e202102351 (2022). https://doi.org/10.1002/cssc.202102351
162. Dharmaraj, S., Ashokkumar, V., Pandiyan, R., et al.: Pyrolysis: an effective technique for degradation of COVID-19 medical wastes. Chemosphere **275**, 130092 (2021). https://doi.org/10.1016/j.chemosphere.2021.130092
163. Bazargan, A., Yan, Y., Hui, C.W., et al.: A review: synthesis of carbon-based nano and micro materials by high temperature and

high pressure. Ind. Eng. Chem. Res. **52**, 12689–12702 (2013). https://doi.org/10.1021/ie4018513
164. Titirici, M.M., White, R.J., Falco, C., et al.: Black perspectives for a green future: hydrothermal carbons for environment protection and energy storage. Energy Environ. Sci. **5**, 6796–6822 (2012). https://doi.org/10.1039/C2EE21166A
165. Zhang, P.F., Gong, Y.T., Wei, Z.Z., et al.: Updating biomass into functional carbon material in ionothermal manner. ACS Appl. Mater. Interfaces **6**, 12515–12522 (2014). https://doi.org/10.1021/am5023682
166. Pereira, R.G., Veloso, C.M., da Silva, N.M., et al.: Preparation of activated carbons from cocoa shells and siriguela seeds using H_3PO_4 and $ZnCL_2$ as activating agents for BSA and α-lactalbumin adsorption. Fuel Process. Technol. **126**, 476–486 (2014). https://doi.org/10.1016/j.fuproc.2014.06.001
167. Mi, J., Wang, X.R., Fan, R.J., et al.: Coconut-shell-based porous carbons with a tunable micro/mesopore ratio for high-performance supercapacitors. Energy Fuels **26**, 5321–5329 (2012). https://doi.org/10.1021/ef3009234
168. Yang, M.L., Guo, L.P., Hu, G.S., et al.: Highly cost-effective nitrogen-doped porous coconut shell-based CO_2 sorbent synthesized by combining ammoxidation with KOH activation. Environ. Sci. Technol. **49**, 7063–7070 (2015). https://doi.org/10.1021/acs.est.5b01311
169. Sekhon, S.S., Kaur, P., Park, J.S.: From coconut shell biomass to oxygen reduction reaction catalyst: tuning porosity and nitrogen doping. Renew. Sustain. Energy Rev. **147**, 111173 (2021). https://doi.org/10.1016/j.rser.2021.111173
170. Kuo, H.C., Lin, Y.G., Chiang, C.L., et al.: Email protected graphitic biochars derived from hydrothermal-microwave pyrolysis of cellulose biomass for fuel cell catalysts. J. Anal. Appl. Pyrolysis **153**, 104991 (2021). https://doi.org/10.1016/j.jaap.2020.104991
171. Chen, Y.S., Yang, B., Xie, W.Y., et al.: Combined soft templating with thermal exfoliation toward synthesis of porous g-C_3N_4 nanosheets for improved photocatalytic hydrogen evolution. J. Mater. Res. Technol. **13**, 301–310 (2021). https://doi.org/10.1016/j.jmrt.2021.04.056
172. Shen, W.Z., Fan, W.B.: Nitrogen-containing porous carbons: synthesis and application. J. Mater. Chem. A **1**, 999–1013 (2013). https://doi.org/10.1039/c2ta00028h
173. Kabir, S., Serov, A., Atanassov, P.: 3D-graphene supports for palladium nanoparticles: effect of micro/macropores on oxygen electroreduction in anion exchange membrane fuel cells. J. Power Sources **375**, 255–264 (2018). https://doi.org/10.1016/j.jpowsour.2017.08.092
174. Monteverde Videla, A.H.A., Osmieri, L., Specchia, S.: Non-noble metal (NNM) catalysts for fuel cells: tuning the activity by a rational step-by-step single variable evolution. In: Zagal, J.H., Bedioui, F. (eds) Electrochemistry of N4 macrocyclic metal complexes, pp. 69–101. Springer, Cham (2016). https://doi.org/10.1007/978-3-319-31172-2_3
175. Osmieri, L., Escudero-Cid, R., Monteverde Videla, A.H.A., et al.: Performance of a Fe-N-C catalyst for the oxygen reduction reaction in direct methanol fuel cell: cathode formulation optimization and short-term durability. Appl. Catal. B-Environ. **201**, 253–265 (2017). https://doi.org/10.1016/j.apcatb.2016.08.043
176. Tylus, U., Jia, Q.Y., Strickland, K., et al.: Elucidating oxygen reduction active sites in pyrolyzed metal–nitrogen coordinated non-precious-metal electrocatalyst systems. J. Phys. Chem. C **118**, 8999–9008 (2014). https://doi.org/10.1021/jp500781v
177. Ma, J.J., Li, J.S., Wang, R.G., et al.: Hierarchical porous S-doped Fe–N–C electrocatalyst for high-power-density zinc–air battery. Mater. Today Energy **19**, 100624 (2021). https://doi.org/10.1016/j.mtener.2020.100624
178. Lo Vecchio, C., Sebastián, D., Alegre, C., et al.: Carbon-supported Pd and Pd-Co cathode catalysts for direct methanol fuel cells (DMFCs) operating with high methanol concentration. J. Electroanal. Chem. **808**, 464–473 (2018). https://doi.org/10.1016/j.jelechem.2017.02.042
179. Li, C.J., Yang, W.H., He, W., et al.: Multifunctional surfactants for synthesizing high-performance energy storage materials. Energy Storage Mater. **43**, 1–19 (2021). https://doi.org/10.1016/j.ensm.2021.08.033
180. Díez, N., Sevilla, M., Fuertes, A.B.: Dense (non-hollow) carbon nanospheres: synthesis and electrochemical energy applications. Mater. Today Nano **16**, 100147 (2021). https://doi.org/10.1016/j.mtnano.2021.100147
181. Momčilović, M., Stojmenović, M., Gavrilov, N., et al.: Complex electrochemical investigation of ordered mesoporous carbon synthesized by soft-templating method: charge storage and electrocatalytical or Pt-electrocatalyst supporting behavior. Electrochim. Acta **125**, 606–614 (2014). https://doi.org/10.1016/j.electacta.2014.01.152
182. Qiu, Z.Y., Huang, N.B., Zhang, J.J., et al.: Fabricating carbon nanocages as ORR catalysts in alkaline electrolyte from F127 self-assemble core-shell micelle. Int. J. Hydrog. Energy **44**, 32184–32191 (2019). https://doi.org/10.1016/j.ijhydene.2019.10.066
183. Braghiroli, F.L., Fierro, V., Szczurek, A., et al.: Hydrothermally treated aminated tannin as precursor of N-doped carbon gels for supercapacitors. Carbon **90**, 63–74 (2015). https://doi.org/10.1016/j.carbon.2015.03.038
184. Grishechko, L.I., Amaral-Labat, G., Szczurek, A., et al.: Lignin–phenol–formaldehyde aerogels and cryogels. Microporous Mesoporous Mat. **168**, 19–29 (2013). https://doi.org/10.1016/j.micromeso.2012.09.024
185. Morawa Eblagon, K., Rey-Raap, N., Figueiredo, J.L., et al.: Relationships between texture, surface chemistry and performance of N-doped carbon xerogels in the oxygen reduction reaction. Appl. Surf. Sci. **548**, 149242 (2021). https://doi.org/10.1016/j.apsusc.2021.149242
186. Alegre, C., Sebastián, D., Lázaro, M.J.: Carbon xerogels electrochemical oxidation and correlation with their physico-chemical properties. Carbon **144**, 382–394 (2019). https://doi.org/10.1016/j.carbon.2018.12.065
187. Zainul Abidin, A.F., Loh, K.S., Wong, W.Y., et al.: Nitrogen-doped carbon xerogels catalyst for oxygen reduction reaction: improved structural and catalytic activity by enhancing nitrogen species and cobalt insertion. Int. J. Hydrog. Energy **44**, 28789–28802 (2019). https://doi.org/10.1016/j.ijhydene.2019.09.066
188. Deng, J., Li, M.M., Wang, Y.: Biomass-derived carbon: synthesis and applications in energy storage and conversion. Green Chem. **18**, 4824–4854 (2016). https://doi.org/10.1039/C6GC01172A
189. Kim, M.J., Park, J.E., Kim, S., et al.: Biomass-derived air cathode materials: pore-controlled S, N-co-doped carbon for fuel cells and metal–air batteries. ACS Catal. **9**, 3389–3398 (2019). https://doi.org/10.1021/acscatal.8b03730
190. Qiu, Y.X., Wanyan, Q.R., Xie, W.Y., et al.: Green and biomass-derived materials with controllable shape memory transition temperatures based on cross-linked poly (l-malic acid). Polymer **180**, 121733 (2019). https://doi.org/10.1016/j.polymer.2019.121733
191. Chung, H., Wu, G., Higgins, D., et al.: Heat-treated non-precious metal catalysts for oxygen reduction. In: Zagal, J.H., Bedioui, F. (eds) Electrochemistry of N4 Macrocyclic Metal Complexes, pp. 41–68. Springer, Cham (2016). https://doi.org/10.1007/978-3-319-31172-2_2
192. Borghei, M., Laocharoen, N., Kibena-Põldsepp, E., et al.: Porous N, P-doped carbon from coconut shells with high electrocatalytic activity for oxygen reduction: alternative to Pt-C for alkaline fuel cells. Appl. Catal. B-Environ. **204**, 394–402 (2017). https://doi.org/10.1016/j.apcatb.2016.11.029
193. Yang, K.B., Peng, J.H., Srinivasakannan, C., et al.: Preparation of high surface area activated carbon from coconut shells using

microwave heating. Bioresour. Technol. **101**, 6163–6169 (2010). https://doi.org/10.1016/j.biortech.2010.03.001
194. Gao, S.Y., Fan, H., Zhang, S.X.: Nitrogen-enriched carbon from bamboo fungus with superior oxygen reduction reaction activity. J. Mater. Chem. A **2**, 18263–18270 (2014). https://doi.org/10.1039/c4ta03558e
195. Wu, D.Y., Shi, Y.T., Jing, H.Y., et al.: Tea-leaf-residual derived electrocatalyst: hierarchical pore structure and self nitrogen and fluorine co-doping for efficient oxygen reduction reaction. Int. J. Hydrog. Energy **43**, 19492–19499 (2018). https://doi.org/10.1016/j.ijhydene.2018.08.201
196. Guo, Z.Y., Xiao, Z., Ren, G.Y., et al.: Natural tea-leaf-derived, ternary-doped 3D porous carbon as a high-performance electrocatalyst for the oxygen reduction reaction. Nano Res. **9**, 1244–1255 (2016). https://doi.org/10.1007/s12274-016-1020-2
197. Hao, Y.J., Zhang, X., Yang, Q.F., et al.: Highly porous defective carbons derived from seaweed biomass as efficient electrocatalysts for oxygen reduction in both alkaline and acidic media. Carbon **137**, 93–103 (2018). https://doi.org/10.1016/j.carbon.2018.05.007
198. Zhou, H., Zhang, J., Zhu, J.W., et al.: A self-template and KOH activation co-coupling strategy to synthesize ultrahigh surface area nitrogen-doped porous graphene for oxygen reduction. RSC Adv. **6**, 73292–73300 (2016). https://doi.org/10.1039/C6RA16703A
199. Zhou, H., Zhang, J., Amiinu, I.S., et al.: Transforming waste biomass with an intrinsically porous network structure into porous nitrogen-doped graphene for highly efficient oxygen reduction. Phys. Chem. Chem. Phys. **18**, 10392–10399 (2016). https://doi.org/10.1039/c6cp00174b
200. Liu, Y., Su, M.J., Li, D.H., et al.: Soybean straw biomass-derived Fe–N co-doped porous carbon as an efficient electrocatalyst for oxygen reduction in both alkaline and acidic media. RSC Adv. **10**, 6763–6771 (2020). https://doi.org/10.1039/c9ra07539a
201. Srinu, A., Peera, S.G., Parthiban, V., et al.: Heteroatom engineering and co-doping of N and P to porous carbon derived from spent coffee grounds as an efficient electrocatalyst for oxygen reduction reactions in alkaline medium. ChemistrySelect **3**, 690–702 (2018). https://doi.org/10.1002/slct.201702042
202. Zhang, J., Zhang, C.Y., Zhao, Y.F., et al.: Three dimensional few-layer porous carbon nanosheets towards oxygen reduction. Appl. Catal. B-Environ. **211**, 148–156 (2017). https://doi.org/10.1016/j.apcatb.2017.04.038
203. Pérez-Rodríguez, S., Sebastián, D., Alegre, C., et al.: Biomass waste-derived nitrogen and iron co-doped nanoporous carbons as electrocatalysts for the oxygen reduction reaction. Electrochim. Acta **387**, 138490 (2021). https://doi.org/10.1016/j.electacta.2021.138490
204. Gao, S.Y., Wei, X.J., Fan, H., et al.: Nitrogen-doped carbon shell structure derived from natural leaves as a potential catalyst for oxygen reduction reaction. Nano Energy **13**, 518–526 (2015). https://doi.org/10.1016/j.nanoen.2015.02.031
205. Li, M., Xiong, Y.P., Liu, X.T., et al.: Iron and nitrogen co-doped carbon nanotube@hollow carbon fibers derived from plant biomass as efficient catalysts for the oxygen reduction reaction. J. Mater. Chem. A **3**, 9658–9667 (2015). https://doi.org/10.1039/c5ta00958h
206. Yang, S., Mao, X., Cao, Z., Yin, Y., Wang, Z., Shi, M., Dong, H.: Onion-derived N, S self-doped carbon materials as highly efficient metal-free electrocatalysts for the oxygen reduction reaction. Appl. Surf. Sci. **427**, 626–634 (2018). https://doi.org/10.1016/j.apsusc.2017.08.222
207. Wang, G.H., Peng, H.L., Qiao, X.C., et al.: Biomass-derived porous heteroatom-doped carbon spheres as a high-performance catalyst for the oxygen reduction reaction. Int. J. Hydrog. Energy **41**, 14101–14110 (2016). https://doi.org/10.1016/j.ijhydene.2016.06.023
208. Zhang, J.M., He, J., Zheng, H.Y., et al.: N, S dual-doped carbon nanosheet networks with hierarchical porosity derived from biomass of *Allium cepa* as efficient catalysts for oxygen reduction and Zn–air batteries. J. Mater. Sci. **55**, 7464–7476 (2020). https://doi.org/10.1007/s10853-020-04535-4
209. Zheng, H.Y., Zhang, Y., Long, J.L., et al.: Nitrogen-doped porous carbon material derived from biomass of beancurd as an efficient electrocatalyst for oxygen reduction and Zn-air fuel cell. J. Electrochem. Soc. **167**, 084516 (2020). https://doi.org/10.1149/1945-7111/ab907f
210. Ferrero, G.A., Preuss, K., Marinovic, A., et al.: Fe–N-doped carbon capsules with outstanding electrochemical performance and stability for the oxygen reduction reaction in both acid and alkaline conditions. ACS Nano **10**, 5922–5932 (2016). https://doi.org/10.1021/acsnano.6b01247
211. Sudarsono, W., Wong, W.Y., Loh, K.S., et al.: Noble-free oxygen reduction reaction catalyst supported on Sengon wood (*Paraserianthes falcataria L.*) derived reduced graphene oxide for fuel cell application. Int. J. Energy Res. **44**, 1761–1774 (2020). https://doi.org/10.1002/er.5015
212. Guo, C.Z., Liao, W.L., Li, Z.B., et al.: Easy conversion of protein-rich enoki mushroom biomass to a nitrogen-doped carbon nanomaterial as a promising metal-free catalyst for oxygen reduction reaction. Nanoscale **7**, 15990–15998 (2015). https://doi.org/10.1039/c5nr03828f
213. Zhang, H.M., Wang, Y., Wang, D., et al.: Hydrothermal transformation of dried grass into graphitic carbon-based high performance electrocatalyst for oxygen reduction reaction. Small **10**, 3371–3378 (2014). https://doi.org/10.1002/smll.201400781
214. Xiao, Z., Gao, X.Y., Shi, M.H., et al.: China rose-derived tri-heteroatom co-doped porous carbon as an efficient electrocatalysts for oxygen reduction reaction. RSC Adv. **6**, 86401–86409 (2016). https://doi.org/10.1039/c6ra14619h
215. Chen, P., Wang, L.K., Wang, G., et al.: Nitrogen-doped nanoporous carbon nanosheets derived from plant biomass: an efficient catalyst for oxygen reduction reaction. Energy Environ. Sci. **7**, 4095–4103 (2014). https://doi.org/10.1039/c4ee02531h
216. Liu, Z.W., Wang, F., Li, M., et al.: N, S and P-ternary doped carbon nano-pore/tube composites derived from natural chemicals in waste sweet osmanthus fruit with superior activity for oxygen reduction in acidic and alkaline media. RSC Adv. **6**, 37500–37505 (2016). https://doi.org/10.1039/c6ra08371d
217. Kong, D.W., Yuan, W.J., Li, C., et al.: Synergistic effect of nitrogen-doped hierarchical porous carbon/graphene with enhanced catalytic performance for oxygen reduction reaction. Appl. Surf. Sci. **393**, 144–150 (2017). https://doi.org/10.1016/j.apsusc.2016.10.019
218. Yuan, W.J., Xie, A.J., Li, S.K., et al.: High-activity oxygen reduction catalyst based on low-cost bagasse, nitrogen and large specific surface area. Energy **115**, 397–403 (2016). https://doi.org/10.1016/j.energy.2016.09.026
219. Zhao, Q.P., Ma, Q., Pan, F.P., et al.: Facile synthesis of nitrogen-doped carbon nanosheets as metal-free catalyst with excellent oxygen reduction performance in alkaline and acidic media. J. Solid State Electrochem. **20**, 1469–1479 (2016). https://doi.org/10.1007/s10008-016-3157-z
220. Muhyuddin, M., Zocche, N., Lorenzi, R., et al.: Valorization of the inedible pistachio shells into nanoscale transition metal and nitrogen codoped carbon-based electrocatalysts for hydrogen evolution reaction and oxygen reduction reaction. Mater. Renew. Sustain. Energy **11**, 131–141 (2022). https://doi.org/10.1007/s40243-022-00212-5
221. Zago, S., Bartoli, M., Muhyuddin, M., et al.: Engineered biochar derived from pyrolyzed waste tea as a carbon support for Fe-N-C electrocatalysts for the oxygen reduction reaction. Electrochim.

Acta **412**, 140128 (2022). https://doi.org/10.1016/j.electacta.2022.140128
222. Ahsan, M.A., Puente Santiago, A.R., Rodriguez, A., et al.: Biomass-derived ultrathin carbon-shell coated iron nanoparticles as high-performance tri-functional HER, ORR and Fenton-like catalysts. J. Clean. Prod. **275**, 124141 (2020). https://doi.org/10.1016/j.jclepro.2020.124141
223. Jiang, R., Chen, X., Liu, W.P., et al.: Atomic Zn sites on N and S codoped biomass-derived graphene for a high-efficiency oxygen reduction reaction in both acidic and alkaline electrolytes. ACS Appl. Energy Mater. **4**, 2481–2488 (2021). https://doi.org/10.1021/acsaem.0c03035
224. Müller-Hülstede, J., Schonvogel, D., Schmies, H., et al.: Incorporation of activated biomasses in Fe-N-C catalysts for oxygen reduction reaction with enhanced stability in acidic media. ACS Appl. Energy Mater. **4**, 6912–6922 (2021). https://doi.org/10.1021/acsaem.1c01018
225. Yao, W.T., Yu, L., Yao, P.F., et al.: Bulk production of nonprecious metal catalysts from cheap starch as precursor and their excellent electrochemical activity. ACS Sustain. Chem. Eng. **4**, 3235–3244 (2016). https://doi.org/10.1021/acssuschemeng.6b00269
226. Ou, Z.H., Qin, Y., Xu, C.L., et al.: Double-activator modulation of ultrahigh surface areas on doped carbon catalysts boosts the primary Zn–air battery performance. ACS Appl. Energy Mater. **5**, 1701–1709 (2022). https://doi.org/10.1021/acsaem.1c03142
227. Ma, J.H., Yao, Z.Z., Hoang, T.K.A., et al.: The intriguing ORR performance of iron and nitrogen co-doped biomass carbon composites incorporating surface-modified polyaniline-derived carbon. Fuel **317**, 123496 (2022). https://doi.org/10.1016/j.fuel.2022.123496
228. Park, J.H., Kaur, P., Park, J.S., et al.: Soil-templated synthesis of mesoporous carbons from biomass wastes for ORR catalysis. Catal. Today **403**, 2–10 (2022). https://doi.org/10.1016/j.cattod.2022.08.011
229. Zhao, Y.L., Liu, X.P., Liu, Y., et al.: Favorable pore size distribution of biomass-derived N, S dual-doped carbon materials for advanced oxygen reduction reaction. Int. J. Hydrog. Energy **47**, 12964–12974 (2022). https://doi.org/10.1016/j.ijhydene.2022.02.064
230. Amiinu, I.S., Zhang, J., Kou, Z.K., et al.: Self-organized 3D porous graphene dual-doped with biomass-sponsored nitrogen and sulfur for oxygen reduction and evolution. ACS Appl. Mater. Interfaces **8**, 29408–29418 (2016). https://doi.org/10.1021/acsami.6b08719
231. Zan, Y.X., Zhang, Z.P., Liu, H.J., et al.: Nitrogen and phosphorus co-doped hierarchically porous carbons derived from cattle bones as efficient metal-free electrocatalysts for the oxygen reduction reaction. J. Mater. Chem. A **5**, 24329–24334 (2017). https://doi.org/10.1039/c7ta07746g
232. Guo, C.Z., Hu, R., Liao, W.L., et al.: Protein-enriched fish "biowaste" converted to three-dimensional porous carbon nano-network for advanced oxygen reduction electrocatalysis. Electrochim. Acta **236**, 228–238 (2017). https://doi.org/10.1016/j.electacta.2017.03.169
233. Zheng, F.Y., Li, R.S., Ge, S.Y., et al.: Nitrogen and phosphorus co-doped carbon networks derived from shrimp shells as an efficient oxygen reduction catalyst for microbial fuel cells. J. Power Sources **446**, 227356 (2020). https://doi.org/10.1016/j.jpowsour.2019.227356
234. Shi, C.J., Maimaitiyiming, X.: Biomass-derived precious metal-free porous carbon: Ca-N, P-doped carbon materials and its electrocatalytic properties. J. Alloy. Compd. **883**, 160726 (2021). https://doi.org/10.1016/j.jallcom.2021.160726
235. Liang, H.W., Wu, Z.Y., Chen, L.F., et al.: Bacterial cellulose derived nitrogen-doped carbon nanofiber aerogel: an efficient metal-free oxygen reduction electrocatalyst for zinc-air battery. Nano Energy **11**, 366–376 (2015). https://doi.org/10.1016/j.nanoen.2014.11.008
236. Liu, Q., Duan, Y.X., Zhao, Q.P., et al.: Direct synthesis of nitrogen-doped carbon nanosheets with high surface area and excellent oxygen reduction performance. Langmuir **30**, 8238–8245 (2014). https://doi.org/10.1021/la404995y
237. Alonso-Lemus, I.L., Figueroa-Torres, M.Z., Lardizabal-Gutíerrez, D., et al.: Converting chicken manure into highly active N-P co-doped metal-free biocarbon electrocatalysts: effect of chemical treatment on their catalytic activity for the ORR. Sustain. Energ. Fuels **3**, 1307–1316 (2019). https://doi.org/10.1039/c8se00583d
238. Lee, J., Sohn, Y., Kim, S., et al.: Insight on the treatment of pig blood as biomass derived electrocatalyst precursor for high performance in the oxygen reduction reaction. Appl. Surf. Sci. **545**, 148940 (2021). https://doi.org/10.1016/j.apsusc.2021.148940
239. Chaudhari, K.N., Song, M.Y., Yu, J.S.: Transforming hair into heteroatom-doped carbon with high surface area. Small **10**, 2625–2636 (2014). https://doi.org/10.1002/smll.201303831
240. Chaudhari, N.K., Song, M.Y., Yu, J.S.: Heteroatom-doped highly porous carbon from human urine. Sci. Rep. **4**, 1–10 (2014). https://doi.org/10.1038/srep05221
241. Wang, X.D., Fang, J.J., Liu, X.R., et al.: Converting biomass into efficient oxygen reduction reaction catalysts for proton exchange membrane fuel cells. Sci. China Mater. **63**, 524–532 (2020). https://doi.org/10.1007/s40843-019-1224-5
242. Jäger, R., Teppor, P., Paalo, M., et al.: Synthesis and characterization of cobalt and nitrogen co-doped peat-derived carbon catalysts for oxygen reduction in acidic media. Catalysts **11**, 715 (2021). https://doi.org/10.3390/catal11060715
243. Maruyama, J., Hasegawa, T., Amano, T., et al.: Pore development in carbonized hemoglobin by concurrently generated MgO template for activity enhancement as fuel cell cathode catalyst. ACS Appl. Mater. Interfaces **3**, 4837–4843 (2011). https://doi.org/10.1021/am2013294
244. Sarkar, I.J.R., Peera, S.G., Chetty, R.: Fe–N–C catalyst derived from solid-state coordination complex as durable oxygen reduction electrocatalyst in alkaline electrolyte. Ionics **26**, 5685–5696 (2020). https://doi.org/10.1007/s11581-020-03722-2
245. Juvanen, S., Sarapuu, A., Mooste, M., et al.: Electroreduction of oxygen on iron- and cobalt-containing nitrogen-doped carbon catalysts prepared from the rapeseed press cake. J. Electroanal. Chem. **920**, 116599 (2022). https://doi.org/10.1016/j.jelechem.2022.116599
246. Zhao, S.Y., Liu, T., Wang, J., et al.: Anti-CO_2 strategies for extending zinc-air batteries' lifetime: a review. Chem. Eng. J. **450**, 138207 (2022). https://doi.org/10.1016/j.cej.2022.138207
247. Miao, W.J., Liu, W.F., Ding, Y.C., et al.: Cobalt (iron), nitrogen and carbon doped mushroom biochar for high-efficiency oxygen reduction in microbial fuel cell and Zn-air battery. J. Environ. Chem. Eng. **10**, 108474 (2022). https://doi.org/10.1016/j.jece.2022.108474
248. Wang, Y., Sheng, K., Xu, R., et al.: Efficient bifunctional 3D porous Co–N–C catalyst from spent Li-ion batteries and biomass for zinc-air batteries. Chem. Eng. Sci. **268**, 118433 (2023). https://doi.org/10.1016/j.ces.2022.118433
249. Su, D.C., Wang, X.Z., Liu, Y.L., et al.: Co-embedded nitrogen-enriching biomass-derived porous carbon for highly efficient oxygen reduction and flexible zinc-air battery. J. Alloy. Compd. **896**, 162604 (2022). https://doi.org/10.1016/j.jallcom.2021.162604
250. Jiao, D., Ma, Z.A., Li, J.S., et al.: Test factors affecting the performance of zinc–air battery. J. Energy Chem. **44**, 1–7 (2020). https://doi.org/10.1016/j.jechem.2019.09.008

251. Monteverde Videla, A.H.A., Sebastián, D., Vasile, N.S., et al.: Performance analysis of Fe–N–C catalyst for DMFC cathodes: effect of water saturation in the cathodic catalyst layer. Int. J. Hydrog. Energy **41**, 22605–22618 (2016). https://doi.org/10.1016/j.ijhydene.2016.06.060
252. Zelenay, P., Myers, D.: ElectroCat2.0, DOE hydrogen program 2021 Annual Merit Review and Peer Evaluation Meeting, 7–11 June (2021)
253. Akula, S., Mooste, M., Zulevi, B., et al.: Mesoporous textured Fe-N-C electrocatalysts as highly efficient cathodes for proton exchange membrane fuel cells. J. Power Sources **520**, 230819 (2022). https://doi.org/10.1016/j.jpowsour.2021.230819
254. Li, J.K., Brüller, S., Sabarirajan, D.C., et al.: Designing the 3D architecture of PGM-free cathodes for H_2/air proton exchange membrane fuel cells. ACS Appl. Energy Mater. **2**, 7211–7222 (2019). https://doi.org/10.1021/acsaem.9b01181
255. Santori, P.G., Speck, F.D., Cherevko, S., et al.: High performance FeNC and Mn-oxide/FeNC layers for AEMFC cathodes. J. Electrochem. Soc. **167**, 134505 (2020). https://doi.org/10.1149/1945-7111/abb7e0
256. Lilloja, J., Kibena-Põldsepp, E., Sarapuu, A., et al.: Transition metal and nitrogen-doped carbide-derived carbon/carbon nanotube composites as cathode catalysts for anion-exchange membrane fuel cells. Meet. Abstr. (2021). https://doi.org/10.1149/ma2021-02401213mtgabs
257. Adabi, H., Shakouri, A., Ul Hassan, N., et al.: High-performing commercial Fe–N–C cathode electrocatalyst for anion-exchange membrane fuel cells. Nat. Energy **6**, 834–843 (2021). https://doi.org/10.1038/s41560-021-00878-7
258. Kisand, K., Sarapuu, A., Danilian, D., et al.: Transition metal-containing nitrogen-doped nanocarbon catalysts derived from 5-methylresorcinol for anion exchange membrane fuel cell application. J. Colloid Interface Sci. **584**, 263–274 (2021). https://doi.org/10.1016/j.jcis.2020.09.114
259. Pajarito Powder. https://pajaritopowder.com/products/
260. Brouzgou, A., Song, S.Q., Tsiakaras, P.: Low and non-platinum electrocatalysts for PEMFCs: current status, challenges and prospects. Appl. Catal. B-Environ. **127**, 371–388 (2012). https://doi.org/10.1016/j.apcatb.2012.08.031
261. Daems, N., Sheng, X., Vankelecom, I.F.J., et al.: Metal-free doped carbon materials as electrocatalysts for the oxygen reduction reaction. J. Mater. Chem. A **2**, 4085–4110 (2014). https://doi.org/10.1039/c3ta14043a
262. Mineva, T., Matanovic, I., Atanassov, P., et al.: Understanding active sites in pyrolyzed Fe-N-C catalysts for fuel cell cathodes by bridging density functional theory calculations and ^{57}Fe Mössbauer spectroscopy. ACS Catal. **9**, 9359–93714 (2019). https://doi.org/10.1021/acscatal.9b02586
263. Workman, M.J., Serov, A., Tsui, L.K., et al.: Fe–N–C catalyst graphitic layer structure and fuel cell performance. ACS Energy Lett. **2**, 1489–1493 (2017). https://doi.org/10.1021/acsenergylett.7b00391
264. Kramm, U.I., Lefèvre, M., Larouche, N., et al.: Correlations between mass activity and physicochemical properties of Fe/N/C catalysts for the ORR in PEM fuel cell via ^{57}Fe mössbauer spectroscopy and other techniques. J. Am. Chem. Soc. **136**, 978–985 (2014). https://doi.org/10.1021/ja410076f
265. Koslowski, U.I., Abs-Wurmbach, I., Fiechter, S., et al.: Nature of the catalytic centers of porphyrin-based electrocatalysts for the ORR: a correlation of kinetic current density with the site density of Fe–N_4 centers. J. Phys. Chem. C **112**, 15356–15366 (2008). https://doi.org/10.1021/jp802456e
266. Marshall-Roth, T., Libretto, N.J., Wrobel, A.T., et al.: A pyridinic Fe-N_4 macrocycle models the active sites in Fe/N-doped carbon electrocatalysts. Nat. Commun. **11**, 5283 (2020). https://doi.org/10.1038/s41467-020-18969-6
267. Firouzjaie, H.A., Mustain, W.E.: Catalytic advantages, challenges, and priorities in alkaline membrane fuel cells. ACS Catal. **10**, 225–234 (2020). https://doi.org/10.1021/acscatal.9b03892
268. Jaouen, F., Jones, D., Coutard, N., et al.: Toward platinum group metal-free catalysts for hydrogen/air proton-exchange membrane fuel cells. Johns. Matthey Technol. Rev. **62**, 231–255 (2018). https://doi.org/10.1595/205651318x696828
269. Wang, Y.C., Huang, L., Zhang, P., et al.: Constructing a triple-phase interface in micropores to boost performance of Fe/N/C catalysts for direct methanol fuel cells. ACS Energy Lett. **2**, 645–650 (2017). https://doi.org/10.1021/acsenergylett.7b00071
270. Wang, Y.C., Lai, Y.J., Wan, L.Y., et al.: Suppression effect of small organic molecules on oxygen reduction activity of Fe/N/C catalysts. ACS Energy Lett. **3**, 1396–1401 (2018). https://doi.org/10.1021/acsenergylett.8b00516
271. Serov, A., Artyushkova, K., Atanassov, P.: Fe-N-C oxygen reduction fuel cell catalyst derived from carbendazim: synthesis, structure, and reactivity. Adv. Energy Mater. **4**, 1301735 (2014). https://doi.org/10.1002/aenm.201301735
272. Saveleva, V.A., Kumar, K., Theis, P., et al.: Fe–N–C electrocatalyst and its electrode: are we talking about the same material? ACS Appl. Energy Mater. **6**, 611–616 (2023). https://doi.org/10.1021/acsaem.2c03736
273. Berretti, E., Longhi, M., Atanassov, P., et al.: Platinum group metal-free Fe-based (Fe-N-C) oxygen reduction electrocatalysts for direct alcohol fuel cells. Curr. Opin. Electrochem. **29**, 100756 (2021). https://doi.org/10.1016/j.coelec.2021.100756
274. Higgins, D.C., Hoque, M.A., Hassan, F., et al.: Oxygen reduction on graphene–carbon nanotube composites doped sequentially with nitrogen and sulfur. ACS Catal. **4**, 2734–2740 (2014). https://doi.org/10.1021/cs5003806
275. Govan, J., Abarca, G., Aliaga, C., et al.: Influence of cyano substituents on the electron density and catalytic activity towards the oxygen reduction reaction for iron phthalocyanine. The case for Fe(II) 2, 3, 9, 10, 16, 17, 23, 24-octa(cyano)phthalocyanine. Electrochem. Commun. **118**, 106784 (2020). https://doi.org/10.1016/j.elecom.2020.106784
276. Oyarzún, M.P., Silva, N., Cortés-Arriagada, D., et al.: Enhancing the electrocatalytic activity of Fe phthalocyanines for the oxygen reduction reaction by the presence of axial ligands: pyridine-functionalized single-walled carbon nanotubes. Electrochim. Acta **398**, 139263 (2021). https://doi.org/10.1016/j.electacta.2021.139263
277. Priyadarsini, A., Mallik, B.S.: Effects of doped N, B, P, and S atoms on graphene toward oxygen evolution reactions. ACS Omega **6**, 5368–5378 (2021). https://doi.org/10.1021/acsomega.0c05538
278. Denis, P.A., Faccio, R., Mombru, A.W.: Is it possible to dope single-walled carbon nanotubes and graphene with sulfur? ChemPhysChem **10**, 715–722 (2009). https://doi.org/10.1002/cphc.200800592
279. Denis, P.A., Huelmo, C.P., Iribarne, F.: Theoretical characterization of sulfur and nitrogen dual-doped graphene. Comput. Theor. Chem. **1049**, 13–19 (2014). https://doi.org/10.1016/j.comptc.2014.08.023
280. Liang, J., Jiao, Y., Jaroniec, M., et al.: Sulfur and nitrogen dual-doped mesoporous graphene electrocatalyst for oxygen reduction with synergistically enhanced performance. Angew. Chem.-Int. Edit. **51**, 11496–11500 (2012). https://doi.org/10.1002/anie.201206720
281. Li, X.F., Xu, Q., Fu, Y., et al.: Preparation and characterization of activated carbon from Kraft lignin via KOH activation. Environ. Prog. Sustain. Energy **33**, 519–526 (2014). https://doi.org/10.1002/ep.11794

282. Okman, I., Karagöz, S., Tay, T., et al.: Activated carbons from grape seeds by chemical activation with potassium carbonate and potassium hydroxide. Appl. Surf. Sci. **293**, 138–142 (2014). https://doi.org/10.1016/j.apsusc.2013.12.117
283. Hui, T.S., Zaini, M.A.A.: Potassium hydroxide activation of activated carbon: a commentary. Carbon Lett. **16**, 275–280 (2015). https://doi.org/10.5714/cl.2015.16.4.275
284. Ding, L., Tang, T., Hu, J.S.: Recent progress in proton-exchange membrane fuel cells based on metal-nitrogen-carbon catalysts. Acta Phys.-Chim. Sin. **37**, 2010048 (2020). https://doi.org/10.3866/pku.whxb202010048
285. Serov, A., Artyushkova, K., Andersen, N.I., et al.: Original mechanochemical synthesis of non-platinum group metals oxygen reduction reaction catalysts assisted by sacrificial support method. Electrochim. Acta **179**, 154–160 (2015). https://doi.org/10.1016/j.electacta.2015.02.108
286. Wang, Y.C., Zhu, P.F., Yang, H., et al.: Surface fluorination to boost the stability of the Fe/N/C cathode in proton exchange membrane fuel cells. ChemElectroChem **5**, 1914–1921 (2018). https://doi.org/10.1002/celc.201700939
287. Banham, D., Kishimoto, T., Zhou, Y.J., et al.: Critical advancements in achieving high power and stable nonprecious metal catalyst-based MEAs for real-world proton exchange membrane fuel cell applications. Sci. Adv. **4**, eaar7180 (2018). https://doi.org/10.1126/sciadv.aar7180
288. Wang, L., Sofer, Z., Pumera, M.: Will any crap we put into graphene increase its electrocatalytic effect? ACS Nano **14**, 21–25 (2020). https://doi.org/10.1021/acsnano.9b00184
289. U.S. Department of Energy: Technology Readiness Assessment Guide (2015).
290. Romani, A., Suriano, R., Levi, M.: Biomass waste materials through extrusion-based additive manufacturing: a systematic literature review. J. Clean Prod. **386**, 135779 (2023). https://doi.org/10.1016/j.jclepro.2022.135779
291. Kikuchi, Y., Torizaki, N., Tähkämö, L., et al.: Life cycle greenhouse gas emissions of biomass- and waste-derived hydrocarbons considering uncertainties in available feedstocks. Process Saf. Environ. Protect. **166**, 693–703 (2022). https://doi.org/10.1016/j.psep.2022.08.054
292. Cañete Vela, I., Berdugo Vilches, T., Berndes, G., et al.: Co-recycling of natural and synthetic carbon materials for a sustainable circular economy. J. Clean Prod. **365**, 132674 (2022). https://doi.org/10.1016/j.jclepro.2022.132674

Stefano Zago obtained his Bachelor's and Master's degrees in Chemistry from the University of Turin (Italy). He recently obtained his Ph.D. degree in Chemical Engineering from the Politecnico di Torino, working in the field of fuel cells and synthetizing a series of electrocatalysts for oxygen reduction reaction using waste biomass, under the supervision of Prof. Stefania Specchia. He also collaborated for a few months with Ontario Tech University (Oshawa, Canada). Other than fuel cells, his research interests involve porous materials such as metal organic frameworks.

Laura C. Scarpetta-Pizo studied Chemistry at the Universidad of the Amazonia, Colombia. She obtained a master degree in Chemistry from the University of Santiago de Chile and worked on heterogeneous catalysis for the nitration of aromatic compounds. Currently, she is working on her Ph.D. in chemistry, focusing on molecular electronics and electrocatalysis, under the supervision of Prof. José H. Zagal and Prof. Ingrid Ponce at the University of Santiago de Chile. She studies correlations between the electronic properties of molecular catalysts and their activity for the reduction of O_2 in aqueous media.

José H. Zagal is Distinguished Professor at the Faculty of Chemistry and Biology of the University of Santiago de Chile, where he directs the Laboratory of Electrocatalysis since 1982. He obtained his Ph.D. degree from Case Western Reserve University in 1978 and was postdoctoral fellow at Brookhaven National Laboratory, Upton, New York. His main research efforts are focused on the fundamentals of electron transfer reactions that are relevant for energy conversion and sensors. He has contributed to the definition of reactivity descriptors and volcano correlations for non-precious metal catalysts for electrochemical reactions. He received the Presidential Chair in Science in 1996 and is a Fellow of the International Society of Electrochemistry and of the Electrochemical Society.

Stefania Specchia chemical engineer, is a full professor of Chemical Plants Design at the Politecnico di Torino, and an associate researcher at the CNR-ITAE "Nicola Giordano" (Italy). She is a member of the Committee Board of the International Academy of Electrochemical Energy Science (IAOEES). Leader of the Gre.En^2 Group (Green Energy and Engineering Group), her technical expertise areas are catalytic reaction engineering, electrochemistry, heterogeneous catalysis and electrocatalysis. Her work has resulted in the development of a wide range of catalysts and electrocatalysts for PEMFC/DMFC, methane combustion and gas sensing. She also works on transition technologies for low- or zero-emission energy recovery systems for hydrogen production and waste valorization.

Authors and Affiliations

Stefano Zago[1] · Laura C. Scarpetta-Pizo[2] · José H. Zagal[2] · Stefania Specchia[1]

✉ José H. Zagal
jose.zagal@usach.cl

✉ Stefania Specchia
stefania.specchia@polito.it

[1] Department of Applied Science and Technology, Politecnico di Torino, Corso Duca Degli Abruzzi 24, 10129 Turin, Italy

[2] Departamento de Química de los Materiales, Laboratorio de Electrocatálisis y Electrónica Molecular, Universidad de Santiago de Chile, Ada. Bernardo O'higgins 3363, 9170022 Santiago, Chile